Fabrication and Optical Properties of Periodic Long Range Order Nanoholes on Metallic Films

Ahmad Reza Hajiaboli

A Thesis

in

The Department

of

Electrical and Computer Engineering

Presented in Partial Fulfillment of the Requirements

for the Degree of Doctor of Philosophy at

Concordia University

Montréal, Québec, Canada

November 2009

Your file Votre référence
ISBN: 978-0-494-67338-6
Our file Notre référence
ISBN: 978-0-494-67338-6

ABSTRACT

Long range order periodic structures of subwavelength apertures on optically thick metallic films have been investigated for their anomalous optical properties. Light transmission through an array of nanoholes is surprisingly higher than the prediction of the classical diffraction theorem and there is a consensus that this would be attributed to the excitation of the surface plasmon modes, a collective oscillation of the electrons on the surface of the metal due to interaction with the incident electromagnetic field. Long-range-order nanoholes array systems, contrarily to the more commonly studied short range structures, would provide several distinct advantages but the challenging fabrication process for these systems would be a major obstacle to overcome for their realization. In this thesis, it has been shown that for the long range order nanostructures of nanoholes array the spectrum of the transmitted light through the holes still showed the signature of the maxima and minima found in the transmitted spectrum for short range order systems. Experimental analysis of the spectra of these structures is however greatly simplified due to the increased total light transmission. One of the important applications of these structures is biosensing. The theoretical calculations showed that the higher flux of energy through the long range order periodic structures potentially increases the sensitivity of the biosensors based on the extraordinary optical transmission phenomenon. Two lithographic techniques based respectively on Electron Beam Lithography (EBL) and Nanospheres Lithography (NSL) for the fabrication of long range nanohole structures have been introduced. Spectra analysis of the structures by numerical calculations based on the 3 Dimensional Finite Difference Time Domain (3-D FDTD) reveals that the

primitive model of momentum matching is not sufficiently accurate to predict the transmission spectra features and hence should not be relied on as a design tool. Instead, the transmitted spectra are interpreted as resulting from a combination of scattering and resonance modes, namely localized surface plasmons resonance, Wood anomalies and Surface Plasmon Polaritons modes.

To my Family

ACKNOWLEDGEMENTS

This research would not have been possible without the support of many people. The author wishes to express his gratitude to his supervisors, Dr. Mojtaba Kahrizi and Dr. Truong Vo-Van, who have been abundantly helpful, offering their invaluable assistance, support and guidance. Gratitude is also due to the members of the supervisory committee for their thoughtful comments and suggestions.

Special thanks are due to Dr Simona Badilescu for sharing the literature and for her invaluable assistance, and to Dr. Teodor Veres and Dr. Bo Cui for making possible the access to fabrication facilities.

The author wishes to express his love and gratitude to his beloved family, particularly to his brothers, Mohammad Reza and Dr. Amir Hajiaboli, for their timeless and tireless insightful discussion and also to his parents who taught him how to persevere.

He would like to reserve his deepest thanks to his wife, Sahar, for her unflagging love and support throughout his life.

TABLE OF CONTENTS

LIST OF FIGURES

LIST OF TABLES

LIST OF SYMBOLS

ω	Angular frequency
ω_p	Plasma angular frequency
ϵ_m	Permittivity of metals
ϵ_d	Permittivity of dielectrics
χ	Electrical susceptibility
μ	Magnetic permeability
σ	Skin depth
Γ	Electron collision rate
f_k	Strength of the K^{th} Lorentzean resonance
Γ_k	Damping frequency of the K^{th} Lorentzean resonance
ω_k	Resonance frequency of the K^{th} Lorentzean resonance
τ	Mean electron collision
Δx	Spatial grid size
Δt	Time step in FDTD algorithm
Ω	Observation area
η_B	Transmission efficiency
λ	Wavelength of electromagnetic wave
θ	Angel of incident
ν	Phase velocity of electromagnetic wave

Chapter 1

Introduction

Nanostructures consist of a metallic films perforated with array of nanoscale holes exhibit an optical phenomenon known as extraordinary optical transmission (EOT). The term extraordinary refers to the difference between measurements and theoretical predictions of transmitted light through the apertures. According to the classical diffraction theorem, Bethe's theorem [1], a very small transmission through the subwavelength holes is predicted, to be proportional to the fourth power of ratio of the hole diameter to the light wavelength,$(d/\lambda)^4$. However, experimental measurements conducted by Ebbesen and coworkers in 1998 [2] using arrays of subwavelength holes fabricated on an optically thick silver film showed that the transmission is proportional to square of ratio of the hole diameter to the light wavelength,$(d/\lambda)^2$. Knowing that for a subwavelength hole ($d \ll \lambda$) , the observed transmission is much higher than what was predicted by the Bethe's theorem.

EOT, as it was labeled, occurs at specific frequencies imposed by geometrical parameters of the structure, electrical permittivity of the surrounding medium, state of polarization and angle of incident of the illuminating light. This simple optical phenomenon has opened a wealth of opportunities for potential applications, from optical switches [3,

4] and photolithography masks [5, 6] to chemical and biochemical sensing applications [7-11]. The impact of the electrical permittivity of the surrounding medium on the shape and position of the peak of the transmission is a foundation for applications of devices as chemical and biochemical sensors. More applications can be foreseen for this interesting phenomenon owing to the simplicity in which the transmission spectrum is tunable by changing the geometrical parameters of the array of subwavelength holes.

A mostly accepted physical model that explains the phenomenon of EOT is based on the excitations of the surface plasmon polaritons (SPP) mediated by the spatial perforation of the structure. Surface plasmon polaritons are collective oscillations of electrons at the surface of metallic structures coupled to the photons of the incident electromagnetic waves (light). Photons of free space propagating light do not have enough momentum to excite SPPs on a planar surface of a bulk metal. The momentum matching takes place if either the surface of a bulk metal has been textured by a nanoscale feature or the photons pass through a dense medium as a waveguide [12]. This argument implies that SPPs can be excited when the periodic structures formed by arrays of subwavelength holes which are illuminated by light. In fact, this mechanism is applied primarily to explain the EOT phenomenon.

SPPs and their characteristics have been known to scientists long before the observation of the EOT and they have been used in a wide range of applications in electrochemistry [12], wetting[13], chemical and biochemical sensing [14-16], scanning tunneling microscopy [17] and ejection of ions from surfaces [18]. Regarding the above applications, using the EOT phenomena (measuring transmitted spectrum), as compared to some of the SPPs related devices (measuring reflected spectrum), has two advantages. Firstly, there will be no need for any bulky waveguide to excite the SPPs and the devices are more easily integrated with the associate circuitry for on-chip applications. Secondly, the spectroscopic measurements for the transmission spectrum are less complicated than the

one for reflection. In spite of all the advantages, limitations of the fabrication techniques for such structures are still a major challenge to be addressed. Periodic structures such as arrays of subwavelength apertures (referred as nanohole arrays) with regard to their response to an external excitation could be categorized into two groups of short and long range order. Unlike the long range order structures, the response to the excitation in the short-range order structure is under influence of any random disorder or geometrical boundaries of the structures. Experimental studies show that the EOT phenomenon could be observed even on arrays containing a very small number of holes [19]. Most of researches in this field are devoted to study the optical properties of the short range order structures and their applications as their fabrication techniques are more available [7, 20-26]. However, these studies face the following array-size related limitations:

a. Effect of Noise:

The spectroscopic measurements and interpretation of the results are challenging tasks since the level of the shot noise at the detector of the spectrometer is dramatically increased due to the starvation of the received photons [27].

b. Collinear alignment:

Finding a few number of nanoscale holes, each beyond the diffraction limit of the visible light on a metal surface, and align them in the collinear position with the source and the collector of the spectrometer requires very high precision positioning system.

c. Effect of the boundaries:

In most theoretical studies on the nanoholes array, electromagnetic field distributions are analyzed by using a numerical solver. In the numerical solver the periodic structure is simulated by implementing periodic boundary condition to a unit cell

of the structure under study. Hence, the solver calculated the field distribution assuming that the array is infinitely extended. On the other hand, if the array contains a small number of ensemble holes, the periodicity is not well defined and the contribution of boundaries becomes significant [28]. Therefore, the discrepancy between the results obtained by the experimental measurements and those of the numerical simulations is inevitable.

To overcome these issues, using the long range order nanoholes arrays, which is the subject of this thesis, is proposed. Fabrication of the long range order structures, the most challenging issue, has been addressed in this work. One of the main goals of this research is to develop relatively simple, reliable and reproducible methods to fabricate the long range order nanohole arrays on planar metallic films. The structures are characterized and their optical properties are investigated experimentally and theoretically. The different aspects of the thesis are itemized as follow:

1. Fabrication:

   Electron beam and nanosphere lithography are used to introduce two new reproducible and tunable fabrication methods with the capability of producing the nanohole structures in the range of 3-10 mm^2. The qualities of the fabricated structures as well as the potential structural defects associated with each method are analyzed.

2. Optical characterization:

   Due to the increased number of the holes, the total energy of the transmitted light is increased. Hence, the immediate impact is that the effect of the noise in the receptor of the spectrometer is reduced. Therefore, the expected optical responses of the structure are conveniently measurable by a far-field UV-VIS spectrometer.

3. Electromagnetic analysis using numerical calculation:

   Tunability of the proposed fabrication methods motivates the comprehensive study of the spectral behavior of these structures subject to the variation of geometrical parameters. The optical responses of the structures are simulated using a numerical solver based on the finite difference time domain (FDTD) approach. The spectral behavior of the structures is analyzed in a wide range of variation of the geometrical parameters to identify the signature of each of the known scattering and diffractive modes involved in the transmission phenomenon. The results of these studies could be used to determine the optimal geometrical parameters for any desired application such as in highly sensitive biosensors.

The rest of this dissertation is organized as following:

In Chapter 2, a brief theoretical review is presented. We begin with a historical overview on the evolution of plasmonics over the last hundred years. The surface plasmon polariton dispersion relation is derived by solving the Maxwell equation on the interface of a metal and a dielectric medium, and conditions for the excitation of these polaritons will be shown.

The developed methods of fabrication and the optical measurement setup along with the results and discussion are presented in Chapter 3.

Chapter 4 of this thesis contains a detailed discussion on the mechanisms of transmission with the help of a 3-D numerical calculation. Using the simulation results, the optical spectral behavior of the long range order nanohole array over a wide range of the geometrical parameters is investigated. An overall conclusion and some of the suggested further directions are presented in the Chapter 5.

Chapter 2

Background Review and Theory

2.1 Introduction

Reflection, transmission and absorption are three main optical characteristics of a material. Metals are known as good reflectors and because of this characteristic metals have been traditionally used as optical mirrors. Metals such as silver, gold and cooper are also known as good electrical conductors. In this chapter, the relation between of the optical properties of the metals and their electrical conduction is described. It will be shown that the reflection of the light by the metal does not take place at all wavelengths of the spectrum and there will be some specific bands that are not reflected. Light at those specific energy bands, instead of being reflected, is absorbed by the surface plasmons polaritons (SPP). Since the SPPs are known as the major contributor to the extraordinary optical transmission (EOT), a mathematical frame work is presented to describe the physics involved in the transmission process and the roles of the SPP modes in EOT phenomenon.

The chapter is organized as following: in 2.2, before beginning the physics of plasmons and surface plasmons, a brief history is presented to show the evolution process and the

physical concepts lead to the field presently known as plasmonics. As an analogy to electronics, plasmonics is a field of science and technology that uses plasmons instead of electrons in associated devices.

Some physical quantities related to the interaction of the light and matters are defined in 2.3. In the next two sections of 2.4 and 2.5, with emphasis on metals such as gold and silver, two models known respectively as Drude and Lorentz-Drude (LD) models are presented to provide an approximation for the dielectric constant of the metals in the visible range of spectrum. The LD model provides a more accurate estimation for the dielectric constant of metals as compared to the Drude model. In Section 2.6, the dispersion relation of surface plasmon polaritons for metals excited by an electromagnetic source is derived using Maxwell's equations. Based on this relation, in the following section, a model known as momentum matching model for EOT through a long range order nanoholes array is presented. The shortcomings of this model are discussed and the main scattering and diffracting optical modes involved in the transmission process are introduced. Finally, the chapter is concluded with a summary.

2.2 Historical Remarks

The unique optical properties of metallic nanostructures have been used by artists to fabricate glass windows in churches even before scientists started to investigate and formulate them. One of the famous articles of this kind is the Lycurgus Cup which is dated back to the Byzantine Empire (4th century A.D) [30]. The reflected light from the cup illustrate beautiful colors as the cup rotates.

In the beginning of 20th century, professor Robert W. Wood observed an unexplainable behavior of the reflected light from a grating metallic surface, known as Wood's

anomaly (WA) [31]. As it will be explained, WA modes play a major role in the transmission spectral behavior of the nanoholes array structures. In 1904, Maxwell Garnett by using both the newly developed Drudè model of free electrons in metals and Rayleigh's theorem of scattering for spherical particles has studied the bright reflection of metallic nanoparticles embedded in glass. In 1908, Gustav Mie developed a theory, the now well-known Mie scattering theory, to explain the optical scattering of spherical particles of any size.

In 1907, Zenneck was the first to analyze the solution of Maxwell equations that had surface waves. Sommerfeld, in 1909, has realized that radio waves will propagate around the earth when the upper half space is considered as a dielectric and the earth a conductor.

In continuation of these investigations, in 1956, David Pines has developed a theoretical model to describe the energy losses experienced by fast electrons passing through metals [32]. He considered that the attenuation of energy of the electrons was due to oscillation of the free electrons in the metals. In analogy to the earlier research on plasma oscillation in gas discharges, he called this oscillation *plasmons*. In the same year, Robert Fano introduced the term *polariton* for the coupled oscillation of light and bound electrons in a transparent medium [33].

In 1957, an article was published by Rufus Ritchie on electron energy losses in thin films, in which it was shown that plasmon modes could exist near the surface of metals. This study represented the first theoretical description of surface plasmons [34]. In 1968, nearly seventy years after Wood's original observations, Ritchie and coworkers described the anomalous behavior of metal gratings in terms of excited surface plasmons [35]. In the same year, Andreas Otto as well as Erich Kretschmann and Heinz Raether presented methods for the optical excitation of surface plasmons on planar metal films, making experiments on surface plasmons easily accessible to many researchers [12].

At this point, the properties of surface plasmons are well known, however the connection to the optical properties of metal nanoparticles remained to be explained. In 1970, more than sixty years after Garnett's work on the colors of metal doped glasses, Uwe Kreibig and Peter Zacharias performed a study in which they compared the electronic and optical responses of gold and silver nanoparticles. In their work, they have described the optical properties of the metallic nanoparticles in terms of surface plasmons [36]. As the field continues to develop, the importance of the coupling between the oscillating electrons and the electromagnetic field becomes more apparent. In 1974, Stephen Cunningham and his colleagues introduced the term surface plasmon-polariton (SPP). A major boost to the field was given by the development of a commercial sensor based on surface plasmon resonance (SPR), in 1990. At present, an estimated fifty percent of all publications on surface plasmons involve the use of plasmons for biodetection. Most recently, metal nanostructures have received considerable attention for their ability to guide and manipulate the *light* at the nanoscale, and the pace of new inventions in the area has accelerated even further [37]. In 1997, Junichi Takahara and co-workers [38] have suggested that metallic nanowires are able to guide the optical beams of visible to near-infrared regions in a nanometer scale diameter. In 1998, Thomas Ebbesen et al. have reported on the extraordinary optical transmission through subwavelength metal apertures [2].

2.3 Interaction of Light with Matter

The physical quantity that describes the interaction of the electric field and a medium is known as permittivity or dielectric constant of the material. The electric charges in the medium, electrons or ions, are interacting with the external electromagnetic field in different ways including the formation of the electric dipole or electron migration and

charge accumulation in form of polarization of the medium. The response of the medium to the external electromagnetism field is represented by the electric displacement field $\vec{D}$. Its relation to permittivity in a very simple case of linear, homogeneous, isotropic materials with "instantaneous" response to changes in electric field is given by

$$\vec{D} = \epsilon\vec{E} = \epsilon_0\epsilon_r\vec{E}\ , \tag{2.1}$$

where ϵ is the electric permittivity of a given medium (i.e. a product of the free space permittivity, ϵ_0, and the relative permittivity of the material, ϵ_r). magnetic permeability, μ, is a parameter that represents the response of the material to the magnetic field. The magnetic field, B, and the auxiliary magnetic field, H, inside the matter are related by

$$B = \mu H = \mu_0\mu_r H\ . \tag{2.2}$$

Knowing the permeability and permittivity of a given material, the phase velocity of the electromagnetic field passing through the material is given by

$$\epsilon\mu = \frac{1}{\nu^2}\ ,$$

where ν is the phase velocity of the propagating electromagnetic wave. In free space, the phase velocity is known as $c = 299,792,458m/s$.

The optical property of materials is described by a quantity known as the index of refraction. The index of refraction of a medium is defined in the most simple condition when the material is a linear, isotropic, homogeneous and non-magnetic by $n = \sqrt{\epsilon}$. On the other hand, the electric displacement can also be defined as

$$\vec{D} = \epsilon\vec{E} = \epsilon_0\vec{E} + \vec{P}\ , \tag{2.3}$$

where P is the electric polarization density of the material. The polarization density is given by

$$\vec{P} = \epsilon_0\chi\vec{E}\ , \tag{2.4}$$

where χ is the electrical susceptibility of the material. This quantity defines how a material is polarized by an incident electromagnetic field.

By replacing (2.4) in (2.3) the electrical susceptibility could be found as

$$\chi = 1 - \epsilon_r \ . \tag{2.5}$$

The dielectric constant and the electric susceptibility in the material are complex numbers. Moreover they could be a frequency dependent (i.e. dispersion in the materials) quantity. The imaginary part of the dielectric constant defines the loss or absorption of the electromagnetic field in the material. The electric susceptibility and the permittivity of the metals (especially in the wavelength range from the ultra violet to the near infrared or UV_NIR) show a strong relation to the frequency of the excitation field. Atomic structures of the metal are considered as a main clue to derive a physical model to calculate the ϵ and χ for metals known as the Drude model.

2.4 Refractive Index of Metals (Drude Model)

All matters are composed of atoms which possess positively charged nuclei attracting negatively charged electrons by Coulomb forces. Generally, due to the Coulomb attraction force, electrons can hardly move away from the atoms. However, in the case of a metal, a large number of electrons in the outer shell orbits of the metallic atoms are lessening the Coulomb force causing the electrons to move freely in the metals. The Drude model has been developed based on the assumption that the material can be described as a gas of free electrons. This free movement of electrons in the metals makes these materials electrically conductive. The Drude model effectively models conductivity, dispersion and background absorption of the metals due to the electronic intraband transitions.

The Drude model derives the refractive index of a metal by analyzing the motion

of free electrons which is expressed within the framework of classical mechanics. The equation of motion of an electron in metals is given by

$$m\frac{\partial^2\vec{r}(t)}{\partial t^2} + m\Gamma\frac{\partial\vec{r}(t)}{\partial t} = -e\vec{E}(t) \ , \tag{2.6}$$

where m is the mass, $\vec{r}(t)$ the displacement, Γ the electron collision rate which is simply the inverse of the mean electron collision time $\Gamma = \tau^{-1}$ and $(-e)$ the charge of electron. The electric field of the incident light is expressed as $\vec{E}(t) = E_0 e^{-i\omega t}$ where ω is the angular frequency of the incident light. From (2.6) the electron displacement is found as

$$\vec{r}(t) = \frac{e}{m}\frac{\vec{E}(\omega)}{(\omega^2 + i\Gamma\omega)} \ . \tag{2.7}$$

Due to this displacement, an electric dipole moment ,$-\vec{r}(t).e$, is induced in each atom. Summing over all the electric dipole moments, the polarization ,$-\vec{r}(t).e.N$, is generated in the metal, where N is the number of electrons per unit volume of the metal. This polarization is also expressed as $\vec{P} = \epsilon_0.\chi.\vec{E}$. If the plasma angular frequency ω_p is defined by:

$$\omega_p = \sqrt{\frac{e^2N}{\epsilon_0 m}} \ , \tag{2.8}$$

Thus, by using (2.4) and (2.7),the electric susceptibility of the metal is derived as:

$$\chi(\omega) = -\frac{\vec{P}}{\epsilon_0.\vec{E}(\omega)} = -\frac{\omega_p^2}{\omega^2 + i\Gamma\omega} \ . \tag{2.9}$$

Hence, the imaginary and real part of the χ are given by:

$$\chi^{'}(\omega) = -\omega_p^2\frac{1}{\omega^2+\Gamma^2} \quad , \quad \chi^{"}(\omega) = \omega_p^2\frac{\Gamma/\omega}{\omega^2+\Gamma^2} \ , \tag{2.10}$$

From here the dielectric constant of the metal is given by the Drude model as:

$$\epsilon^{'}(\omega) = 1 - \omega_P^2\frac{1}{\omega^2+\Gamma^2} \quad , \quad \epsilon^{"}(\omega) = \omega_p^2\frac{\Gamma/\omega}{\omega^2+\Gamma^2} \ , \tag{2.11}$$

For metals, where the electron collision rate is $\Gamma = \tau^{-1}$, the dielectric constant of the material can be derived as:

$$\epsilon^{'}(\omega) = 1 - \frac{\omega_P^2 \tau^2}{1+\omega^2\tau^2} \quad , \quad \epsilon^{"}(\omega) = \frac{\omega_p^2 \tau}{\omega\left(1+\omega^2\tau^2\right)} \; , \tag{2.12}$$

Therefore, their index of refraction will be given as:

$$n^2 = 1 - \frac{\omega_P^2 \tau}{\omega\left(\omega.\tau + i\right)} \; , \tag{2.13}$$

The quantity $(\omega_p/2\pi)$ is called the plasma frequency. The value of $\omega.\tau$ is larger than unity as the plasma frequency is normally larger than $2\pi \times 10^{15} Hz$ (i.e. in the visible or ultraviolet region) and the value of τ of the order of $1 \times 10^{-14} s$, therefore the imaginary part of the right-hand side of equation (2.13) is negligible and n is approximated by:

$$n^2 \approx 1 - \left(\frac{\omega_P}{\omega}\right)^2 \; , \tag{2.14}$$

Figure 2-1 shows the relation between ω and n^2. Note that n^2 is negative if $\omega < \omega_p$, which means that the refractive index n takes a purely imaginary value. This also means that the incident light is totally reflected by the surface of the metals. Since $\omega.\tau \gg 1$ is valid for most of metals, they have a high reflectivity and appear shiny.

2.5 Lorentz-Drude Model

The Drude model is an accurate and valid model for the dielectric function of most metals in the visible to infrared (IR) spectrum. However, in the case of silver, gold and copper, the dielectric constant calculated by the Drude model is exhibiting significant discrepancies with experimental measurements. The atomic structure of these metals shows the same number of the free electrons located in the outer shell orbits and all of them have the *"d"* orbits filled. Copper has the electronic configuration of [Ar].3d10.4s1,

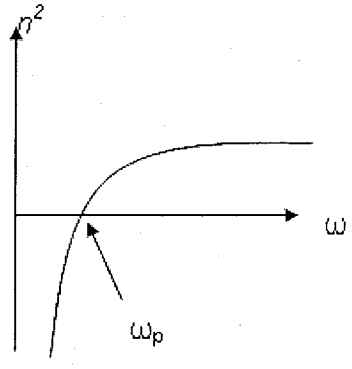

Figure 2.1: Dependency of the angular frequency (ω) of incident light on the square of the index of refraction.

silver has [Kr].4d10.5s1 and gold has [Xe].4f14.5d10.6s1. These metals are known as the "noble metals". The d-electron bands lie below the Fermi energy of the conduction band. Transitions from the d-band to the empty states above the Fermi level can occur over a fairly narrow band of energy (i.e. around $\hbar\omega_0 = E_f - E_d$). While these transitions are not considered in the Drude model, the proposed Lorentz model is an analytic approach to model them. The model calculates the optical behavior of the materials based on the interband transition of the inner shell electrons and conduction band empty states.

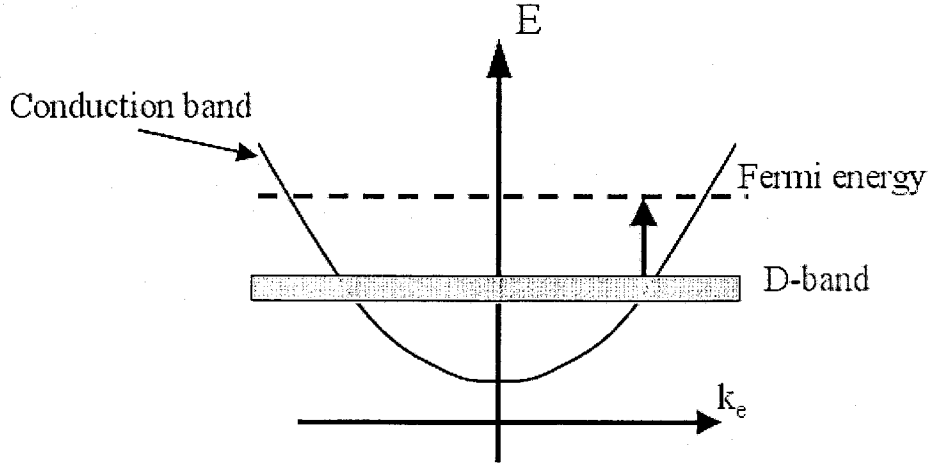

Figure 2.2: Interband transition of the d- band electrons.

The Drude and Lorentz models can be combined in a single one which takes into account both intraband and interband contributions [40]. The hybrid Lorentz-Drude (LD) model provides a dielectric function having an excellent correlation with the experimentally measured dielectric functions of many metals like silver (Ag) over a wide range of frequencies. The Lorentz-Drude model is described by the following dielectric constant:

$$\epsilon(\omega) = \epsilon^f(\omega) + \epsilon^b(\omega) \,, \tag{2.15}$$

Also it can be written as:

$$\epsilon(\omega) = \epsilon_{r,Drude} + \sum_{k=1}^{K} \frac{f_k \omega_K^2}{\omega_k^2 - \omega^2 + i\omega\Gamma_k} \,, \tag{2.16}$$

or can be rearranged in the following form :

$$\epsilon(\omega) = \epsilon_{r,\infty} + \sum_{k=0}^{K} \frac{f_k \omega_p^2}{\omega_k^2 - \omega^2 + i\omega\Gamma_k} \,, \tag{2.17}$$

In (2.17), $\epsilon_{r,\infty}$ is the optical dielectric constant at infinite frequency (for isotropic plasma-like metals $\epsilon_{r,\infty} = 1$ and ω_p is the plasma angular frequency, while ω_k, f_k and Γ_k are the resonance frequency, strength and damping frequency, respectively, of the k^{th} resonator. For $k = 0$ and $\omega_0 = 0$, the general LD model simplifies to the Drude model for free electrons. The values of parameters for several common metals are listed below in Table 2.1. In order to show the enhanced accuracy of the LD model in the case of silver, the Drude and LD models are compared with respect to the experimentally measured data obtained from [40]. As can be seen in Figure 2.3, the Lorentz-Drude model is able to describe the small resonances in the blue-end and provide an accurate fit with the real dielectric function of silver over the whole frequency range of interest.

Circles are the experimental data values taken from reference [40]. Solid line: dielectric function given by the Drude model. Dotted line: dielectric function given by the Lorentz-Drude model [41].

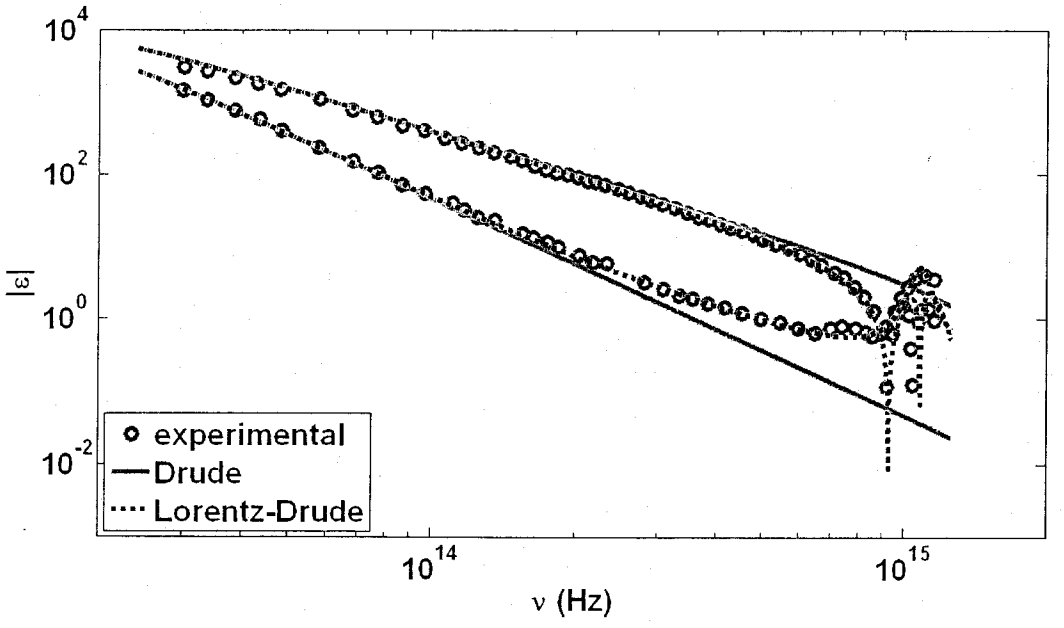

Figure 2.3: The values of the real and imaginary parts of the dielectric function of silver as a function of excitation frequency.

Table 2.1: Lorentz-Drude parameters for common metals

Parameter	Metal										
	Ag	Au	Cu	Al	Be	Cr	Ni	Pd	Pt	Ti	W
f_0	0.845	0.760	0.575	0.523	0.084	0.168	0.096	0.330	0.333	0.148	0.206
Γ_0	0.048	0.053	0.030	0.047	0.035	0.047	0.048	0.008	0.080	0.082	0.064
f_1	0.065	0.024	0.061	0.227	0.031	0.151	0.100	0.649	0.191	0.899	0.054
Γ_1	3.886	0.241	0.378	0.333	1.664	3.175	4.511	2.950	0.517	2.276	0.530
ω_1	0.816	0.415	0.291	0.162	0.100	0.121	0.174	0.336	0.780	0.777	1.004
f_2	0.124	0.010	0.104	0.050	0.140	0.150	0.135	0.121	0.659	0.393	0.166
Γ_2	0.452	0.345	1.056	0.312	3.395	1.305	1.334	0.555	1.838	2.518	1.281
ω_2	4.481	0.830	2.957	1.544	1.032	0.543	0.582	0.501	1.314	1.545	1.917
f_3	0.011	0.071	0.723	0.166	0.530	1.149	0.106	0.638	0.547	0.187	0.706
Γ_3	0.065	0.870	3.213	1.351	4.454	2.676	2.178	4.621	3.668	1.663	3.332
ω_3	8.185	2.969	5.300	1.808	3.183	1.970	1.597	1.659	3.141	2.509	3.580
f_4	0.840	0.601	0.638	0.030	0.130	0.825	0.729	0.453	3.576	0.001	2.590
Γ_4	0.916	2.494	4.305	3.382	1.802	1.335	6.292	3.236	8.517	1.762	5.836
ω_4	9.083	4.304	11.18	3.473	4.604	8.775	6.089	5.715	9.249	19.43	7.498
f_5	5.646	4.384	-	-	-	-	-	-	-	-	-
Γ_5	2.419	2.214	-	-	-	-	-	-	-	-	-
ω_5	20.29	13.32	-	-	-	-	-	-	-	-	-

2.6 Plasmon Polaritons

In the same way as photons that can be defined as an elementary particle, the quantum of the electromagnetic field, a plasmon, is defined as the quantum of the collective excitation of free electrons in solids. Plasmonics effects are more applied in metals since these materials behave as a free-electron gas when the excitation frequency ω is below the plasma frequency ω_p of the metal. Polaritons are the coupled mode of a photon and another type of excitation. Thus, the plasmon-polariton is a plasmon-photon coupled mode. There exist two types of plasmon polaritons - bulk and surface modes.

2.6.1 Bulk Plasmon Polaritons

Collective oscillations of the electrons in the bulk metal are called the *bulk plasmon polaritons*. The propagation of the electromagnetic field inside a medium can be formulated by Maxwell equations and the dispersion relation for the bulk plasmon polaritons is derived from these. If the source of excitation is a plane wave $\vec{E} = \vec{E}_0 e^{[i(\vec{k}.\vec{r}-\omega t)]}$, in an isotropic homogeneous medium with no initial charge, $\epsilon(\omega)$, the electric displacement follows the condition $\nabla.\vec{D} = 0$. This condition leads to:

$$\epsilon(\omega)\vec{k}.\vec{E} = 0 \ , \tag{2.18}$$

Equation (2.18) could present two solutions:

The first one is $\epsilon(\omega) = 0$ which leads to the longitudinal bulk plasmon polariton mode discussed in 2.3 for the Drude model of free electrons.

The second solution is the transverse bulk plasmon polaritons mode that is derived from the relation $\vec{k}.\vec{E} = 0$. With the help of Maxwell equations:

$$\vec{\nabla} \times \vec{H} = \frac{\partial \vec{D}}{\partial t} \ \text{ and } \vec{\nabla} \times \vec{E} = -\frac{\partial \vec{B}}{\partial t} \ ,$$

the dispersion relation of the transverse bulk plasmon polaritons of a metal can be derived as:

$$k^2(\omega) = \epsilon(\omega)\frac{\omega^2}{c^2}\,, \tag{2.19}$$

where ω is the frequency of the excitation source, c is speed of light in free space, and k is the wavevector to the bulk plasmon polaritons.

2.6.2 Surface Plasmon Polaritons

Physically, surface plasmon polaritons (SPPs) are defined as a collective oscillation of charge carriers in the conducting layer, transferring the energy parallel to the interface. These electromagnetic surface waves are bound to the interface of the conduction layer (metal) and the dielectric medium. SPPs can be seen as electromagnetic surface waves that are solutions of the Maxwell equations with lateral extensions evanescently decaying into both sides of the interface. The penetration length of the evanescent waves is longer for the dielectric medium as compared to the metallic side.

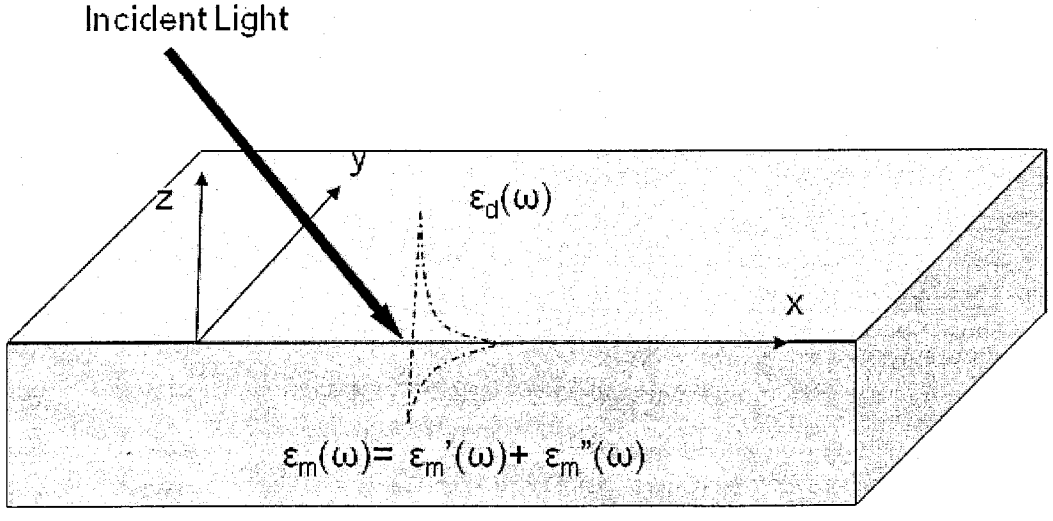

Figure 2.4: The evanescent field of SPP decaying in either side of the interface. The dotted line represents the SPP evanescent waves.

S-polarized light (TE polarization) refers to the polarization state that has the electric field parallel to the surface of the interface. P polarized, transverse magnetic (TM) polarized light is light that has the electric field lying in the light plane of incidence (the plane that is perpendicular to the surface of the interface and contains the wavevector of the excitation source). In order to excite the SPP modes on a planar metal surface an oblique incidence of the p-polarized light, which has a non-zero perpendicular electric vector component on the z axis, is required. The displacement of the electric charge on the z axis is generating the forces that lead to the transversal motion of the electromagnetic field at the lateral direction bounded to the interface. It should be noted that TE polarized light is providing merely a lateral charge displacement of the electron on the surface of the metal which is not a necessary condition for exciting the SPPs. The dispersion relation of the SPPs can be derived from the solution of the wave equation for a p-polarized electromagnetic incident light governed by Maxwell equations and subjected to the boundary conditions that ensure the continuity of the tangential and normal field components. The details of the solution are as following. A source of plane wave with TM polarization is defined as:

$$\vec{E}(x,z) = (E_{jx}, 0, E_{jz})\, e^{i(k_x x - \omega t)} e^{(ik_{jz} z)} \,, \tag{2.20}$$

where the j is either 1 or 2 which refers either to the metal or the dielectric medium. As the boundary condition is applied at $z = 0$ and at the interface, k_x, or the x component of k, is the same in both mediums at the interface. The dispersion relation for K_x is the same for SPPs or $\omega(K_x) = \omega(K_{sp})$.

The conservation of the momentum gives:

$$K_x^2 + K_{jz}^2 = \epsilon_j K_0^2 \,, \tag{2.21}$$

where $k_0 = \omega/c$ and j refers to the medium (1 or 2) .

If the imaginary parts of ϵ_m and ϵ_d are being neglected and considering the primary assumption for the SPPs as evanescent modes decaying in both mediums,

$$Im(k_{1z}) > 0 \qquad \text{and} \qquad Im(k_{2z}) < 0 \ .$$

From (2.21) the normal wavevectors, K_{1z} and K_{2z}, can be defined as following:

$$K_{1z} = iK_1 \ , \tag{2.22}$$

$$K_{2z} = -iK_2 \ . \tag{2.23}$$

For any isotropic, charge free, homogeneous medium, i.e. $\vec{\nabla}.\vec{D} = 0$, by applying (2.20) into this equation the relation for the amplitude of the electric field is derived as:

$$K_x E_{jx} + K_{jz} E_{jz} = 0 \ , \tag{2.24}$$

where $j = 1, 2$ for the dielectric or metallic medium.

Continuity conditions are translated to the boundary conditions as following:

$$E_{1x} = E_{2x} \ , \tag{2.25}$$

$$\epsilon_1 E_{1z} = \epsilon_2 E_{2z} \ . \tag{2.26}$$

From (2.24) the amplitude of the E_1 and E_2 can be derived as:

$$K_x E_{1x} + K_{1z} E_{1z} = 0 \ , \tag{2.27}$$

$$K_x E_{2x} + K_{2z} E_{2z} = 0 \ , \tag{2.28}$$

By applying the boundary conditions of (2.25) and (2.26) into (2.27) and (2.28), an implicit dispersion relation can be derived as following:

$$\frac{K_{1z}}{\epsilon_1} = \frac{K_{2z}}{\epsilon_2} \ , \tag{2.29}$$

From (2.29) one of the basic condition of the excitation of SPPs is that the real parts of ϵ_1 and ϵ_2 should have opposite signs since K_{1z} and K_{2z} have opposite signs. By substituting (2.21) into (2.29) the explicit relation for K_x and eventually K_{spp}, the wavevector of surface plasmon polaritons is derived as:

$$K_x = K_{spp} = \frac{\omega}{c}\sqrt{\frac{\epsilon_m \epsilon_d}{\epsilon_m + \epsilon_d}}\,, \tag{2.30}$$

where c is velocity of light and ϵ_m and ϵ_d are dielectric constants of the metal and the dielectric interface, respectively.

The second condition for excitation of the SPPs is that, not only the real parts of ϵ_m and ϵ_d have to be in opposite signs, but also, $\epsilon_m + \epsilon_d < 0$, or in other words, $|\epsilon_m| > |\epsilon_d|$. The above condition is defining the range of frequencies for which the SPPs can be excited. The imaginary part of K_{spp} corresponds to the propagation length of the surface wave before it is damped in the metal. On a smooth surface of noble metals such as gold or silver, the propagation length is about tens of micrometers.

The real part of K_{sp} , $R(k_{sp})$, for a typical noble metal is plotted versus frequency in Figure 2.5. As it can be seen, $R(k_{sp})$ always falls below the light line (the line that separates the free space photons from the evanescent ones). The diagram shows that such modes are evanescent and therefore cannot be excited directly by the free propagating photons. Experimentally, three different methods have been developed to overcome the momentum matching problem.

2.6.3 Attenuated Total Reflection

The most common technique is the "attenuated total reflection" (ATR) which is realized in the Otto's configuration Figure 2.6 using total internal reflection (TIR) in a prism for the coupling condition [12].

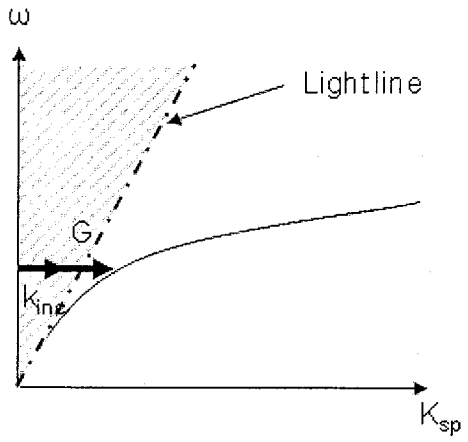

Figure 2.5: Dispersion diagram of surface plasmons.

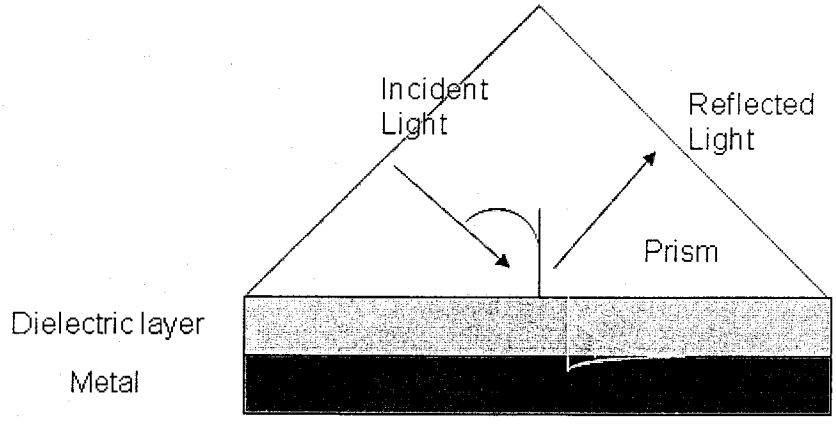

Figure 2.6: Otto's arrangement for the excitation of surface plasmon waves.

These arrangements have been vastly studied theoretically and experimentally. The wavevector of the light will be increased by traveling through the dense medium of the prism. The new wavevector can be defined as $K' = n.K$, where n is the index of refraction of the prism and K is the light wavevector in vacuum. At the total internal reflection condition the evanescent waves as surface waves at the base of the prism have enough momentum to excite surface plasmons at the top side of the metal film. As it has been mentioned earlier, these arrangements have already been applied in commercial instruments for biosensing.

2.6.4 Grating SPR Coupling

Alternative SPR configurations are based on the coupling of optical waves and surface plasmons by a grating surface. The incident electromagnetic radiation is directed toward a medium whose surface has a spatial periodicity (D) similar to the wavelength of the radiation. As an example, a reflection diffraction grating is shown in Figure 2.7. The incident beam (solid line) is diffracted, producing propagating modes which travel away from the interface (dash line) and evanescent modes which exist only at the interface. The evanescent modes have wave vectors parallel to the interface, similar to the incident radiation. These modes couple to the surface plasmons (dot line) which run along the interface between the grating and the ambient medium. This phenomenon is known as Wood's anomaly [31]. The suppression in the reflection spectrum observed in Figure 2.7 is related to the diffraction of the light to the evanescent surface waves in metallic grating surfaces. The mechanism of coupling can be explained by the SP dispersion diagram given in Figure 2.7. For the coupling between the incident light and the SPs to take place, a given extra momentum G is needed. Therefore, the wave vector K_{inc} of the incident light will fall to the evanescent one where the SP modes exist. This is expressed as a simple

resonance condition as

$$\vec{K}_{sp} = \vec{K}_{inc} + \vec{G} \,, \tag{2.31}$$

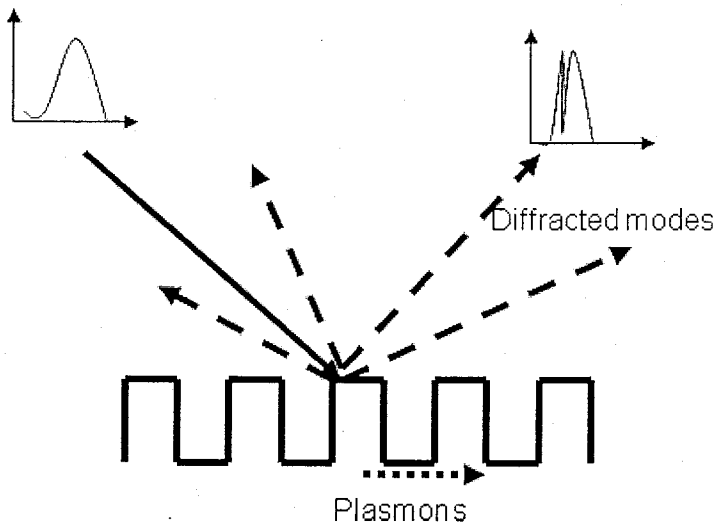

Figure 2.7: Grating surface and surface plasmon excitation.

Unlike the ATR method where the momentum matching condition is provided by shifting in the position of light line, here the extra momentum will be provided by grating. For example, in the one dimensional periodic grating surface, G which is a multiple of $2\pi/D$ (D is the period of grating) will add to K_{inc}. Hence, the resonance condition can be written as following:

$$\vec{K}_{sp} = K_0 sin\theta + i2\pi/D \,, \tag{2.32}$$

where, i is an integer.

2.6.5 Optical Waveguide SPR Coupling

The coupling of optical waves and surface plasmons may furthermore be realized by an optical waveguide system as it is shown in Figure 2.8. A light wave is guided by the waveguide and, entering the region with a thin metal overlaid, it evanescently penetrates

through the metal layer. If the surface plasmon wave and the guided mode are phase matched, the light wave excites a surface plasmon wave at the outer interface of the metal. At the end of the wave guide, the outgoing light is detected by photodiodes. A decrease of the detected signal again occurs upon the resonant surface plasmon coupling. Optical waveguide systems have some attractive properties including a simple way to control the optical path and the small sizes [98].

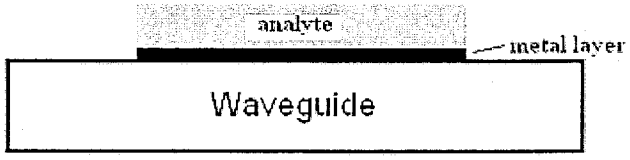

Figure 2.8: Waveguide SPR coupling.

2.6.6 Choice of Materials for SPR Based Devices

The surface plasmon resonance excitation mainly depends on the properties of the metal film, the wavelength of the incident light and the refractive index of the media on either side of the metal film. Because the refractive index is sensitive to temperature, it is important to perform the measurements at well defined temperatures. The metal must have conduction band electrons capable of resonating with the incoming light at a suitable wavelength. Metals that satisfy this condition are silver, gold, copper, aluminum, sodium and indium. In addition, the metal must be free of oxides, sulphides and not to react with other molecules on exposure to the atmosphere or to a liquid. Among the metals, indium is too expensive, sodium too reactive, copper and aluminum too broad in their SPR response and silver susceptible to oxidation although it exhibits better optical response compared to gold. Gold is the most practical metal. Gold is rather resistant to oxidation

and other atmospheric contaminants but is compatible with a lot of chemical modification systems. The thickness of the gold should be more than 70 nm. The thickness of the metal layer is important to guarantee that there is no direct photon tunneling involved in the transmission process. The light source should be polychromatic and non-polarized due to the two-dimensional symmetric geometry of the structures, for plane wave normal incident the transmission is independent of the polarization.

2.7 Extraordinary Optical Transmission (EOT)

Bethe in his *Theory of Diffraction by Small Holes*, investigated the transmission of electromagnetic waves through a subwavelength hole for the first time [1]. Bethe established his theory for electromagnetic wave in the microwave region. He solved the problem assuming two cavities separated by an infinitesimally thin film of a perfectly conductor material that contained a subwavelength hole. Using these assumptions, the theory suggests a very simple equation for transmission efficiency η_B (normalized to the area of aperture) as:

$$\eta_B = \frac{64(kd)^4}{27\pi^2}, \tag{2.33}$$

where $k = 2\pi/\lambda$.

His theory predicts a transmission dependence of $(d/\lambda)^4$, where d is the diameter of the hole and λ is the wavelength of the electromagnetic wave.

Although the problem was solved in the microwave regime, the scale invariance property of of electromagnetic wave equations (Maxwell's equations) makes it applicable to light in visible and near infrared range, which is of interest to applications in telecommunications, medicine, sensing, and data storage.

While these dependencies are well established, Ebbesen observed [2] much higher transmissions, proportional to $(d/\lambda)^2$ through an optically thick metal film with an array

of subwavelength apertures. A metal film is called optically thick when the film is thicker than the skin depth (σ) of the metal by an order of magnitude. The skin depth in the metals is defined by

$$\sigma = \frac{c}{2\omega\sqrt{\epsilon}} \approx \frac{c}{2\omega_P}, \tag{2.34}$$

where c is velocity and ω in angular frequency of light and ϵ is dielectric constant of metal. ω_P denotes the plasma angular frequency. This is a quantity that characterizes the length of penetration of the electromagnetic field in the metal before being reflected. The skin depth is the order of 5 to 10 nm in a metal such as aluminum and it is about 15 to 20 nm in the visible to NIR range for silver and gold.

Ebbesen conducted his experiment under the following conditions: white light has been illuminated on perforated silver (Ag) films with a thickness of $t = 0.2\mu m$. The holes had a diameter (d) between $150nm$ to $1\mu m$ and the spacing a_0 was about $0.6\mu m$-$1.8\mu m$. Figure 2.9 shows the zero-order transmission spectrum that has been obtained with a UV-near-infrared spectrometer. The peak at $\lambda = 326nm$ corresponds to the normal bulk silver plasmons. More interesting are those peaks at $\lambda > a_0$, which are the transmissions of light waves through subwavelength nanostructures. The maximum transmitted intensity occurs at $1370nm$, almost ten times d.

Experiments showed that this effect takes place on metals such as Au, Cr, Ag and not for (Ge, Si) films which are semiconductor materials. Moreover, EOT is strongly dependent on the angle and polarization of light. Furthermore, it was shown that the peak positions were determined by the holes periodicity that is comparable to the wavelength of the incident light [29]. By modifying the thickness and diameter of the holes, one can control the shape of the peaks in term of the width and intensity [44]. It was due to these facts that many researchers believe that SPP is responsible for EOT and developed models to explain the phenomena [2, 45, 46].

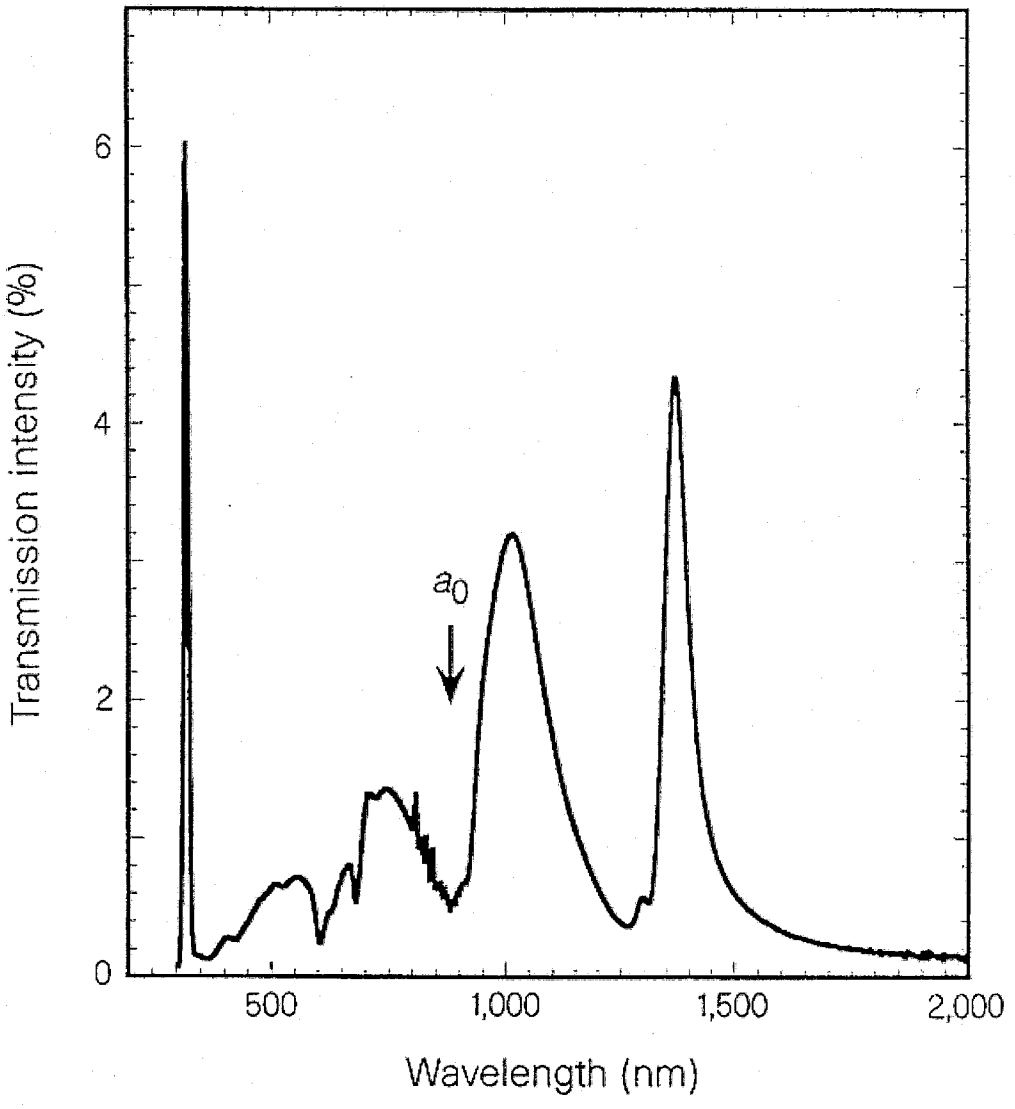

Figure 2.9: Zero order transmission spectrum through an Ag film perforated with nanoholes [2].

According to the SPP model for EOT, the light illuminated on the surface of the film is absorbed by the SPP modes. The modes then transmitted to the far side of the film and reemitted from back side in the form of propagating photons. Matching between the energy and momentum of the photons of the incident light and those of the electrons in the conduction band of metals can occur owing to the extra momentum introduced by the periodicity of the metallic medium. Therefore, the collective excitation of the conduction electrons in the metal due to interaction with the incident photons in the periodic structures is called surface plasmon polariton Bloch wave or simply SPP. The first approximate model that describes the features of the transmission spectra was introduced by Ebbesen [2] and his colleagues based on the following coupling matching condition:

$$\vec{k}_{sp} = \vec{k}_x \pm i\vec{G}_x \pm j\vec{G}_y \ , \tag{2.35}$$

where $\vec{k}_{sp}$ is the surface plasmon wave vector, $\vec{k}_x$ is the component of the incident wave vector that lies in the plane of the surface, $\vec{G}_x$ and $\vec{G}_y$ are the reciprocal lattice vectors, for a square lattice with $|\vec{G}_x|$, $|\vec{G}_y| = 2\pi/a_0$, and i, j are integers. a_0 is the period of the holes. Applying the coupling condition to this primary model would permit the estimation for the peak position in the spectrum. For instance, in the hexagonal crystalline structures the peak position would be as following:

$$\lambda_{max} = \frac{P}{\sqrt{\frac{3}{4}\left(i^2 + ij + j^2\right)}} \sqrt{\frac{\epsilon_m \epsilon_d}{\epsilon_m + \epsilon_d}} \ . \tag{2.36}$$

The same relation can be derived for an array with square lattice structure as:

$$\lambda_{max} = \frac{P}{\sqrt{\left(i^2 + j^2\right)}} \sqrt{\frac{\epsilon_m \epsilon_d}{\epsilon_m + \epsilon_d}} \ , \tag{2.37}$$

where P is the period of the array, ϵ_m and ϵ_d are the dielectric constants of the metal and the dielectric material in contact with the metal respectively and i, j are two integer numbers representing the scattering orders of the array.

The result of this model is demonstrated in Figure 2.10. the structure is a hexagonal hole array of circular holes milled on a 225 nm thick gold film. The holes diameter and arrays period are $170nm$ and $520nm$ respectively. Based on the SPP model, the first peak is predicted at the position marked by $(1,1)$ corresponding respectively to the integer numbers i and j in equation (2.36), the second peak is likewise predicted and marked by $(1,0)$. Both peak positions are estimated at a shorter wavelength when compared to those given by the solid line which represents the actual measurements of the transmission spectrum for the hexagonal nanohole structure depicted in the inset of Figure 2.10. The quantity I/I_0 is the transmission efficiency through the array and η is the same transmission efficiency when it is normalized to the area of the holes. The diagram shows that at the peak position, the total light transmitted through each hole is more than twice the impinging light in the hole. The features of the spectrum interpreted by Ghaemi et al. [47] are in the form of a combination of maxima and minima ascribed by SPP and Wood anomalies. Professor R.W Wood was the first scientist who reported on the anomalous reflection spectrum of metallic grating structures in 1902 [31]. He has observed, without adequate explanations, that reflected light from the grating surface of a metal does not contain some of the wavelengths of the original light source. In 1970, Wood's anomaly was explained by Hassel et al. [48] as the combination of excitation of SPPs in the grating surface, and Rayleigh waves which are the higher order diffracted light at the surface of the metallic grating object . According to the Ghaemi's interpretation, while the SPPs modes are contributing to the maxima of the transmitted spectrum, the Wood anomaly modes (Rayleigh modes) correspond to the position of minima.

Wavelengths of Wood anomalies modes in the two dimensional grating structures of nanoholes arrays with a square lattice structure can be calculated as following [49, 50]:

$$\lambda_w = \frac{D}{\sqrt{(i^2+j^2)}}\sqrt{\epsilon_d}\,. \tag{2.38}$$

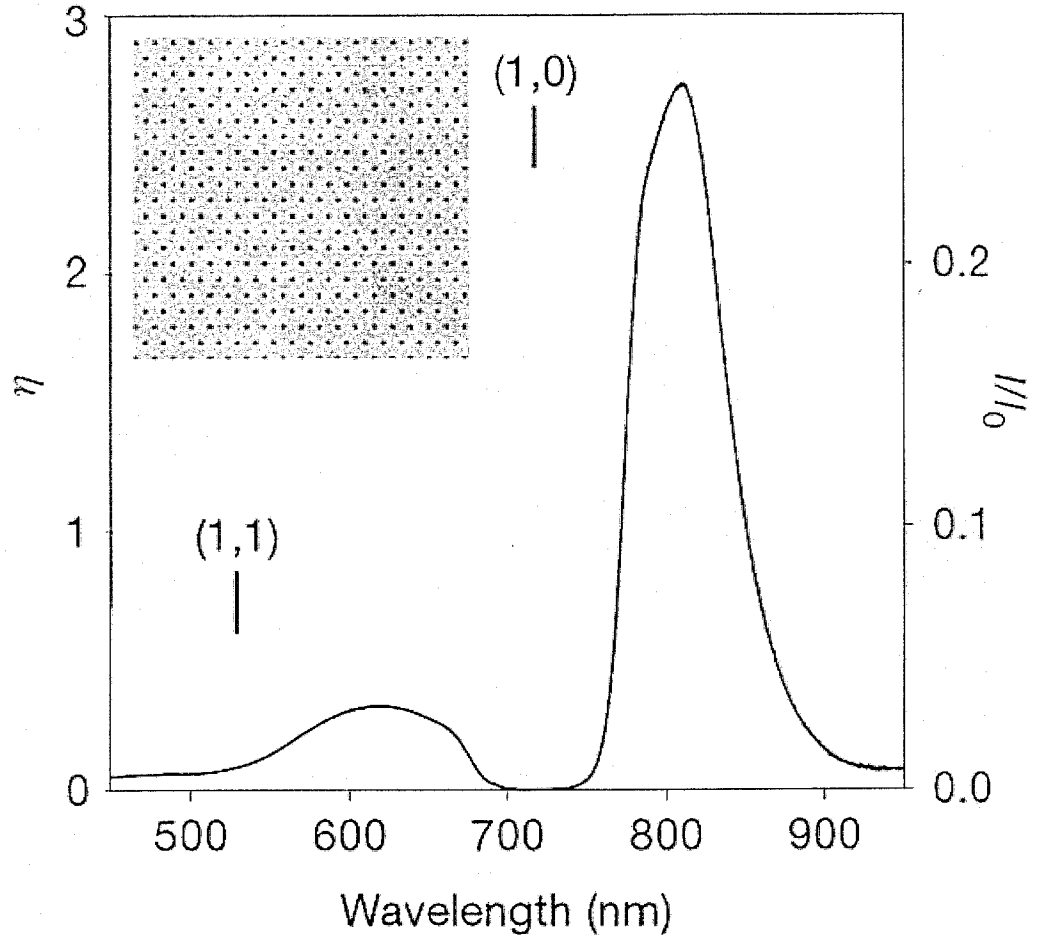

Figure 2.10: Transmission spectrum of hole a array [29].

The Wood's anomaly appears in the perfect conductor as well as in real metals with finite conductivity. In other words, WAs are purely geometrical and do not depend on the dielectric constant of the metals while SPPs are strongly dependent upon the dielectric constant of the metal and the surrounding medium.

There has been speculation [51, 52] that , EOT (when compared to rigorous diffraction theory) is not necessarily the result of SPPs. Opponents of the SPP model in the transmission process provide several reasons for their argument that are as following:

1. Although, Ebbesen's discovery was the first investigation of EOT in the range of visible light [2] (in this range of spectrum of light metals cannot be approximated to perfect conductors), the phenomenon was studied by other researchers like Ulrich who investigated in 1967 the transmission of infrared light (in this range of light spectrum metals can be considered as perfect conductors) through arrays of sub-wavelength holes [53], and Chen [54] who predicted zero reflection through array of holes with sub-wavelength diameter.

2. Comparing the result of the transmission through array of subwavelength holes with what predicted by the Bethe theorem is not justifiable as Bethe's theory is developed for the transmission of light through a single hole only. Recently a research published by Gordon [55] has proved that the revised Bethe's theory for an array of subwavelength holes predicts a 100% transmission. In another word, EOT is in fact due to the suppression of some modes due to the finite thickness and finite conductivity of the metal in the visible range. This argument is exactly opposite to what was suggested by the SPP model.

3. EOT is not a particular property of an array of nanoholes on metallic film. The phenomenon is also observed in the nonmetallic film such as polaritonic silicon dioxide

film [56] or tungsten (W) film [52](although tungsten is a metal, its dielectric constant in the visible range and it thus cannot support SPP excitation). Furthermore, as presented earlier [55], EOT is also predicted for the perfectly conductor film.

These arguments result in other models such as the one presented by Lezec [57]. According to this model, Composite Diffracted Evanescent Wave (CDEW) is responsible for selective enhanced and suppressed transmitted modes.

Since 1998, upon discovery of EOT, there has been numerous research on the EOT phenomenon, exploring experimental aspects [58] as well as theoretical models [59, 60] and still there are debates over the physical models that can exactly describe the mechanism of the transmission. However, the SPP/Photon coupling seems to be most widely accepted phenomenon contributing to the EOT [61]. The fact that neither the effect of the thickness of the film nor the shape of the holes are taken to the account by SPP model may limit its capacity in the accurate prediction of the maxima.

The role of localized surface plasmon modes (LSPR) in the enhanced transmission through periodic subwavelength apertures has been investigated [62-64]. The effect of LSPRs modes was also referred as the "Shape Resonance" in some publications [46-48]. The effect of polarization of the incident light on the transmission process when the shape of the holes is non-circular is also studied [65-67]. Comparison of the transmission spectra through rectangular holes with those with circular holes (but the same area) showed that the excitation of LSPRs and the transmission efficiency is dependent on the shape of holes [68, 69]. In the case of a single hole or for nanohole arrays on a thin metallic films, LSPR are the dominating modes to describe the transmission spectrum [62, 70].

2.8 Summary

A set of theoretical background is presented in this chapter to provide an overview on concepts of EOT and the latest research in this field. In this matter, first we start with the definition of the dispersion behavior of the metals and both the Drude and the Lorentz-Drude models are described. An accurate analytical model to approximate the electric permittivity of the noble metals in the visible range of spectrum is an important building block of any accurate simulation for the plasmonic structures. In Chapter 4, the Lorentz-Drude model is applied to numerical calculations for the transmission spectral analysis of the long range order nanohole arrays.

In the next section, starting from Maxwell's equations, the dispersion relation for the surface plasmon polaritons at the interface of a planar film excited by the plane wave light source has been derived. This dispersion relationship is applied in the momentum matching argument to derive the predictive model for the position of the peaks in the transmission spectrum from long range order nanohole arrays. Moreover, positions of the dips of the spectrum and its relation to the diffractive modes of Wood anomaly are discussed .

SPPs and LSPR as resonating modes and WAs as diffracting modes are the most dominant optical modes involved in the transmission process. In Chapter 4 of this thesis, the spectral behavior of the structures is investigated using a 3-D numerical simulation tools and the effects of the resonance and scattering modes over the overall transmission spectra will be discussed.

Chapter 3

Fabrications and Characterizations

3.1 Introduction

The periodic arrays of sub-wavelength nanoholes in optically thick metallic films are one of the promising structures for applications in photonic circuits and light manipulation at the sub-wavelength range. A few methods exist to fabricate such structures. Direct-writing is the technique which is mostly been used so far. In this method, a Focused Ion Beam (FIB) is used to write the patterns on a surface of metals. This technique offers precise control of both size and period of the holes, however, as it was discussed in Chapter 1, this method is not suitable for fabrication of the long range order structures as it is very slow and has a low throughput characteristic. Another method is called nanoindentation. In this method the holes are punched on the surface of metal using sharp needles of tips of atomic force microscopy (AFM). Recently, two other methods for fabrication of the long-range-order arrays of nanoholes are reported in the literature [71, 72]. Both the techniques are based on high contrast inference lithography approaches. In this work, I introduce two methods to fabricate long range order arrays of nanoholes. One of these methods is based

on direct-writing of the patterns using electron beams. The second method is based on self-assembly of micro/nano spherical particles called nanosphere lithography technique. In the following, I describe the two techniques in detail and the results of the fabricated structures are discussed. Furthermore, the evaluation of the two techniques based on the quality of the produced structures and the nature of possible structural defects are presented. The structures are characterized by the optical transmission spectrum using UV-VIS spectrometer with a given set up shown in the Section 3.4.

3.2 Electron Beam Lithography (EBL)

In this lithography method, a beam of electrons is used to generate the pattern on the surface of materials. Due to the shorter wavelength of electrons which are less than 1nm as compared to photons, the feature size of the pattern can go beyond the diffraction limit of photons even in the case of extreme ultra violet (EUV) lithography. This form of lithography has found wide applications in mask-making (for masks used in both photolithography and ion milling), low-volume production of semiconductor components and research and development on nanostructures. The minimum feature size that can be obtained by this method is 10- 20 nm for a single spot. However, for periodic structures the minimum size will be larger due to interfering of electrons used to write the adjacent features.

The following will describe the method to fabricate arrays of nano holes on pieces of quartz using EBL. The electrons of the E-beam writer have a spherical penetration in the polymer resist rather than a perpendicular one. Hence, the fabricated nanoholes using EBL alone will have conical rather than cylindrical shapes whereas the ideally fabricated structures are the one with the cylindrical holes. The technique which includes a "double lift-off" procedure is designed to overcome this drawback of the EBL method.

In the double lift-off approach, two layers of polymers separated by a protection layer like SiO_2 that is deposited on the substrate. PMGI is a polymer resists based on polydimethylglutarimide used as a first layer. PMGI resists are designed for applications requiring high resolution imaging, easy process tuning, high yields and superior deposition line width control. Mainstream applications which are utilizing PMGI resists include, wireless devices, opto-electronics, Micro/Nano Electromechanical Systems ($MEMS/NEMS$) and packaging. In our design PMGI is used as a sacrificial layer.

The second layer of polymer used in the double lift-off method is either polymethylmethacrylate (PMMA) or a polymer with the trade name of ZEP-520 manufactured by Nippon Zeon Co.. This polymer layer acts as a electron resist [60]. Both of these polymers are high resolution positive resists, simple to use and give reproducible results. ZEP-520, compared to PMMA, is three times faster in writing and has a good dry etch resistance. However, it has poor adhesion properties (requires hexamethyldisilazane (HMDS) prime layer as an adhesive promoter) [73]. Both of these polymers are successfully examined in our design and reproducible results can be obtained.

After this brief introduction, the exact 8 steps procedure for the EBL lift-off method is given in the following:

Step 1: Cleaning the substrate by immersing it in acetone, washing in methanol and then washing in isopropanole. The substrate is dried by N_2.

Step 2: Depositing a stack-up layered structure consists of layers of Polydimethylglutarimide (PMGI) and a layer of silica (SiO_2) covered by a layer of ZEP-520 or PMMA. It is prepared using spin coating for depositing the polymer layers. Electron beam evaporation technique is used to deposit the silica (SiO_2). The top of the stack is covered by Cr layer to serve as a mean to discharge the electrons while the beam is writing the pattern on the electron resist (charge accumulation on the electron resist will decrease the resolution and divert the beam). The schematic of this structure is shown in Figure 3.1.

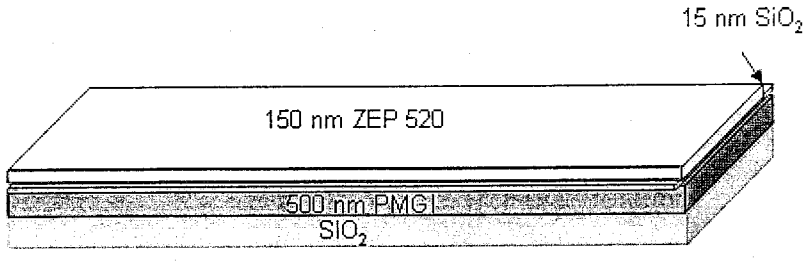

Figure 3.1: Stack up structure made from PMGI and ZEP 520.

Step 3: The pattern is written on the direct electron resist polymer using the modified scanning electron microscopy (SEM). The acceleration voltage is set to 10KV and the scanning is adjusted for 50 μs exposure of electron on each spot. Once the pattern is written the Cr layer is removed. The resist is developed; an array of nanoholes is induced on the electron resist polymer. The schematic is shown in the Figure 3.2.

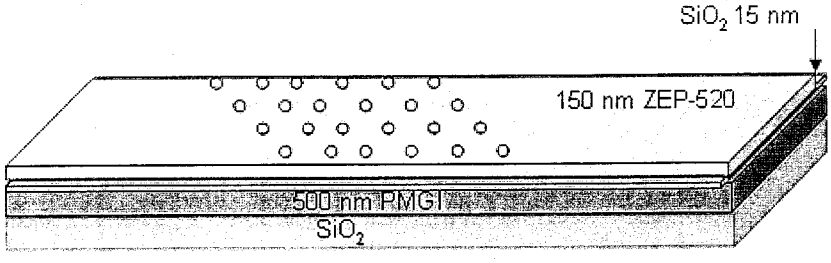

Figure 3.2: Direct writing the pattern of nanohole in positive resist.

The chromium layer is removed by immersing the substrate in a chemical solution known as "Transene Chromium" Etchant (contains 6 wt% Nitric Acid and 16% Ceric Ammonium Nitrate). Polymers of the resist have different developers ($MF - 319$ for PMMA and solution of xylene for $ZEP-520$). Immersing the sample in the corresponding solution for $20 - 40$ minutes will develop the pattern.

Step 4: Depositing a thin layer of chromium. The thickness of this metal layer should be no more than 15 to 20 nm. The cross-section of the structure after metallization by Cr is shown in the schematic below.

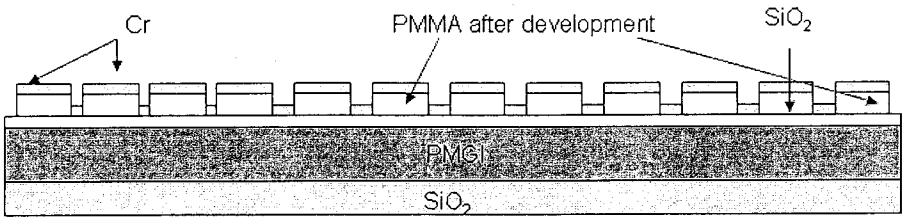

Figure 3.3: Structure after developing and deposition of Cr.

Step 5: The lift-off process of electron resist will leave arrays of the dots on the planar surface of SiO_2. The lift-off is done by immersing the sample in a solution of anisole followed by sonication for 25 minutes. [1]

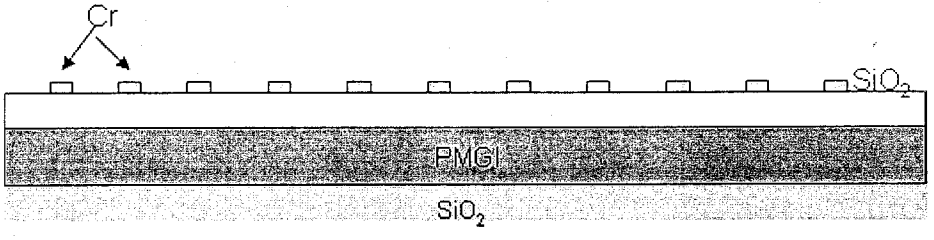

Figure 3.4: Lift-off by first polymer resist of electron resist.

Step 6: Knowing the rate and conditions of PMGI and SiO_2 etching (Table 3.2), PMGI and SiO_2 have been dry etched to form the nanopillars structures as shown in Figure 3.5. The PMGI can be etched very well by the O_2 while silica was etched by a mixture of O_2 and CF_4 with a ratio of 2/20 sccm.

Unit of flow rate for the gas is Sccm which stands for "Standard Cubic Centimeter per Minute" and is defined as following:

$$1sccm = \frac{6.02214179 \times 10^{23}[atoms/mole]}{22.413996[liters/mole\ at\ STP] \times 10^{3}[cc/liter] \times 60[s/min]}$$

[1] It should be mentioned that the structure as appears in the Figure 3.4 is another alternative plasmonic structure. It has been the subject of many interesting researches such as in [74]. Its optical properties in term of localized surface plasmon resonance (LSPR) have been analyzed and the dependency of the LSPR to the periodicity and shape of the metallic nanoparticles provided some promising applications including in biosensing area [11, 70, 71, 75-77].

$$= \quad 4.47792 \times 10^{23}[atoms/s] \ .$$

It is very important not to over etch the PMGI layers as it may deform the pillar structure causing a conic shape for holes or even collapse of the pillars. On the other hand, under etch of the PMGI will cause the structures to be completely removed from the substrate in the next lift-off step. Therefore, the thickness of the PMGI needs to be measured by a profilometer before the etching process (Reactive Ion Etching (RIE) by O_2). A controlled etching for this layer is a critical point of fabrication in this method. Figure 3.5 shows the structure after RIE process.

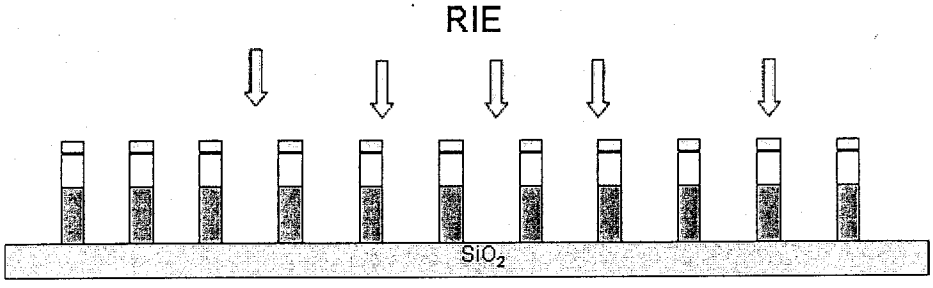

Figure 3.5: Dry etching of the SiO_2 and PMGI and formation of the nanopillar structures.

Step 7: metallization of nanopillars. First a thin layer of Cr is deposited using electron beam evaporation (EBE) to increase the adhesion of the silver or gold layer to the substrate. Due to high absorption of Cr in visible light, this layer has to be very thin. In this work, a thickness of 3 to 5 nm is used. Then a layer of silver or gold is deposited over the Cr layer using the EBE. The thickness of this layers are in order of 120 to 150 nm.

Step 8: opening the holes by removing the PMGI nanopillar structures. The second lift-off step by PMGI is done by immersing the structure in a base solution of (NH_4OH). PMGI dissolves easily in this solution. In order to prevent the collapse of metallic particles that are located in the head of the nanopillars into the surface of the film, it is important

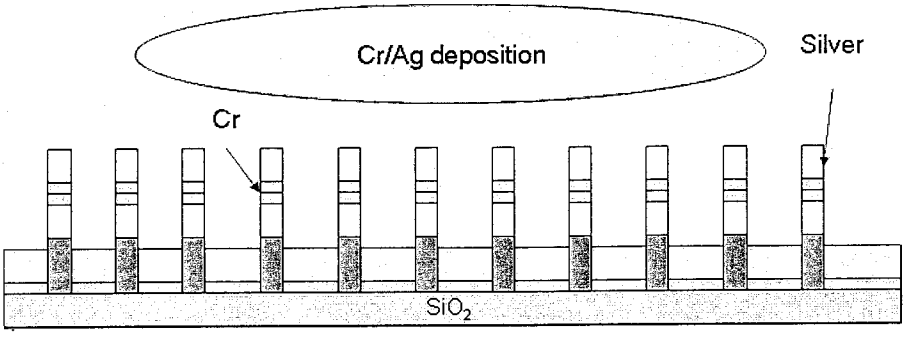

Figure 3.6: Schematic presentation of the structure after metallization.

to immerse the sample in the solution face down. A schematic for the final product is shown in the Figure 3.7.

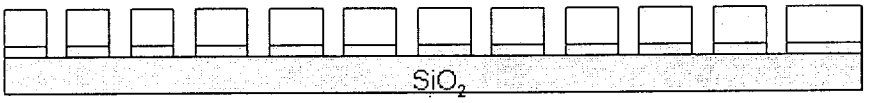

Figure 3.7: Arrays of nanoholes.

3.2.1 Results and Discussion

The following pictures are some of the SEM images of the structures fabricated using the above procedure. Optimization of the deposition rate of the metal layer is particularly important in the fabrication of nanostructures including plasmonic structures such as nanoholes arrays. If the deposition rate of metals such as silver or gold exceeds $2-3$ angstrom per second then, the films will not be very smooth and homogeneous. Instead, it will be more a granular film covered by grains of the metal. The diameters of the grains can be up to about 150 nm. On the other hand, this rate cannot be less than 0.5 angstrom/s otherwise cracks are induced on the surface. Thus, in order to achieve a smoother surface and not to create cracks, the evaporation rate needs to be adjusted. The optimum rate has been chosen around 0.8 to 1 angstrom per second with a resulting

film shown in Figure 3.8. The surface is smooth in contrast to Figure 3.9 that shows a granular surface (deposition rate > 1 Å/S).

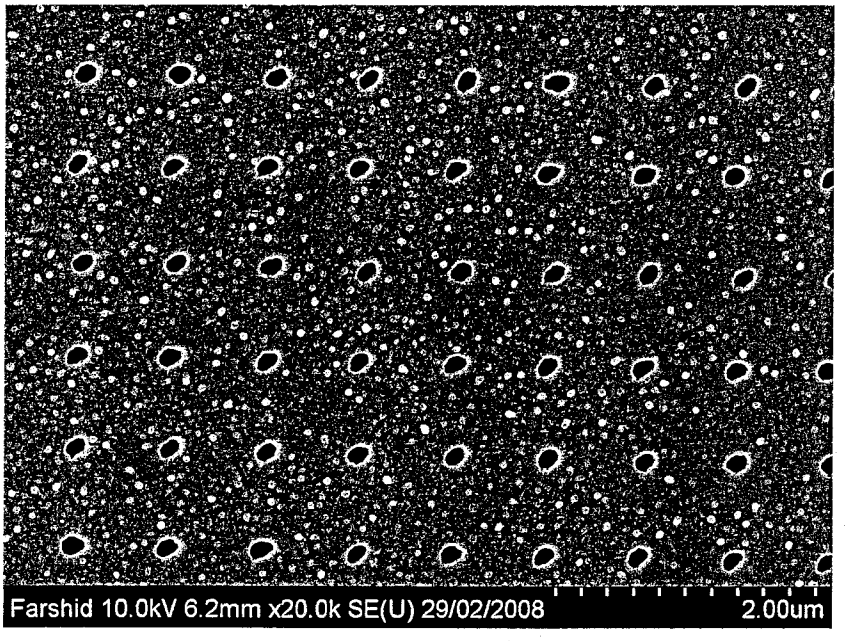

Figure 3.8: Periodic nanohole structure on silver film fabricated by the electron beam lithography.

The quality of the structure depends on the quality of the electron beam writer and its resolution. The close up image of the holes shows that the holes are not perfectly circular. This will be even more pronounced for the larger areas. As the electron beam is diverted from the center of the scanning region, it goes out of focus. Therefore, at the border of the array structures, the holes become more elliptical. To solve this problem, a basic module of $400\mu m^2$ has been considered as a unit area for the scanning region. This is the optimum region that allows the beam not to lose its focus. The beam in each of these areas needs to be adjusted and focused again. However, in this case, the chance that two regions will overlap is high. The structural defects associated to this method are discussed in the next section.

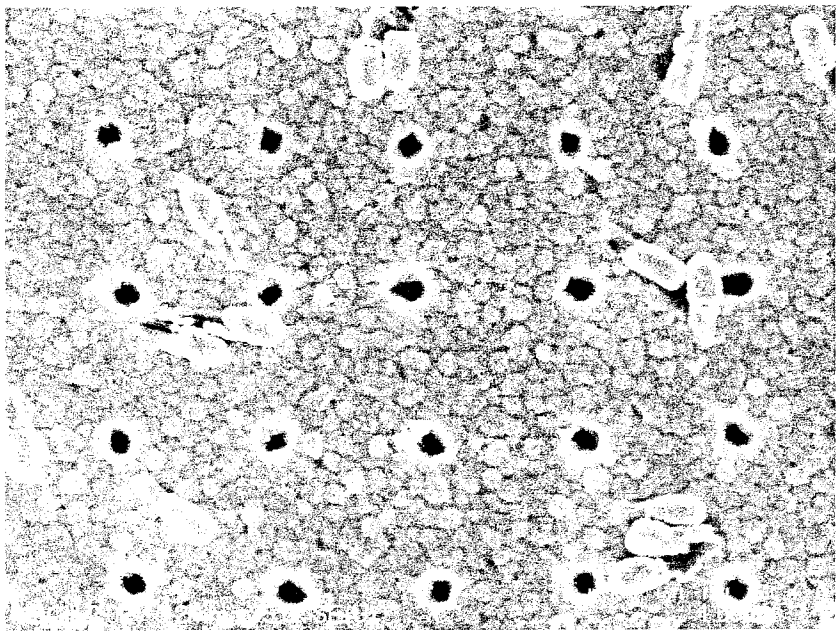

Figure 3.9: The granular structure of nanoholes' array in silver film.

3.2.2 Potential Structural Defect

Depend upon the quality of the E-beam gun and shortcoming of the instrument used in this technique the following defects were observed in the samples.

a) Non uniform circular holes

The close up image of the sample is shown in Figure 3.10. The holes are not completely circular which is mostly affected by the quality of the e-beam instrument used to write the pattern.

b) Overlapping of the nanoholes arrays

The result of overlapping of the two patterned unit modules during the writing of electron beam due to misalignment of beam is shown in Figure 3.11.

c) Elliptical hole shape

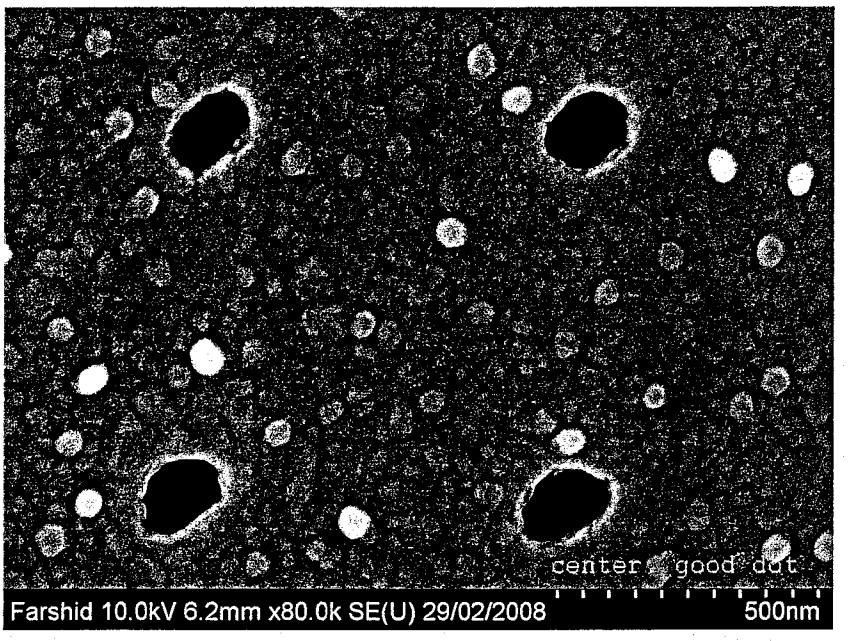

Figure 3.10: The close up images of the metallic structure by SEM.

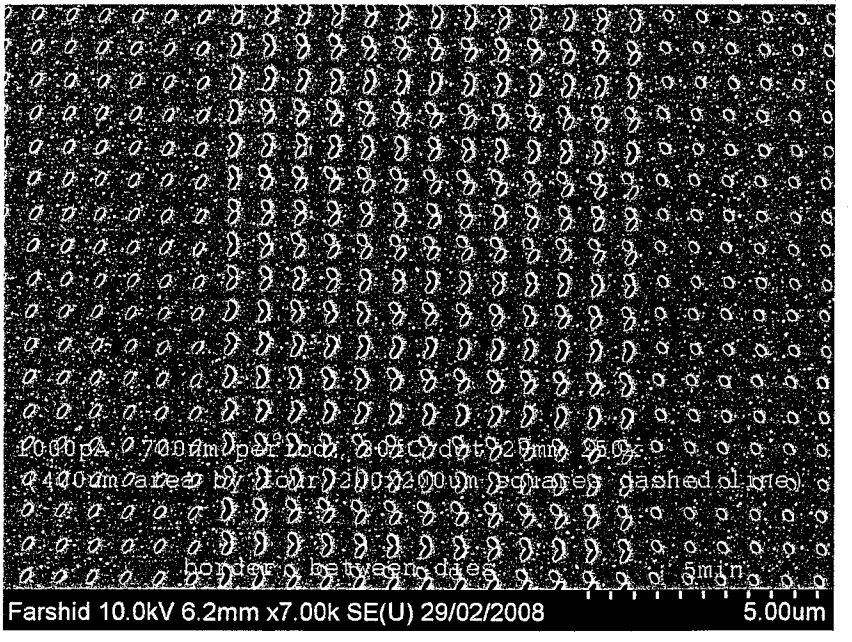

Figure 3.11: Overlapping of two regions during the writing.

The next image shows the elliptic holes which are due to the deformation of the beam of electron while the writing is taking place in the region far from the center of the arrays. Interestingly, both of these structures which are categorized as potential defect in the process of fabrication of the circular nanoholes have been studied as novel nanohole structures [67, 78].

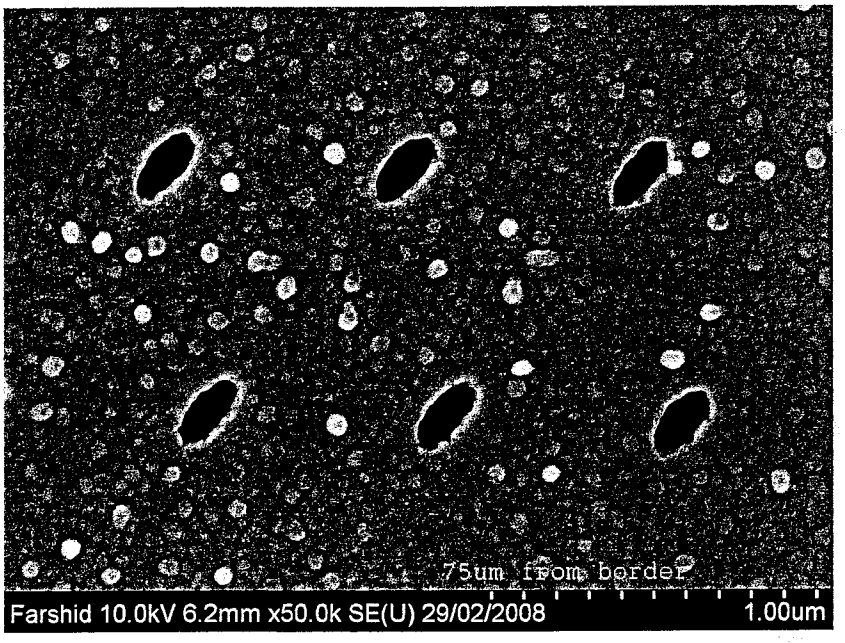

Figure 3.12: Elliptic hole shapes

d) conic hole shape

The other potential defect is the defects in the walls of holes in vertical direction. Due to the overetching of the nanopillar structures of PMGI, the holes fabricated by this method could potentially have a conic shape rather than the perfect cylindrical form.

In the SEM image of Figure 3.9, the dimple structures left on the sample surface after the lift-off belong to PMGI nanopillars which could provide some information about the

shape of the wall of the holes. The quality of the holes in the vertical direction can be controlled by controlling the etching of the PMGI.

3.3 Nanosphere Lithography (NSL)

Monodisperse colloidal microspheres are versatile building blocks for the fabrication of structures in many fields such as sensing [79, 80], photonic band gap[81] materials and more recently surface patterning [82]. Compare to the EBL method, Nanosphere Lithography (NSL) is an inexpensive, simple and high throughput nanofabrication technique capable of producing a large variety of nanostructures [70, 83].

In this section, the recent efforts to broaden the scope of NSL by fabricating cylindrical hole structures on Ag/Au film deposited on glass substrates [43] is described.

Process flow of the proposed method is shown in the Figure 3.13. As the schematic shows, the process is divided into 4 steps described below:

Step 1 Preparation of Template

In this step a template structure has to be fabricated. This template is a long range order monolayer structure of microspheres. To do so, three different tasks have to be done as following:

a) Cleaning the substrate

Glass substrates has to be cleaned by 10-min of sonication in detergent.

b) Surface Rendering

Two method can be used to render the surface of glass substrate hydrophilic, one chemical and the other one a physical approach. In the first method, a cleaned glass substrate is immersed in a solution of H_2O: NH_4OH:H_2O_2 (5:1:1) while it is

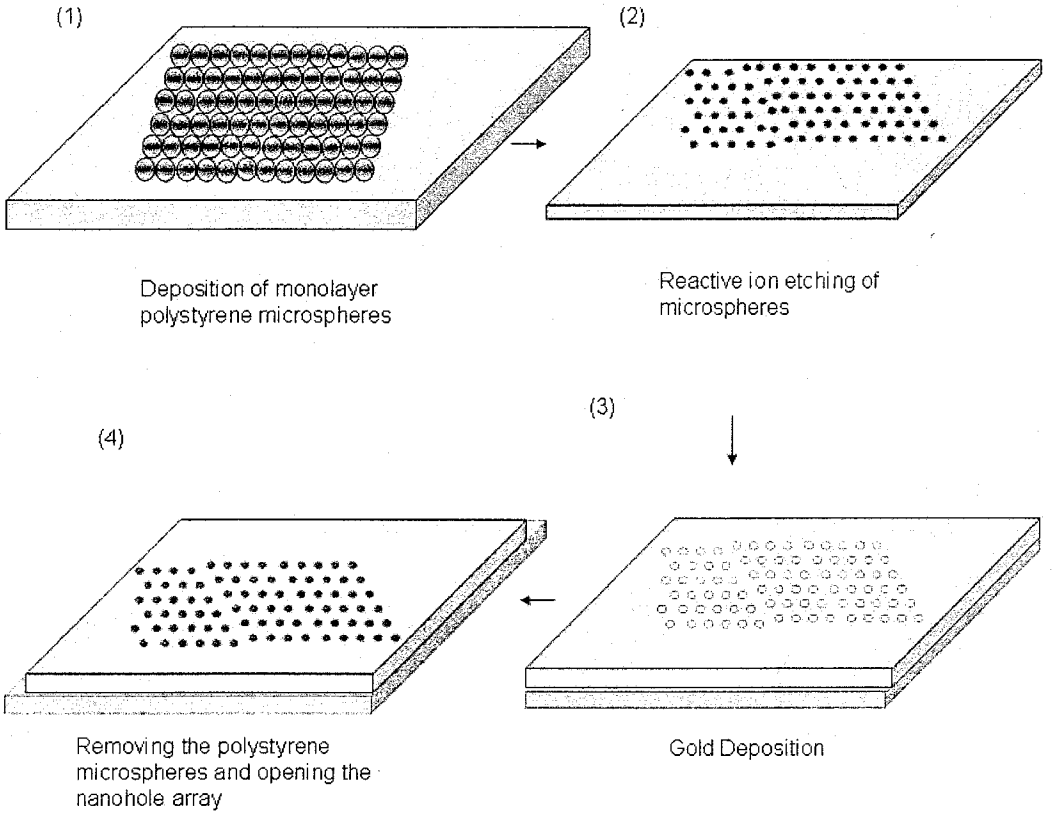

Figure 3.13: Process flow for fabrication of long range order array of nanoholes by NSL.

placed in the ultrasonic bath for one hour. The second technique that can be used is bombardment of oxygen ions on the glass substrates. For this propose, the cleaned glass substrate is placed in the RIE chamber and bombarded by oxygen ions with a flow rate of 20 sccm for 3 to 4 minutes. Although the second method is more preferable due its speed , both of these techniques are successfully tested during our experiments.

c) Microspheres deposition

Polystyrene/Silica microspheres are spin-coated onto the treated substrates. This yields a hexagonal close-packed monolayer of microspheres, which serves as a NSL deposition mask.

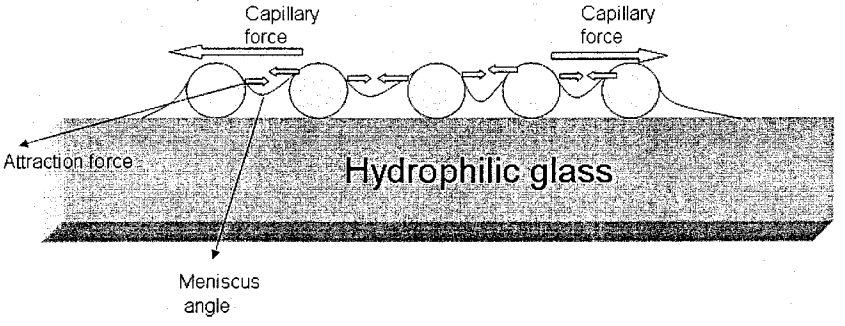

Figure 3.14: Crystallization of Monolayer Closed Packed Hexagonal Structures.

As the colloidal solution of the microspheres dried out on the surface of the substrate, the equilibrium condition of the forces leads to formation of a hexagonal closed packed structure of microspheres. The monolayer structure is formed when the liquid is spread on the surface to a height of less than half of the diameter of the spheres. Otherwise, it could result in a multilayer structure. Since the host liquid of the colloidal solution of microspheres is water and it has to be well spread on the surface of the substrate to obtain a large area of a monolayer crystalline structure. Therefore, it is critically important to render the surface hydrophilic before deposition of the microspheres.

Table 3.1: Spin coating of monolayer microsphere structures

Diameters	Material	Spin RPM	Acceleration Rate RPM /S	Duration
750 nm	Polystyrene	750	500	50 s
1090 nm	Polystyrene	800	550	45 s
1250 nm	Silica	800	600	60 s

Figure 3.15 shows the two structures of monolayer microspheres. The top image is for polystyrene spheres and the bottom one is for silica microspheres with diameters of 750 nm and 1.25 μm respectively. As it can be observed in the top image there are some areas that have not been covered by spheres. These regions can be minimized by optimization of the rotation rate of the spinner and the evaporation rate of water from the solutions of colloidal crystal nanospheres.

The optimum conditions of the deposition for the polystyrene/silica microspheres in the solution with a concentration of %5 w/v (weight of the particle per volume of solution) are shown in Table 3.1. These parameters are empirically determined through a repetitive process of deposition and characterization.

All of the microspheres used in these experiments have been purchased from Sphrotech Inc.. The particles are purified so there is no need for further purification process by users.

Availability and cost efficiency of the method outweight the larger number of defects as compared to the EBL method. In terms of the optical properties of the structures fabricated by this technique, as it will be discussed in the next chapter, the structures periodicity is only one of the parameters involved in the overall optical response of the structures. The shape of the holes as well as the thickness of the metal film are the other important factors. Therefore, considering the fact that defects in the monolayer microspheres crystalline structure will be covered by metal in step three of the procedure, these structures, in spite of their defects still exhibit EOT.

Step 2 Reactive ion etching (RIE) of the polystyrene/Silica

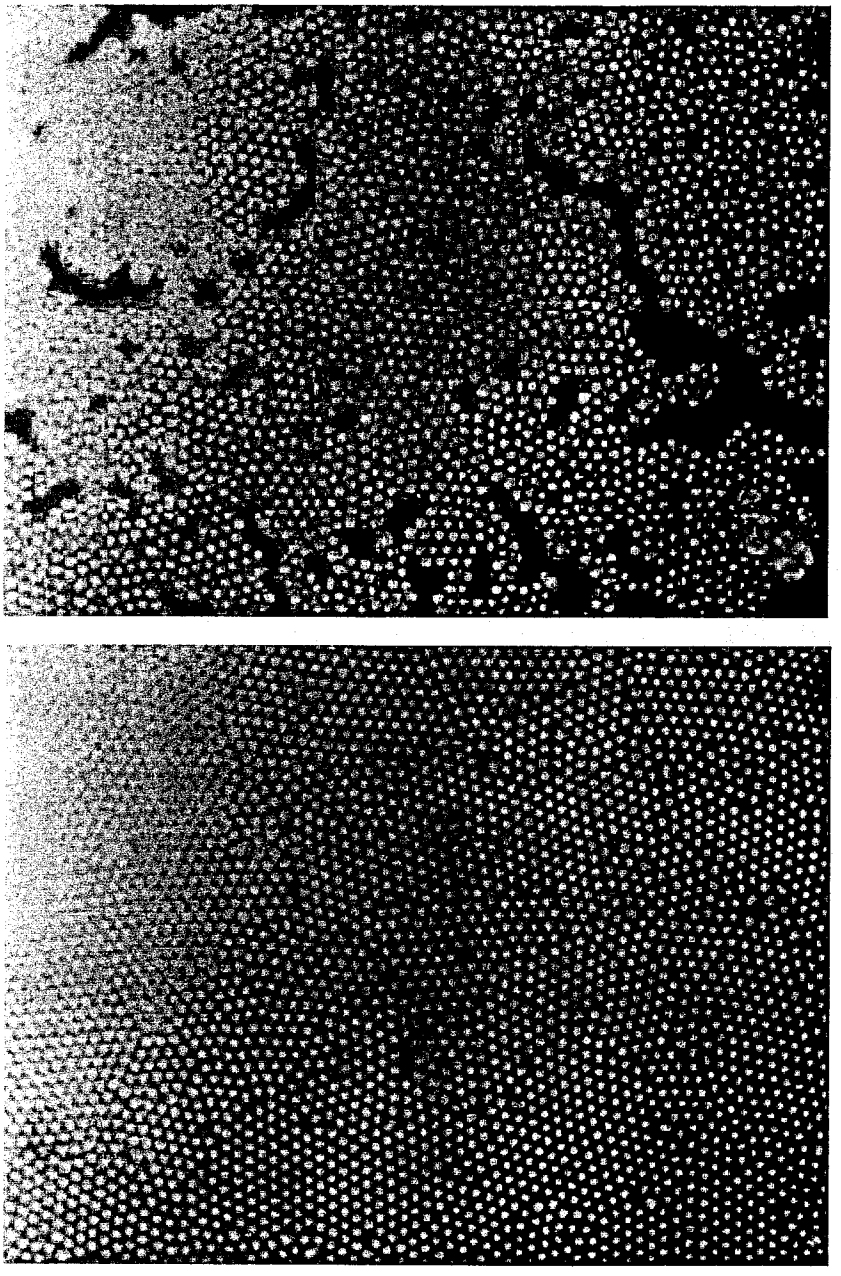

Figure 3.15: The optical microscopy image of a monolayer of self assembled microspheres in hexagonal crystalline structure.

The monolayer template prepared by spin coating of microspheres is dry etched by RIE. Sizes of the spheres are shrunk to the desire size of the holes. The condition and the rate of the etching are among the major factors that define the reproducibility and the uniformity of the fabricated structures. The following table shows the different setups that can be applied for etching of the polymers of ZEP-520 and PMMA as well as silica and polystyrene microspheres. This step is necessary for any accurate fabrication procedure of nanostructures that involve the dry etching of polymers or silica because fabrication *recipes* should be tuned according to the equipment that is available.

Table 3.2: The rates and conditions of etching of polymers and silica

Polymer RIE: the following all use a quartz plate						
Material	Power (Watt)	Gas Flow Rate(sccm)	Pressure (mTorr)	DC Bias (V)	Etch Rate (nm/min)	Comment (Etch time, etc)
Polystyrene	100	CHF3/O2=20/1	5		21	Etch 10 min
Polystyrene	200	CHF3/O2=20/2	10	237	23	Etch 6.5 min
Polystyrene	100	$CHF_3$20sccm	10	100	9.4	Etch 8 min
Polystyrene	200	$CF_4/O_2 = 20/2$	10	285	85	etch 8 min.
silica	200	$CF_4/O_2 = 20/2$	10	285	85	25nm/min.
Polystyrene	100	O_2 20sccm	10	98	63.3	Etch for 9min, accurate
Polystyrene	100	O_2 20sccm	200	67	64.2	Etch 12min.
PMMA	100	O_2 20sccm	10		176	sometimes even faster.
PMGI	100	O_2 20sccm	10	100	130	Etch 1 min
SU-8	100	O_2 20sccm	10	100	86	Etch 1.5 min
Ti	100	$CF_4/Ar = 20/5$	10	350	25/4	not accurate
ZEP-520	100	O_2 20sccm	10	100	127	Etch 3 min
LOR-5A	100	O_2 20sccm	10	100	180	Etch 2 min

Characterization of the fabricated sample in each step of the etching shows that the etching of the templates is an anisotropic process in the lateral and vertical directions. This process is discussed in Section 3.3.1.

Step 3 metallization

First, a thin film of Cr is deposited on the template to improve the adhesion between the Au/Ag film and the glass substrate. Thickness of this layer should not exceed 5nm due to the fact that Cr is a highly absorptive material in the visible range. Then a layer of Ag or Au with a thickness of 100nm to 120nm is deposited. Electron beam evaporation (EBE) technique is used for both depositions. The deposition rate should be tuned to about 1 nm/s to reduce the size of the metal grains in the structure as it is discussed for metallization in the EBL method in section 3.2.1. The importance of using EBE for metallization is discussed in the next section.

Step 4 Lift-off of the microspheres

Immersing the sample in the ethanol while the sample is placed in ultrasonic bath for 3 to 4 minutes will remove the microspheres and open the holes on the metallic film. The sample is washed by ethanol and dried by N_2 afterward.

3.3.1 Anisotropic etching process

Dry etching of the monolayer microspheres is an anisotropic etching in the lateral and vertical directions. In order to provide a reproducible and tunable method for fabrication of nanohole arrays based on NSL, this phenomenon have to be taken to the account.

a) Anisotropic etching in the lateral direction

Although all of the etching setups shown in Table 3.2 will effectively etch the polystyrene as well as silica nanospheres, the etching of polystyrene spheres by CF_4/O_2 will result in an uneven and anisotropic etching of these spheres. The

laterally anisotropic etching of the spheres is associated with the presence of the heavy molecules of CF_4 in the etching gas which will randomly hit the spheres of polystyrene. The result of etching by CF_4/O_2 is shown in Figure 3.16. The same uneven shape is expected on the top surface of hemispheres which make the lift off process more difficult than in the case when the spheres have been vertically etched to the same height.

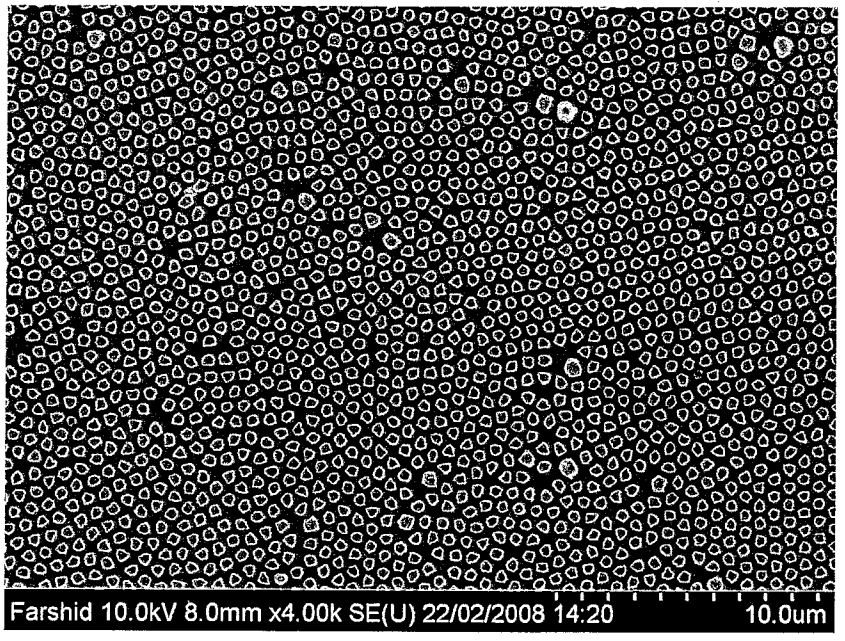

Figure 3.16: Etching by the CF_4 and O_2 and presence of the sharp edges in the holes.

b) Anisotropic etching in the vertical direction

Detailed characterization of the microspheres in several stages of the etching, after every minute of the RIE, shows another anisotropic process in the etching of the spheres. The rates of etching of the silica and polystyrene are not similar in vertical and lateral directions. The spheres which are exposed more to the flow of ions from the top are etched faster in the vertical direction than in the lateral direction.

This process is depicted in Figure 3.17. If the microspheres are etched till they lose half of their height then the rate of lateral etching is increased. When the gap between the spheres is increased, the sides of the hemispheres are more exposed to the etchant gas. By increasing the rate of bombardment of the ions to the side of the hemispheres, the etching rate will be increased. Moreover, the reactive etching of the spheres is not the only parameter involved that defines the size of the diameter of the holes in the final product. The curvature shape of the spherical particles is another important parameter too. When the spheres are etched to the point that their height is reduced to more than half of the original diameter, the curvature of the hemispheres as well as the chemical etching are defining the size of the holes.

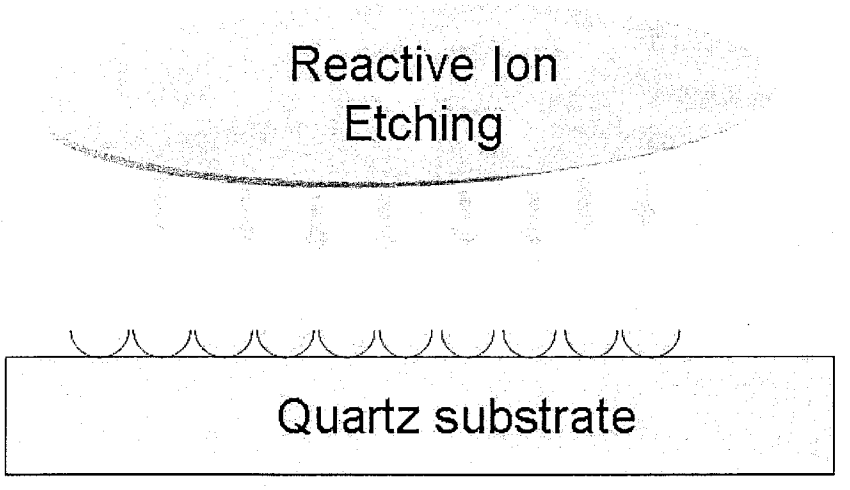

Figure 3.17: Anisotropic etching of the microspheres in lateral and vertical direction.

In order to achieve the holes with diameters beyond the diffraction limit of visible light as $\lambda_{inc}/2$ (around 100 to 150 nm) the spheres should be etched to the point that their height will be less that half of their diameters before etching. This will make the liftoff process very difficult especially if the film ought to be as thick as 100 to 150 nm. In order to be able to remove the etched spheres after metal deposition, the monolayer

films of microspheres with larger spheres have to be prepared and characterized as it has been shown in Figure 3.15.

3.3.2 Results and Discussion

The following images belong to some of the samples that have been fabricated using NSL. A close-up image of the sample is shown in Figure 3.18 to illustrate the uniformity of the hole shapes while the structure shows a hexagonal crystalline arrangement. The samples produced by NSL have large areas of coverage in the order of $10 - 100\ mm^2$.

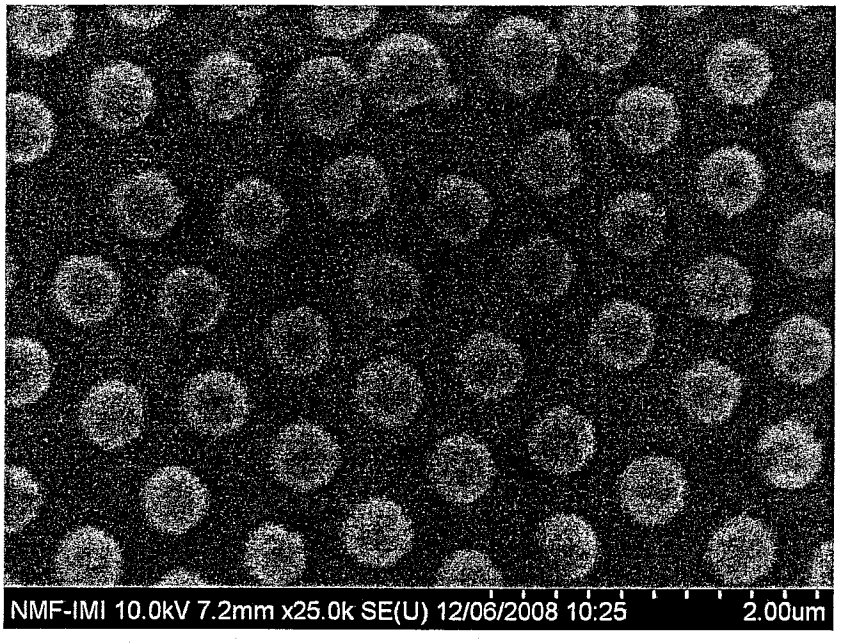

Figure 3.18: SEM image of the nanohole array fabricated by NSL.

The next picture is the image of the structure taken from a CCD camera of a confocal microscope. It shows the long range order structures. Some defect areas can be seen on the sample. These defects and their origin are going to be discussed in the next section. This structure is fabricated with 1 μm microspheres. Therefore, the period of the holes

is equal to the diameter of the spheres before etching (i.e. 1 μm).

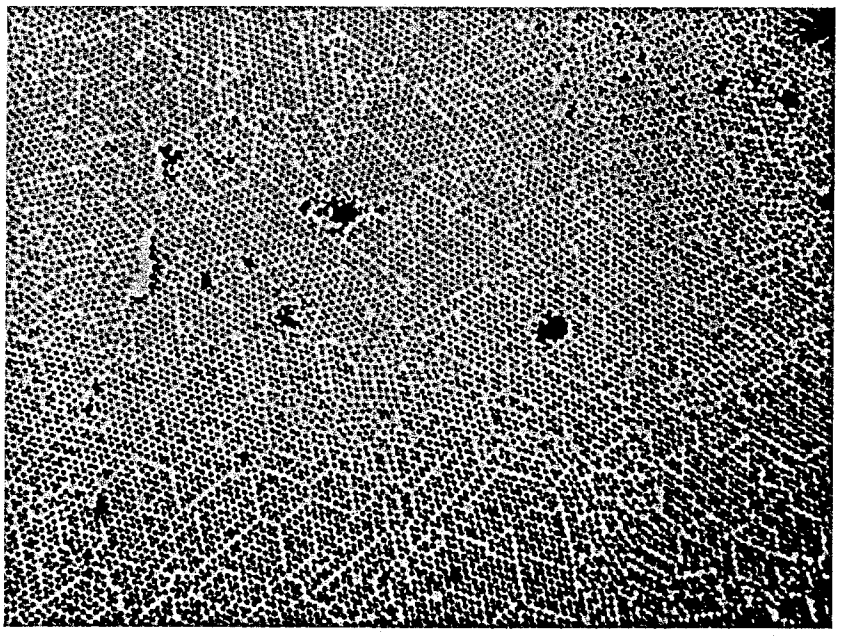

Figure 3.19: The nanohole structures after lift off of the spheres.

Figure 3.20 shows a sample obtained with a monolayer deposition of silica microspheres of 560 nm followed by deposition of Cr (5 nm) and Ag (100 nm). This image has been taken before the lift-off of the microspheres. One can however find on the right hand side of the picture two nanoholes of about 400 nm in diameter.

The sample shown in the following picture is a gold film with nanoholes arrays with a spatial period of 750 nm. In all of the samples shown in this section a thin layer of Cr with a thickness of about 5 nm is deposited under the gold /silver layer as interface layer to increase the adhesion of the gold or silver layer to the glass substrate.

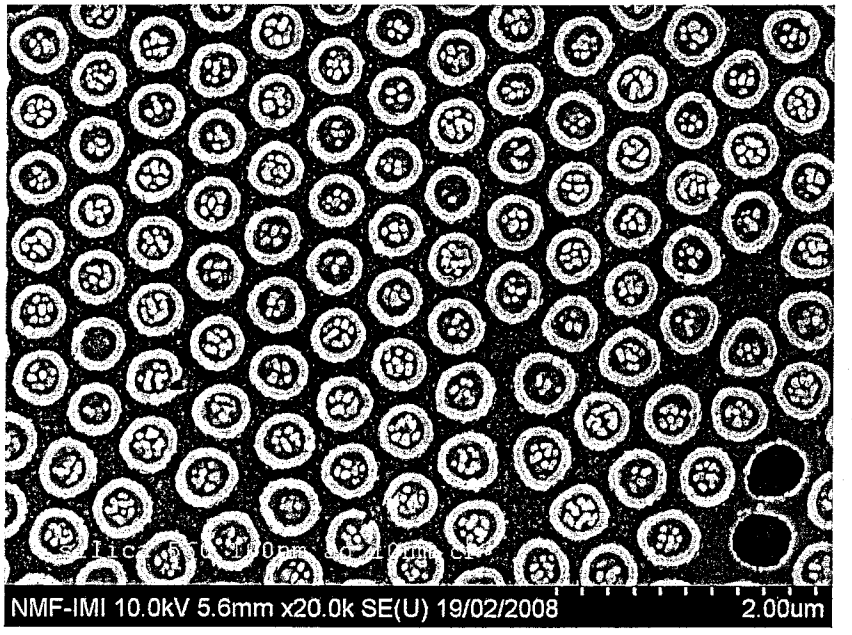

Figure 3.20: Sample of silica microspheres (560nm diameter)

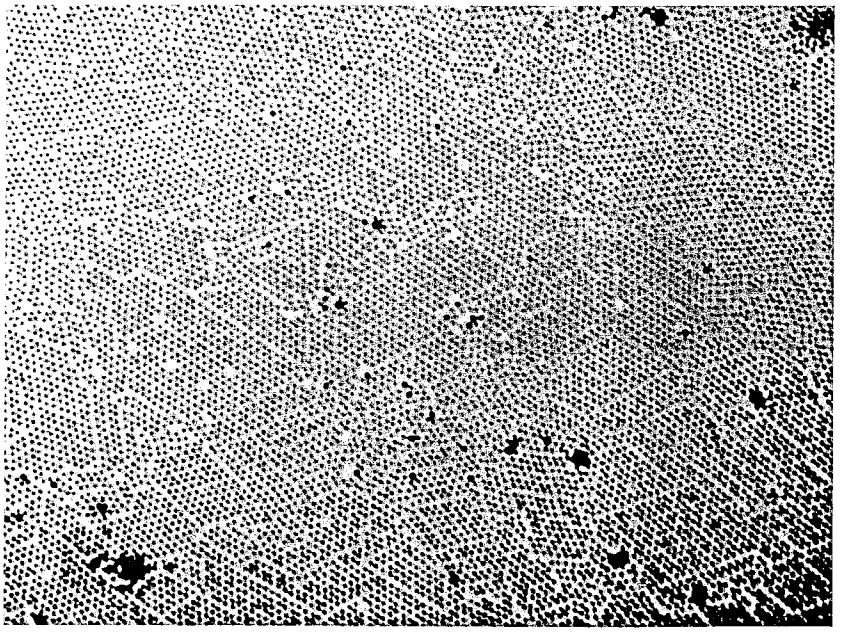

Figure 3.21: The final product of gold film perforated by NSL

3.3.3 Potential Structural Defects

Three groups of potential defects could occur in the structures fabricated based on the approach described above (NSL method). Two groups of defects are related to the structure of the array in the lateral directions. The template structures are either not completely covered by a hexagonal close packed (HCP) structure or exhibiting some multilayer regions. The third group is related to defects in the walls of the holes during the metallization.

a) Presence of the cracks on the monolayer microspheres template

Figure 3.22 shows structures fabricated on a template that is not completely covered by a monolayer of HCP microspheres. The uncovered regions are covered by the metal and the resulting structure can be characterized as a short range order nanohole array or sometimes as an array of random holes.

b) Template with multilayer regions

Presence of multilayer structure of the microspheres will result in the presence of some larger and random shape holes on the array region because the multilayer microspheres prevent the deposition of the metal on the glass substrate. Existence of some large holes on the structure is increasing the intensity of the transmitted light and results in less detectable peaks in the transmission spectrum due to the EOT. Some of these defects are shown in Figure 3.21. However, EOT can still be observed even by the presence of a limited number of these defects.

Unlike the EBL, in this method, as an advantage, the shape of each individual hole is not dependent on the position of the hole with respect to the center of the array regions. However, the etching condition by RIE will determine how uniformly the spheres are etched and consequently how good is the shape of the circular holes.

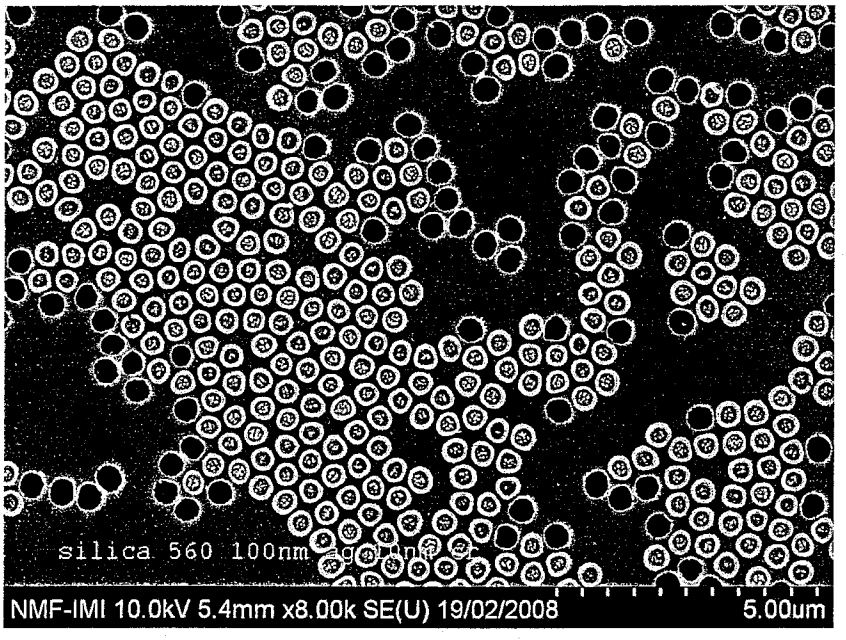

Figure 3.22: Random nanoholes structure (the SEM micrograph is taken before the lift-off of microspheres).

Non-uniform holes shapes which are shown in Figure 3.16 is a result of a RIE of the template by a mixture of O_2 / CF_4 as an etchant.

c) The defect in the holes wall

Metallization of the template of the etched microspheres is also a critical step that defines the shape of the wall of the holes. If the deposition of the metal is done by plasma sputtering, the shadow of the sphere would be covered by the metal. Hence, the holes structures would have bended walls rather than straight walls. To prevent a deformation of the walls, electron beam evaporation technique is used for the metallization of samples. In this method metal particles are deposited vertically on the template (i.e. snow-fall deposition). The rate of the deposition is also an important parameter to be adjusted to obtain a less granular surface. This process is depicted in Figure 3.23.

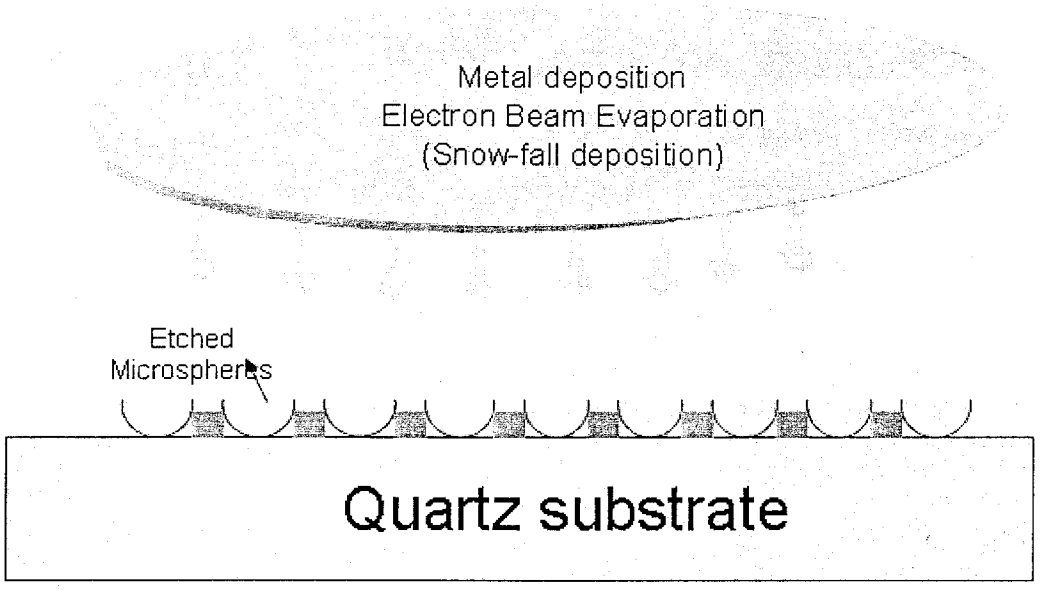

Figure 3.23: The process of metal evaporation (snow-fall deposition of metal particles prevents the penetration into the shadow region of the spheres).

3.4 Optical Measurements

Experimental measurements for the optical properties of the structures made of arrays of subwavelength holes are done both in bright-field and dark-field domain. The dark-field measurements are an appropriate choice where especially in the biological application the intensity of the background light is reducing the perceptual clarity and contrast of the images. However in the spectroscopic measurement the image of the sample itself is not the goal of the measurements. The basic challenges for an accurate measurement are in the control of the illumination light source in terms of the angle of the incident with respect to the sample and the position of the detector of the spectrometer. In the case of nanostructures of an array of subwavelength holes, it becomes even more challenging because the sample has to be placed at a precise position. Figure 3.24 shows two classical methods known as bright and dark field spectroscopy.

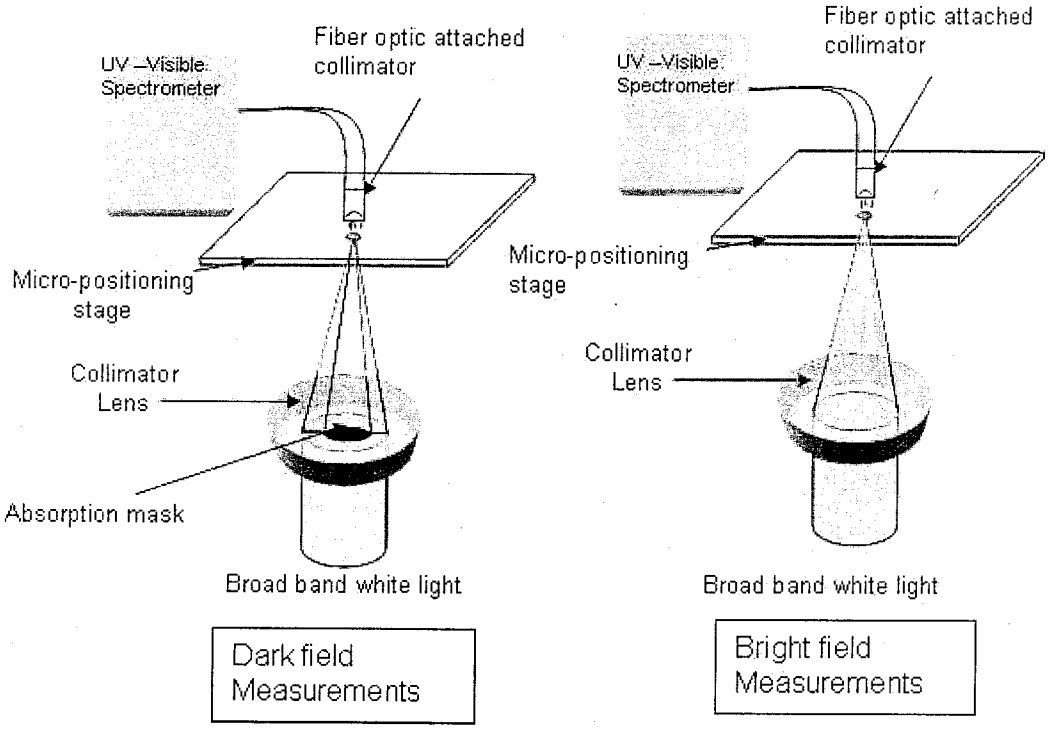

Figure 3.24: The classical optical spectrometry techniques

The setup used for the optical measurement of the transmission spectrum is shown in Figure 3.25. As it can be seen the micro-positioning stage is no longer required for the measurements. The specula reflection accessories used in this experiment provide a control on the spot size of the light for the samples of as large as 3 *mm*. Reference spectrum is measured using a smooth and optically thick film of gold or silver, corresponding to the material of the nanoholes structures.

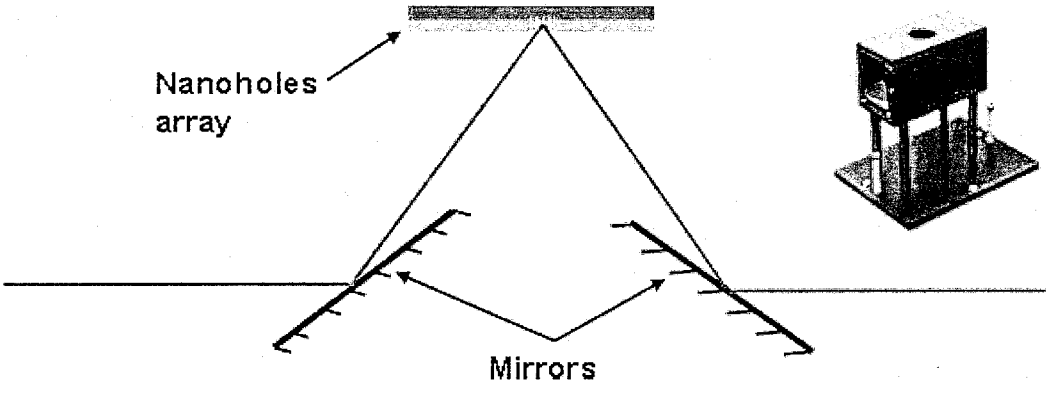

Figure 3.25: Optical setup for specula reflection measurement

The result of the measurement for a typical sample is shown in Figure 3.26. The transmission spectrum is for a sample of the gold nanoholes with a periodicity of 650 nm. The metal film thickness and diameter of the holes are 125 nm and 100 nm respectively. The sample is fabricated on a quartz substrate. The total area of the array is 3.5 mm^2. A shoulder and two peaks can be observed in the spectrum at 365 nm, 511.5 nm and 702.5 nm respectively. The shoulder in the spectrum would be related to the material properties of the metallic nanostructures while, as it is discussed in the next chapter, the second and third peaks would be defined by geometrical parameters of the structure and can in principle be tuned for specific applications.

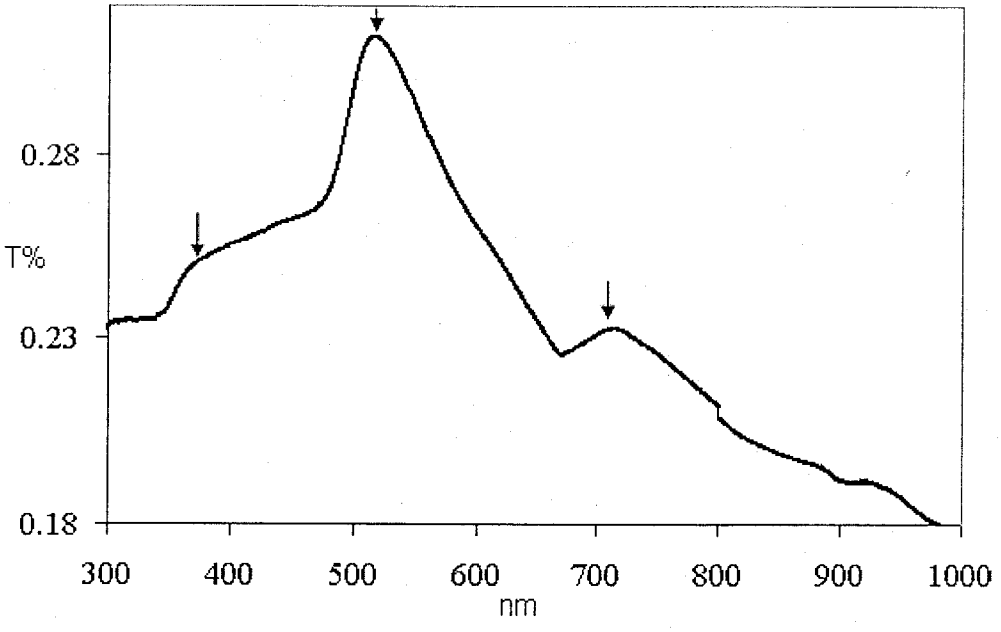

Figure 3.26: VIS-NIR transmission spectra for a long range order nanohole array (100 nm diameter nanoholes) on a gold film of 120 nm thickness. The array has a $3.5mm^2$ coverage and fabricated by EBL technique.

3.5 Conclusion

Two methods of fabrication for long range periodic nanohole structures have been proposed. The maximum area that has been successfully fabricated by EBL method is as large as 3.5 mm^2 whereas, the area of the fabricated structures based on the NSL can be as large as 10 mm^2. It has to be noted that EBL is an expensive and sequential fabrication method. However, such a technique can provide a wide range of options in terms of hole shape and diameters, spatial periods and crystalline orientations of the arrays, and the thickness and material of the metal films.

In the method presented based on NSL, the crystalline orientation of the structure depends on the structures of the template. Therefore, the crystalline orientation of the fabricated structures is more likely in a hexagonal close packed (HCP) orientation. Although a transition between the face centered cubic (FCC) and HCP orientations has been observed [83]. However, it has been suggested that the transition is promoted by the size polydispersion of the colloidal microspheres which can be prevented by using highly purified and monodispersed microspheres. For the structures fabricated by this method, pitch of the holes is defined by size of the spheres before etching and diameters of the holes are defined by the etching time of the monolayer template of the microspheres. Due to the anisotropic etching process of the microspheres, these two parameters can not be tuned independently. However, the availability and cost efficiency of the method outweight these limitations.

The potential structural defects associated with the fabricated structures are discussed and the roots of the defects are defined. The key role of the metal deposition by thermal evaporation in both methods is shown. Metallization by techniques such as sputtering which is not providing a snow-fall deposition condition results in a higher defect rate.

Spectroscopy measurements for optical characterization of the structures are largely

facilitated when structures are fabricated in long range order. Increased level of the energy transmission through the arrays reduces the effect of the shot noise in the detector of the spectrometers. As a result, the far field optical measurements is allowed by a conventional UV-VIS spectrometer. The latter is an advantage in the application of these structures when they are used as biosensors to increase the throughput of the measurement system.

Chapter 4

Numerical Calculations

4.1 Introduction

In the first two chapters of the thesis, a brief introduction is presented to define the EOT and its characteristics. It has been discussed that EOT occurs at some specific wavelengths of the spectrum. Position and shape of the peaks of the transmitted spectrum are prominently interesting for many applications based on this phenomenon. The shapes and positions of the transmission intensities are dependent on many parameters that can be categorized in three groups as following: 1) The geometrical parameters of the structures , 2) the material properties of the metallic films and the dielectric constant of the surrounding mediums, 3) the polarization state and angle of incident of the illuminating light. Therefore, a predictive model would be necessary to relate the optical response of the structures to these parameters. Investigating of the spectral behavior of the nanohole arrays for their transmission spectrum becomes even more interesting knowing that the fabrication techniques presented in Chapter 3 offer a wide range of options in terms of geometrical parameters for the fabricated structures and consequently a wide range of

optical response can be obtained.

Originally, it was presumed that EOT would be due to the excitation of collective oscillation of electrons on a surface with periodic holes. In this picture, Surface Plasmon Polaritons Bloch Waves *(SPP_BW)* which is simply referred as *SPP*, excited at the front side of the film, are transmitted to the back side of the film and reemitted again. This simple three phase mechanism for the transmission led to the first model based on coupling of the light to the *SPP* modes. However, the model failed to predict the peak positions of the transmitted spectrum accurately as many parameters such as thickness of the film and the shape of the holes were not considered [29].

So far, there are many different theorems that tried to explain the mechanism for transmission of the excited SPP from the front side to the far side of the film as well as for the total transmission process. These models, according to the authors involved and their interpretation, have been categorized as: 1- surface plasmon assisted transmission [2, 47, 84], 2- tunneling coupling effect [85, 86], 3- dynamic diffraction by the holes arrays [87, 88], 4- Fabry-Perot Like cavity resonance [89-91] and the most contradictive model as the constructive-deconstructive interference of composite evanescent surface waves [51]. Excitation of the *SPP*s due to interaction of light with the two dimensional array of nanoholes on planar surface of metallic structure is a common denominator of most of these models. The main differences is in how these *SPP*s are involved in the process of transmission and whether they are contributing to the transmission maxima or minima. The position of the minima in the spectrum is dominantly defined by the excitations of the *WA*s modes on the front and back side of the illuminated film [47, 50].

Besides *SPP*s and *WA*s modes, localized surface plasmon resonances *(LSPR)* is another optical modes that are excited and contributed to the overall transmission process. Effects of the holes shape on excitation of *LSPR* modes associated with individual holes

are studied in [62]. The shift of the peaks in the transmitted spectra due to the excitations of the *LSPR* subject to the change of the polarization state of the incident light and aspect ratio of the rectangular holes are reported [63]. This concept is also referred as shape resonance as it is studied in the [58, 63, 64, 68, 92]. It should be mentioned that effect of the *LSPR* is mostly investigated for non circular holes where the shape of the holes have a great impact on the excited modes. However, in this chapter, the role of these modes are studied for array with the circular holes.

In this chapter, a detailed analysis of the spectral behavior is presented. The impact of the *SPP*, *WA* and *LSPR* on the spectral characteristics of the transmission spectrum is studied and effects of geometrical parameters of the structures (i.e. thickness, diameter and period of the holes) on their excitation of the optical modes are shown. This investigation is conducted by applying numerical calculations using the finite difference time domain (FDTD) technique by implementing the Lorentz-Drude model for approximating the dispersion of metal in the visible range of spectrum.

The chapter is organized as following: The important geometrical parameters that can shape the transmission spectra are presented in the 4.2. In the third section the challenges that have to be faced in order to provide accurate results from the simulation is discussed. Results and discussion are presented in the fourth section. Comparative transmission spectra of the structures as a function of the material and each of the geometrical parameters are depicted and the important features are explained. In order to show the potential sensitivity that can be achieved by long range order nanohole array, a simulation is conducted and its result is presented in Section 4.5. Overall conclusion is made in the last section of this chapter.

4.2 Geometrical Parameters

The structure under study is an array of circular subwavelength apertures on an optically thick metal film. Choosing these structures for the analysis is inspired by two reasons. Firstly, for circular holes array, at normal illumination, the transmission process through a long range order array of circular holes would not depended on polarization state of the incident light. Secondly, the fabrication methods that are presented in third chapter and mostly the second method based on the NSL are tuned for the fabrication of the circular holes rather than the other hole shapes.

Based on the momentum matching argument presented in the 2.7, the *SPP*s and *WA*s modes for a hexagonal array of holes can be calculated by the equations (4.1) and (4.2):

$$\lambda_{spp} = \frac{P}{\sqrt{\frac{3}{4}\left(i^2 + ij + j^2\right)}} \sqrt{\frac{\epsilon_m \epsilon_d}{\epsilon_m + \epsilon_d}} \quad , \tag{4.1}$$

$$\lambda_w = \frac{P}{\sqrt{\frac{3}{4}\left(i^2 + ij + j^2\right)}} \sqrt{\epsilon_d} \, . \tag{4.2}$$

In these governing equations, P represents centre-to-centre distance between two neighboring holes or spatial period of structures, ϵ_m and ϵ_d are dielectric constant of the metal and i and j are two integer numbers representing scattering order of the optical modes. As these equations suggest, the *SPP* and *WA* modes are proportionally dependent on the period and the dielectric constants of the metal and the surrounding environment. Moreover, the *LSPR* modes which are excited at the rim of each individual holes are shape dependent optical phenomenon, therefore, for the circular holes, the diameter of the holes is a parameter that defines these modes. The transmission of the excited modes from the front side to the back side of the film would be dominantly influenced by the film thickness [93]. Therefore, the geometrical parameters for these structures that are going to be studied in the spectral behavior of the long range order nanohole arrays are the diameter

of the holes, the periodicity of the structures and the thickness of the films. Since The material of the films as well as the dielectric medium of the interface are also important parameters that are involved in the overall transmission spectrum, these parameters are also studied in this chapter.

Regarding the geometrical parameters, there are some general criteria that have to be considered. The diameters of the holes should be in the subwavelength order that guarantee no existence of any propagation mode and the apertures are not acting as waveguide channels. A film of nanohole array is considered as optically thick when the thickness of the film is several times more than the skin depth of the film in the visible range of the light. The skin depth of the noble metals in the visible spectrum is in order of 20 nm. The apertures are in wavelength-scale proximity to each other. The periodicity of the structures should be in the wavelength range from the visible to the near infra red (i.e. 500 nm to 1.4 μm). All the structures are considered as long-range periodic structures (i.e the the structures is bounded by periodic boundary in two dimensions). It should be mentioned that short-range periodic structures have also been investigated [58] but they are beyond the scope of this study.

4.3 Methodology

In order to investigate the role of the geometrical parameters with respect to the scattering modes and hence to the overall transmission spectrum, transmittance spectra as a function of the geometrical parameters is analyzed. The time domain numerical calculation of the Maxwell equations such as FDTD method can be used to obtain spectra of various types over a range of wavelengths or frequency from a single calculation. The spectra are obtained by complex Fourier transformation of the time-domain field components,

Poynting vectors, at the range of the frequencies of interest to yield complex, frequency-resolved fields, the absolute magnitude of which can be associated with time-averaged intensities.

The light intensity of the transmission spectrum, $T(\lambda)$ is calculated by integrating the Fourier coefficient of the Poynting vectors associated with the EM field distribution at the far side of the film over an observation area as big as the unit cell of the periodic structures. The transmission spectrum is given by

$$T(\lambda) = \int_{\Omega} S \cdot d\vec{n} \tag{4.3}$$

where the S is Poynting vectors of the field, Ω is observation area, $\vec{n}$ is the normal vector to the surface of the observation area. The Poynting vector $\vec{S}$ is representing the flux of the energy and defined as following:

$$S = \vec{E} \times \vec{H} \ . \tag{4.4}$$

As much as the FDTD is an appropriate method for spectral analysis, implementation of the dispersion of the metal is a challenging task that has to be addressed for an accurate time domain calculation of plasmonic structures. Although some of the previous investigations had the transmission spectra calculated while ignoring the dispersion of the metals [94,95], the recent studies showed that this could lead to wrong results and conclusions [96]. Frequency domain methods have an advantage over time domain methods with respect to dispersive material. In time-domain methods, the dispersion property of metals have to be approximated by suitable analytical expressions whereas in the frequency domain solutions the actual permittivity of the metal in each frequency is applied to the calculations. In most cases the Drude model is used to characterize the frequency dependence of the metallic dielectric function. Permittivity in the metal by Drude model is given by

$$\epsilon_{r,D}(\omega) = 1 - \frac{\omega_p^2}{\omega^2} \tag{4.5}$$

Where ω_p is plasma angular frequency and ω is the are angular frequency of the excitation electromagnetic field. However, the Drude model approximation is valid over a limited wavelength range [40] and for noble metals such as gold and silver it is not very accurate in the visible spectrum. The range of validity of the Drude model can be extended by adding Lorentzian terms to Equation (4.3) to obtain the Lorentz-Drude model given by:

$$\epsilon_{r,LD}(\omega) = \epsilon_{r,Drude}(\omega) + \sum_{j=1}^{K} \frac{f_j \omega_p^2}{(\omega_j^2 - \omega^2) - i\omega\Gamma_j} \tag{4.6}$$

where ω_j, f_j and Γ_j are the resonance frequency, strength and damping frequency, respectively, of the J^{th} resonator. Physically, the Drude and Lorentzian terms are related to intraband (free-electron) and interband (bound-electron) transitions respectively [40].

In FDTD method the electromagnetic equations is solved by discretization of the space and time. Choosing the right grid size is critical to obtain the accurate results. The discretization of the time and space are related to each other by a parameter named Courant number S. It is a number between 0 to 1. In order to insure the stability of the algorithm and prevent the numerical dispersion in the results this parameter is set to 0.5 in our calculation. This will yield a convenient relation :

$$\Delta t = \frac{\Delta x}{2C} \tag{4.7}$$

which specifies that it takes two time steps ,Δt,for a wave front to cross one cell ,Δx. In the simulation of plasmonic structures in general and specifically in the simulation of circular nanohole arrays the grid sampling must be sufficiently fine to avoid numerical dispersion and instabilities in the simulation. *LSPR* and *SPP* modes excited by the holes have oscillation length of the order of 10 nm so the grid size should be fine enough to capture them. This constraint will result in a very fine time step in the calculations as well. Overall performing of the simulation with tuned parameter to obtain accurate results is a time consuming task depending on the computer power that can be dedicated to the simulation.

4.3.1 Simulation Setup

Optical simulation of the SW gratings was carried out using the OptiWave software package based on a FDTD numerical modeling approach. OptiWave solves Maxwells curl equations to compute the electromagnetic field components of a 2D or 3D mesh grid and time step size [42]. In this simulations, a system consisting of a stand alone metal layer of gold (Au) film symmetrically surrounded by air is presented in Cartesian coordinates X, Y, and Z. We examine surface plasmon excitation and propagation on the film surfaces, and transmission of light into the air. While we investigated numerous variations on the system parameters, all of the numerical results presented correspond to either gold (Au) or sliver (Ag) films with thickness= 425-200 nm, diameter = 400-200 nm and, for hexagonal and square arrays, lattice spacing P = 1.4 μm to 920 nm. The broad band white light as incident source is required in this calculation to contain all range of frequency in the incident light. This source is implemented in these simulations by considering a perfect plane wave laser source as incident wave being multiplied by a Gaussian pulse in time domain in order to obtain a pulse that contains information over a desired range of wavelengths.

To implement the infinite periodic structure, first a unit cell is defined based on the desired crystalline orientation, as they are presented in the Figure 4.1, then, it is bounded by periodic boundary conditions. The computation domain is limited by periodic boundary conditions in the dimensions X and Y. In the Z direction, it is bounded by perfectly matched layers. A grid size of 5 nm is used to discretize the computation domain to the uniform 3-D array of cells. The source and observation areas for transmission measurements are located as far as 500 to 600 nm distance in two sides of the film. It has been discussed before that the best coupling of the SPP modes will occur when the 2 sides of the hole array are covered by materials with the same index of refraction [86].

Therefore, in this work the computation domain is symmetric in the z direction with respect to the film (i.e. the structure is a stand alone nanohole array film).

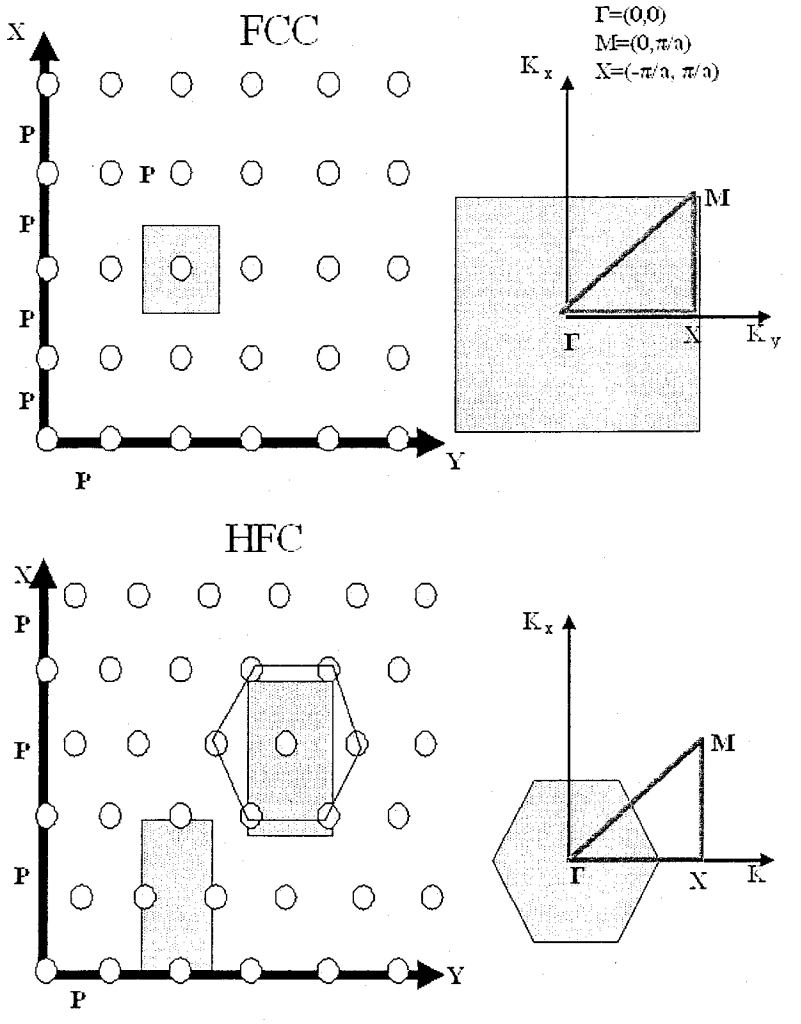

Figure 4.1: The first Brillouin zones of the crystalline structures of face cubic centre (FCC) and hexagonal face centre (HFC).

4.3.2 Computation Domain

A typical computational domain is shown in Figure 4.2. This schematic is shown in two dimensions, as it is appeared in the simulation environment, however, the actual structure is simulated in three dimensions. The third dimension ,Y, is not shown in this figure. The spatial period of the structures is defined by X and Y which in the structure shown in this schematic is 700 nm. The computation domain is terminated in Z=0 and Z=2000 nm by introducing these boundaries to perfectly matched layers. The thick bulk of the vertically positioned structure in the picture is representing the metallic structure.

The vertical line that is attached to an arrow pointing to the left (red line in colorful image) is defining the position and direction of the light source. The two vertical lines at the right and left hand side of the domain are the observation areas which are used for calculations of the reflection and transmission spectrum respectively.

A $3-D$ presentation of the structure is shown in Figure 4.3. This is a X-Y cross section view of the nanoholes array structure with a HCP crystalline symmetry.

4.3.3 Field Distribution

The distribution of the electromagnetic field in the front side of the films and the penetration of the evanescent modes through the holes is clearly illustrated in Figure 4.4. In this , holes are circular holes and the array in square lattice orientation. The cross section view of a unit cell is showed in Figure 4.4 and the white rectangular shape is the position of the hole. The centre to centre distance and diameter of the holes are 600 nm and 100 nm respectively. The thickness of the film is set to 125 nm. A film of gold is used in this simulation and source is implemented as plane wave broad band white light to contain the whole spectrum from the visible to the NIR range.

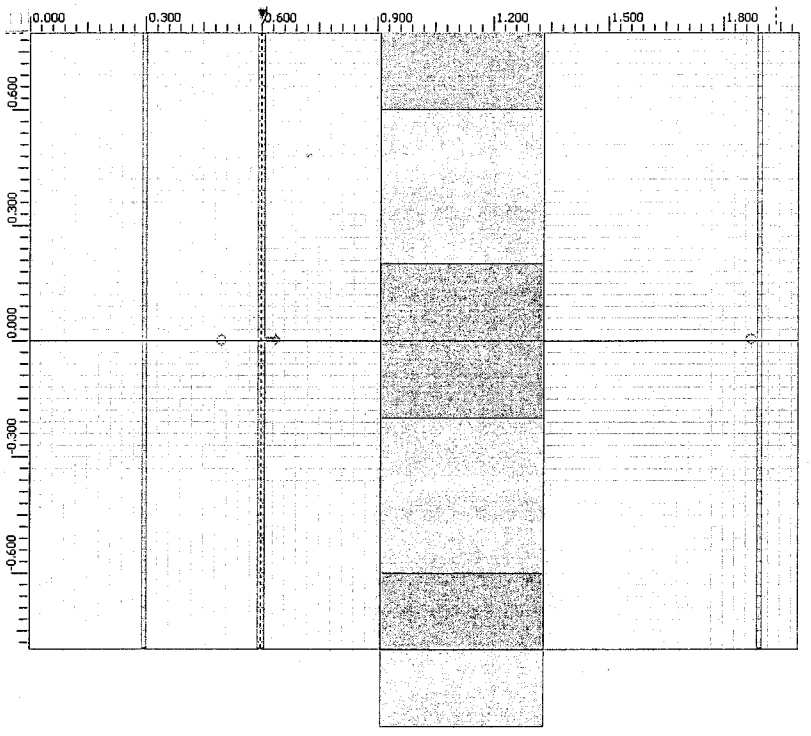

Figure 4.2: A typical computation domain used for the numerical calculation. The dimension lengths presented in microns.

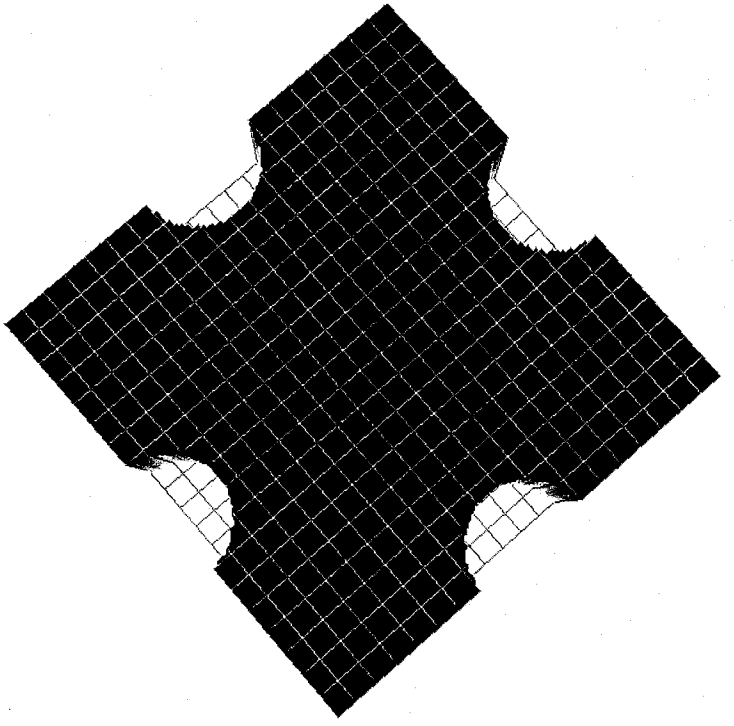

Figure 4.3: Three dimensional view of the unit cell of the structure under study.

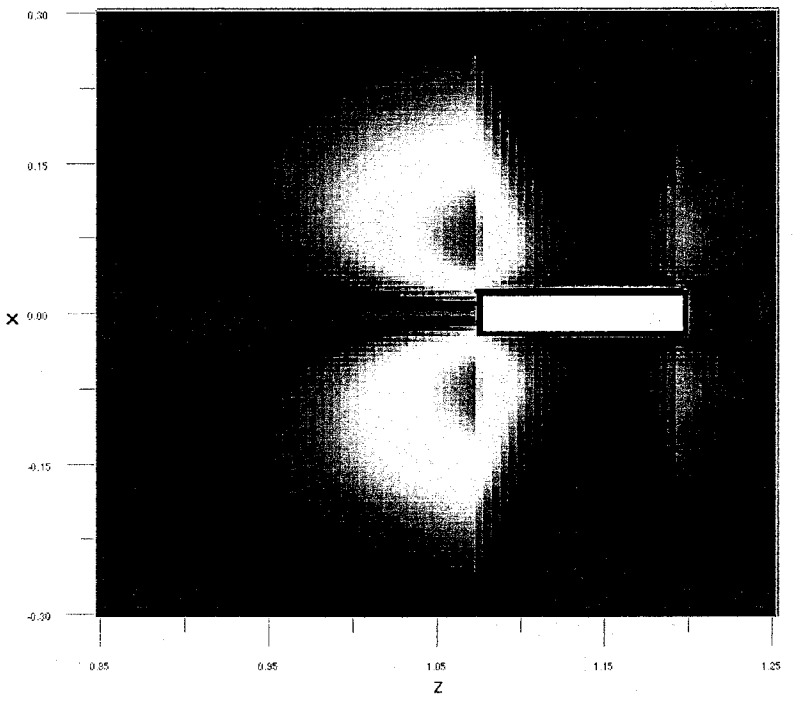

Figure 4.4: The distribution of the electromagnetic field, a cross section view. Source is at the left side of the film. The propagation of the evanescent modes in the front and back side is shown. The dimension lengths presented in microns.

4.4 Results and Discussions

Five set of calculations are presented in this section. Transmittance spectral analysis by changing the three basic geometrical parameters is presented in sub sections 4.4.1 to 4.4.3. In 4.4.4 the analysis is repeated for the structures made of silver, subject to the change of periodicity. The result is interpreted based on the excitation of existing *SPP* and *WA* modes. The effect of the *LSPR* on the rim of the holes is investigated on the overall spectrum features.

4.4.1 Change of Diameter

Optically thick film of thickness 425 nm is perforated by the holes with a periodicity of 1 μm. The diameter of the holes is changing from 200 to 120 nm in the calculation done for transmission spectrum. The incident light is a broad band source of white light. The diagram in Figure 4.5 is depicting the comparative spectrum of each structure in visible to near infrared regime.

According to the model described by equation (4.2) the position of the peaks have to remain constant because the period of the structure is not changing, although the edges of the holes are going to be closer to each other while the diameter of the holes increased as illustrated in the next figure. Figure 4.6 shows the top view of the film. By increasing the diameter of the holes, the centre to centre distance of the holes is not changing while the rims of two adjacent holes are getting closer.

The position of the first and the second peaks are listed in the Table 4.1 and marked by arrows in the Figure 4.5. The first peak is steady at the same position, 480 nm while the second peak is experiencing a red shift. According the SPP model for transmission, there would be no shift in the peak positions. This calculation proves again that the momentum matching model would not be an accurate model. The first peak is not shifting, implying

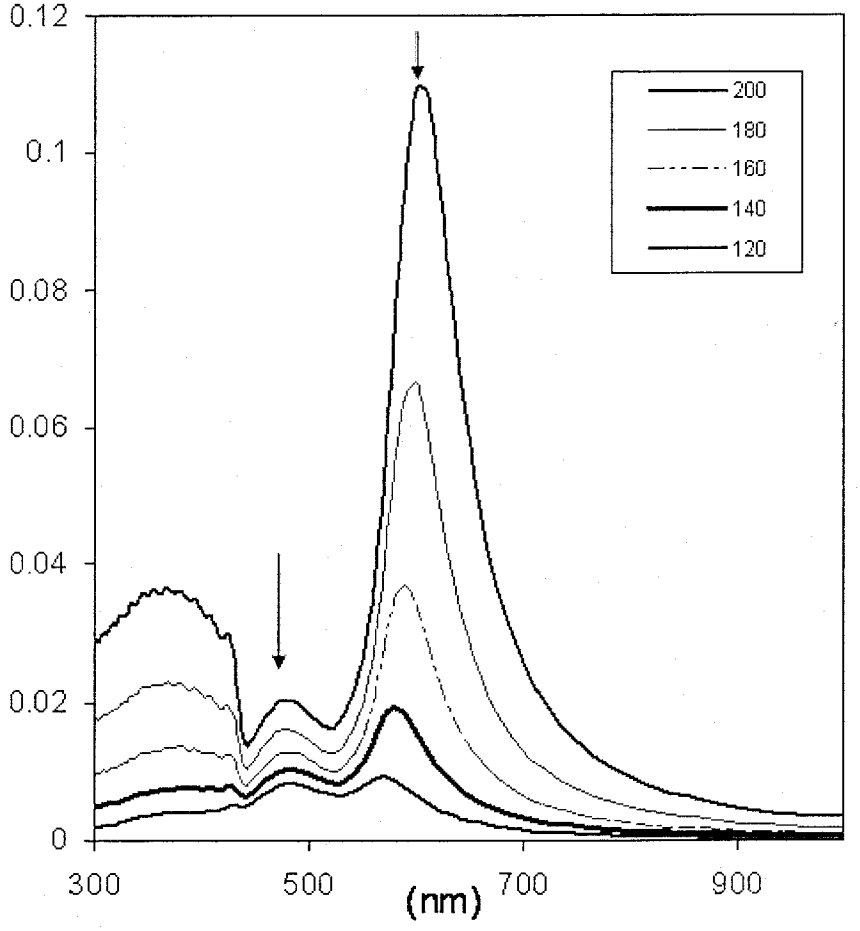

Figure 4.5: Transmission spectrum of the gold films as a function of the diameter of the holes (Y axis is the transmission, intensity of transmitted light normalized to the intensity of incident light, versus wavelength of the incident light in X axis).

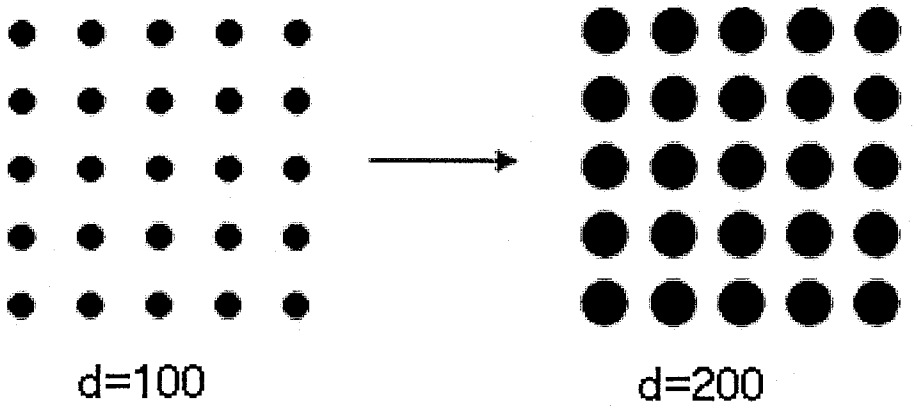

Figure 4.6: Schematic top view of the array of subwavelength holes while the diameter of the holes is changing from 100 nm to 200 nm. The rim of the holes is closer to each other.

Table 4.1: Position of the peaks as a function of the diameter of the holes

Diameters(nm)	peak1	peak2
200	480	560
180	480	570
160	480	580
140	480	590
120	480	600

that the *SPP* and *WA*s excited at the surface are mainly shaping the first peak of the transmission spectrum while the wavelength shift and the increased amplitude in the second peak would result from the *LSPR*s excited at the rim of the holes. The larger is the hole the higher is the average charge accumulation at the rim of the holes in the form of symmetric and asymmetric bands, resulting in a stronger mode coupling at both sides of the film.

4.4.2 Change of Thickness

Arrays of the subwavelength holes are milled on the planar film of gold. The periodicity of the structure and the holes diameters are set at 1400 nm and 300 nm respectively. The

thickness of the film is changing from 425 nm to 125 nm. As mentioned before, the sweep of the thickness is selected in such a way that films can be considered optically thick. Thinner film structures are not in the scope of this thesis, although, they exhibited interesting properties in form of *LSPR* absorptions. They have been investigated experimentally and theoretically by others [74]. The comparative diagram for the transmission spectrum as a function of the film thickness is shown in Figure 4.7. The diagram covers the wavelength range from 550 nm to 1 μm where the two peaks are located. The intensity of the second peak is increased with a decreasing thickness, a likely effect of stronger coupling of the *LSPR* modes at the front and far sides of the films. Table 4.2 is summarizing the position of the two peaks, showing a 53 nm red shift for the second peak. When the thickness of the film is changing, the lateral characteristics of the structure are not changing. The periodicity, the shape and the diameter of the holes remain constant for all structures while the transmission spectra are calculated. The excited modes of *SPP*s and *WA*s at the surface of the film are features of the lateral characteristics of the structures; therefore, the expectation is that they are going to be the same for different structures. There is no direct photon tunneling or propagation inside the holes. There are two features in the diagram that can be discussed here: I) the spectrum feature at shorter wavelengths than the second peak (below 750 nm) remains at a fixed location. The positions of the first and second peaks are listed in the Table 5 showing that the first peak is indeed experience a very small shift. It would indicate that the *SPP* and *WA* modes are only manifested in the shorter wavelength region of the spectrum, II) the shift in the position and the change in intensity of the second peak are also the other interesting feature of the spectrum. According to Equation (4.1) there should be no shift in this peak as it was the case for the first peak. The effect of the *LSPR*, which is ignored in the *SPP* model, is elaborated in this calculation, showing how the change in the coupling of *LSPR*s excited at the rim of individual holes is affecting the overall spectrum.

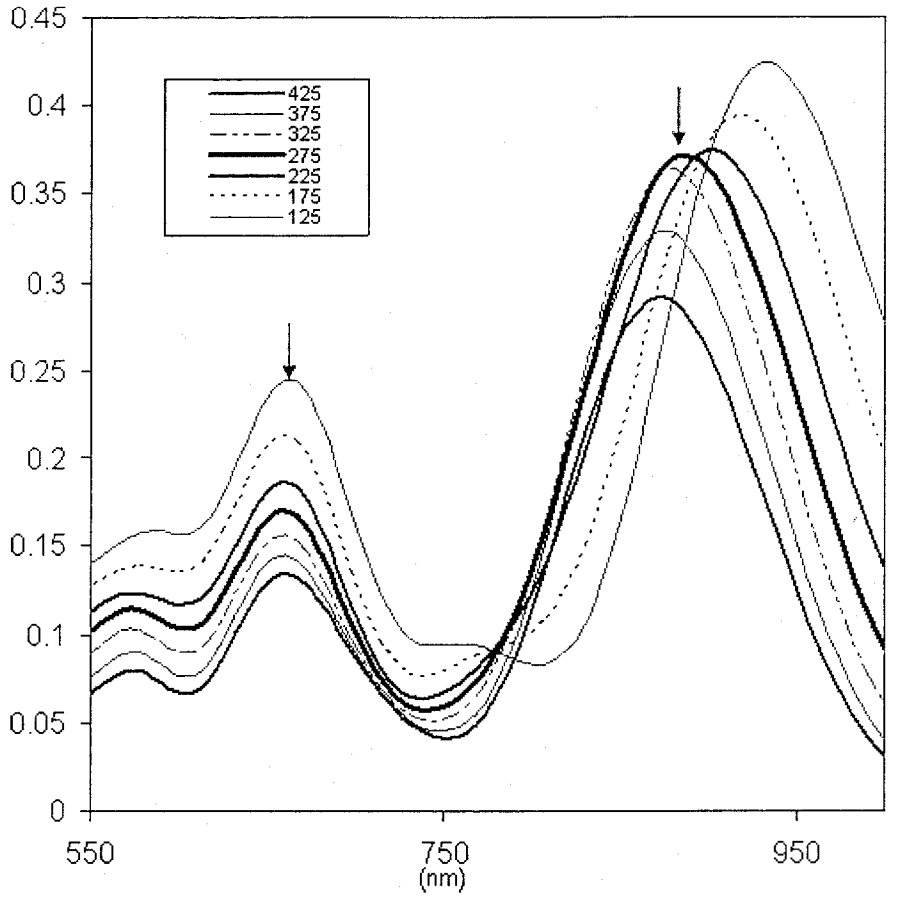

Figure 4.7: Transmission spectrum of the gold films function of the thickness (Y axis is the transmission, intensity of transmitted light normalized to the intensity of incident light, versus wavelength of the incident light in X axis).

Table 4.2: Position of the peaks as a function of the thickness of film for gold

Thickness(nm)	Peak1	Peak2
425	666	877
375	652	877
325	652	877
275	652	877
225	660	903
175	660	920
125	660	930

4.4.3 Change of Periodicity

Planar films of gold with thickness of 425 nm are milled with circular holes of 200 nm radius in a HFC crystalline structure. The centre to centre distance (periodicity) of the holes is changed from 1400 nm to 1000 nm. Figure 4.8 depicts the comparative transmission spectra for various periodicities. As it has been discussed in 4.4.2 and 4.4.1, the cut-off frequency or the longest wavelength of the transmitted modes is mainly influenced by the hole shape and size which defined *LSPR*s excited at the rim of the holes. The *LSPR* modes excited at the rim of the individual holes, contrary to the *WA* and the *SPP* modes, remain unchanged when the shape and the size of the holes remain the same [62]. The diagrams in the Figure 4.8 are confirming the same conclusion. While the hole shape and size is constant the falling edge of the second peak remains unchanged.

Equations (4-2) and (4-3) indicate that the peak and dip positions of the transmitted spectrum corresponding to the *SPP* and *WA* modes will shift as the periodicity changes (λ_{WA} and λ_{SPP} being directly proportional to the period). In Figure 4.8, the peaks 1 and 2 are marked by $\downarrow$ and the dip is shown by $\uparrow$ arrows. The first and second peaks of the spectrum are shifting toward red with increasing periodicity. They are very close and overlap when the period is shorter than 1.080 μm. The red shift of the peak positions in the spectra as a function of periodicity is shown in Figure 4.9. The interesting result that has been observed from these calculations is the proportionality of the red shift with the increase in the period.

The peak 1 (at shorter wavelengths) and the peak 2 (at longer wavelengths), are associated with (1, 1) and (1, 0) scattering orders respectively. The momentum matching model suggests that the change of the peak positions in the transmission spectra are inversely proportional to:

$$\sqrt{\frac{4}{3}(i^2 + ij + j^2)}\,. \tag{4.8}$$

where (i, j) are scattering orders. This predicts that the rate of linear shift in peaks with respect to the hole periodicities for $(1, 1)$ to be smaller than that for the $(1, 0)$ peak. The results observed in our calculation (shown in Figure 4.9) contradict the above prediction. Not only the shift in the position of the second peak is not linear but also the rate of the change in the first peak is larger than the rate of shift in the second peak.

The increase in the intensity of the second peak is consistent with the higher filling factor associated with the shorter periodicity of the structures.

4.4.4 Change of Material

Transmission spectra for the silver films with respect to nanostructure periodicity with the same geometrical parameters defined in section 4.4.3 are calculated and plotted in Figure 4.10. Silver is known as a material with less absorption in the visible range as compared to gold. For both silver and gold the imaginary part of the dielectric constant ($\epsilon"$) which is related to the dissipation (or loss) of energy within the medium are depicted in Figure 4.11 [97]. As it can be seen for the most part of the range of the visible spectrum the value for $\epsilon"$ for silver is less than that for gold which can be translated as the longer propagation lengths of the *SPP*s.

In terms of the shift in the position of the peaks, the silver film of nanoholes array follows the same trend discussed in section 4.3 for the gold films (the red shift due to increasing period). However, as it can be observed from Figure 4.10, quantitatively, peak 2 is not shifted with the same rate of the peak 1. Furthermore, there are two other interesting features that can be pointed out from this diagram. One is related to the change of the shape of the peaks as the period is changing. Peak 1 is sharper for shorter periods and it becomes broader as the period increases. In contrary peak 2 becomes narrower as the period increases.

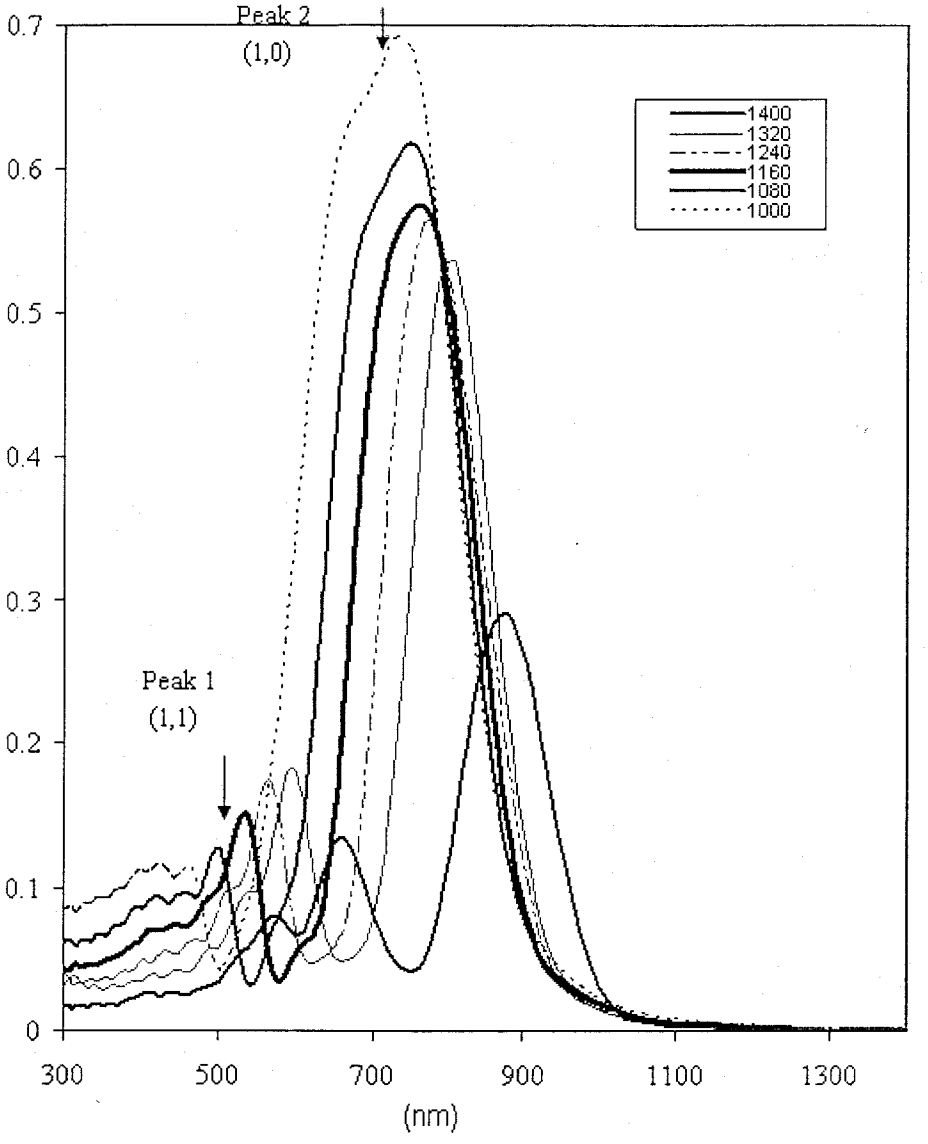

Figure 4.8: Transmission spectrum of the gold films as a function of the period of the structure (Y axis is the transmission, intensity of transmitted light normalized to the intensity of incident light, versus wavelength of the incident light in X axis).

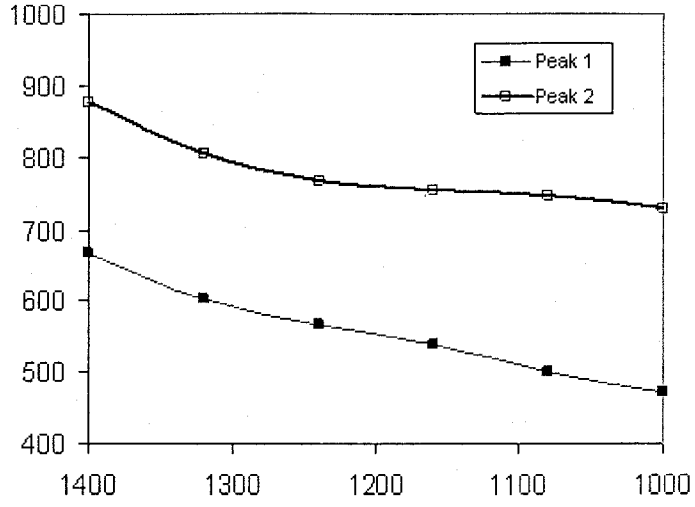

Figure 4.9: Peak positions of transmitted spectrum versus the periodicity of the nanoholes (Y axis is the position of the peaks versus X axis for the spatial period of the holes).

Secondly, the positions of the minima in the spectra are shifting with the period of the structure. It could be anticipated from equation (4.5) that the modes of the *WA*s are directly proportional to the period of the structures. Figure 4.12 is showing the linearity of the shift of the dips both for gold and silver. The fact that the dip position is linearly shifting both for gold and silver independent of the films material is consistent with the model presented in equation (4.5) and confirms the idea that the dips in the spectrum are related to the *WA* modes excited at the illumination surface.

4.5 Simulation of Sensitivity of Long Range Order Nanoholes Arrays

It is shown that this structure could potentially be used as sensing element in biosensors and they could increase the sensitivity of the sensors to 800 nm/UIR, contrarily to the small size array of nanoholes with 330 to 400 nm/UIR [7].

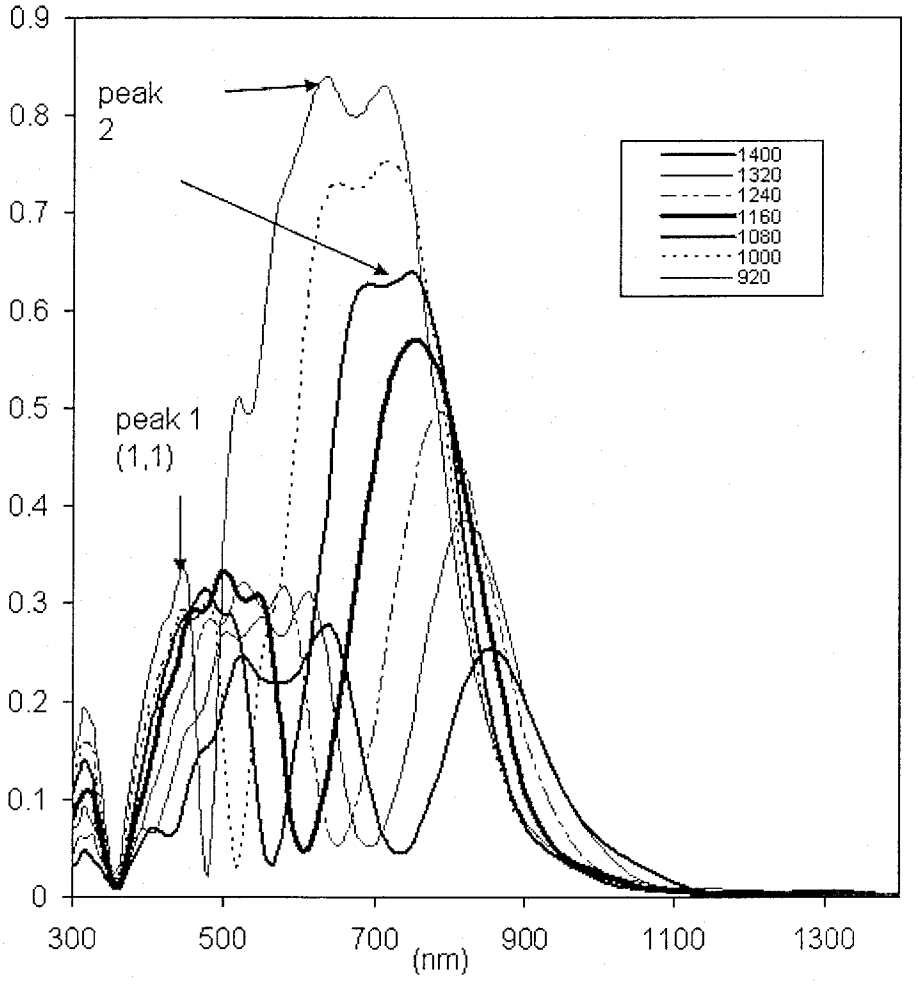

Figure 4.10: Transmission spectra of the silver films as a function of the structure period (Y axis is the transmission, intensity of transmitted light normalized to the intensity of incident light, versus wavelength of the incident light in X axis).

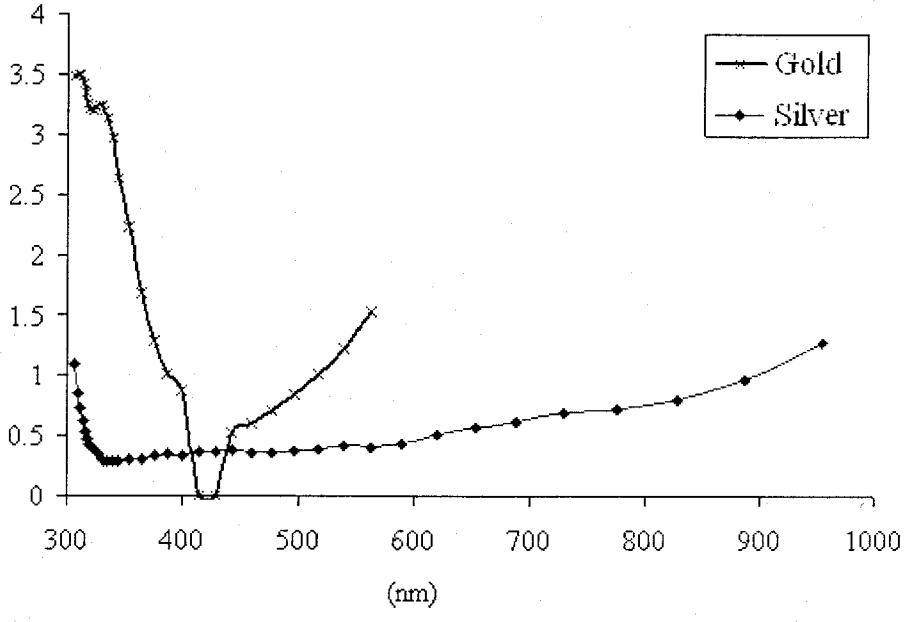

Figure 4.11: The imaginary part of the dielectric constant (Y) versus the wavelength (X). The data are taken from [97].

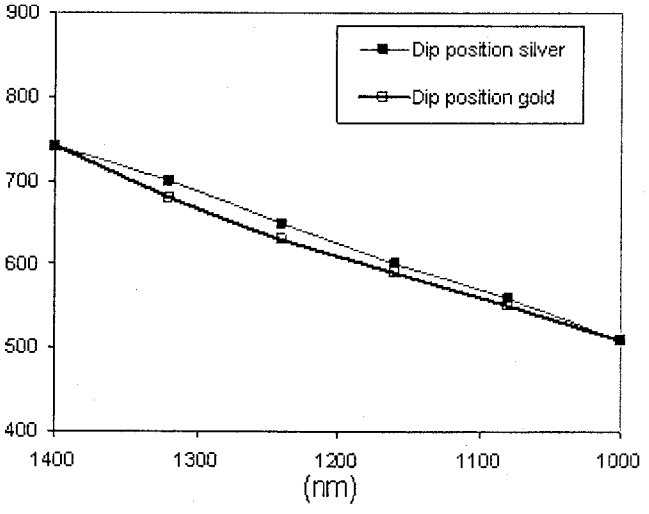

Figure 4.12: The position of the dips in the transmission spectrum (Y) versus the period of the structures (X).

A numerical calculation for the field distribution has been carried out using a 3-D FDTD method. The simulation results shown in Figure 4.13 are the transmission spectrum for a structure with a periodicity of 650 nm and a hole diameter of 100 nm on a film of gold with 120 nm thickness. The thick line shows the spectrum when the structure is exposed to an environment with a refraction index of 1.43 whereas the thin line depicts the spectrum when the ambient refraction index is 1.33. A shift in the spectrum is clearly demonstrated. The shift in the spectrum with regard to the same peaks of the same order is different. The first peak shows a smaller shift compared to the third shift in the third peak. The sensitivity of the second and the third peak have been determined to be as following:

$$S_2 = 460nm/UIR \quad ; \quad S_3 = 800nm/UIR$$

While the sensitivity is defined as:

$$S = \frac{\partial \lambda_{max}}{\partial n_{amb}}$$

where n_{amb} is the index of refraction of the ambient environment.

These values are found to be particularly high, suggesting the potential biosensing applications of the long range order nanohole arrays. The shift of the peak positions of the transmission spectrum due to the change of the index of refraction of the ambient environment for the third peak is larger than the second peak, the intensity of the transmitted light for the second peak is about 50% more than the one for third peak. In order to be able to sense the shift of the peak position of the third peak one need to increase the total energy of the transmitted light by increasing the total number of the holes. In long range order nanoholes arrays, the total energy transmitted through the array is increased. Therefore, the third peak is potentially detectable. Moreover, as it could be observed the simulation and experimental results in Figure 3.26 are in good agreement, suggesting that the effect of the boundaries on the transmitted spectrum is reduced.

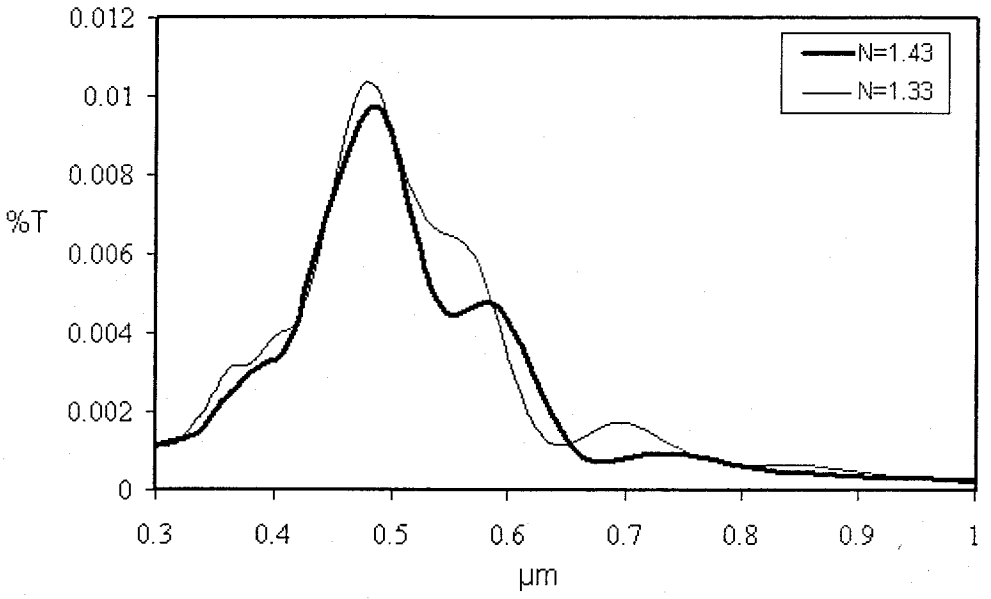

Figure 4.13: The simulation results of the sensing properties of the long range order of nanohole arrays.

4.6 Conclusions

The complex behaviour and characteristics of the transmitted spectrum of the array of nanoholes are related to three scattering modes, namely the localized surface plasmon resonance excited at the rim of the individual hole ($LSPR$), the surface plasmon polaritons Bloch waves on the flat surface of the metal and a third mode known as the Wood anomaly (WA). The simulation conducted on the field distribution provides the following insight on the spectral behaviour:

1. The cut-off frequencies of the transmission are mostly defined by the $LSPR$ at the rim of the holes rather than periodicity of the structures. The thickness analysis showed that the increase in the thickness is decreasing the cut-off frequency.

2. Wood-Rayleigh anomaly which is associated to the diffracted light on the surface of the film due to interaction of the light to the two dimensional periodic grating

of the metal film is mainly defining the minima in the spectrum. The position of the minima in the spectrum is affected by the index of refraction of the surrounding medium and the period of the structure. Linearity and proportionality of the *WA* modes is consistent with the model described by (4.1). The correlation between dips in the spectra with the *WA* modes is investigated and it is confirmed that the *WA* modes are related to the dips in the spectra independent of the films material and directly is proportional to the period of the holes.

3. The *SPP* wave is dominantly characterized by the diameter of the holes and the periodicity of the structures. The high frequency modes, features of the first peak in the spectrum, are mostly affected by *SPP* and *WA* at the surface of the film.

4. The sensitivity of the long range order nanohole structure as it is shown in the simulation results could be potentially as much as 800 nm of shift for change of 1 unit of index of refraction.

Chapter 5

Conclusion and Further Directions

5.1 Conclusion

Periodic structures consisting of a thin metallic film perforated with an array of nanoscale holes exhibit extraordinary light transmission (EOT) when the size of the holes is in the range of the sub wavelength, e.g. for the visible light, the size of the holes should be in the range of 100-250 nm. This simple optical structure has opened a wealth of opportunities for potential applications, from optical switches and photolithography masks to sensing applications. EOT will occur at specific frequencies imposed by the geometrical parameters of the structure, polarization, angle of incident light, and permittivity of the surrounding medium. Periodic arrays of holes in an opaque metal film have found many applications owing to the simplicity with which their spectral properties can be tuned on. They will act as filters for which the transmitted color can be selected by merely adjusting the period. Periodic metallic structures can convert light into SPs by providing the necessary momentum conservation for the coupling process. Therefore, a periodic array of subwavelength holes can give rise to the extraordinary optical transmission phenomenon

where the transmission spectrum contains a set of peaks with enhanced transmission even when the individual holes are so small that they do not allow propagation of light.

Fabrication of a metal film that exhibits plasmonic effects in the visible spectrum is a non-trivial task. In order to maintain photon-plasmon coupling in the structure they have to be patterned to nanoscale sizes. The structure should be periodic and well ordered, with a minimum number of defects in order to observe the best reproducibility of the optical response with different samples. The distance between the apertures should be uniform as well. An accurate control of the surface topology is important, especially for biomedical applications.

Contribution from the diffracted surface waves will become more important on a large ordered array of holes. Increasing the number of holes in the well ordered nanostructure array will increase the total energy transmitted through them. Hence, their optical properties will be measurable through classical methods such as UV-visible spectrometry, instead of the very tedious techniques necessary nowadays for the optical characterization of these nanostructures, such as dark field or near field measurements.

In this dissertation, two new methods for fabrication of the long range ordered nanostructures are studied and the EOT phenomenon is investigated experimentally and theoretically. Simplicity of the optical measurements and elimination of the boundaries effects was one of the motivations to develop these structures. The existing techniques for fabrication of the short range ordered nanoholes arrays are not trivially applicable for fabrication of long range ordered arrays since they are generally sequential and low throughput methods.

In one of the approaches an electron beam lithography (EBL) followed by a double lift-off technique is applied to obtain a uniform structure of nanohole array with large area of coverage. We have successfully fabricated samples with areas up to 3.5 mm^2. The detail of this 8-step fabrication method is explained in Chapter 3. Using this method, various

samples with films of Ag/Au, thickness of 70 to 120 nm, the circular hole's diameters of 100 to 150 nm and array's periodicity of 450 to 700 with the FCC lattice symmetry are fabricated.

The second method is based on nanosphere lithography (NSL) technique to fabricate hexagonal close packed (HCP) nanohole arrays on large area on a metallic film of Au or Ag films with a thickness of 50 to 100 nm. Periodicity of the structures fabricated by this method is defined by the diameters of the microspheres used in the fabrication of the templates. In this research, microspheres of 750, 1050 and 1200 nm in diameters are used.

Whereas EBL method is evaluated as a more versatile and tunable method for fabrication of this structures, the procedure is a sequential process that involve a direct E-beam writing. Therefore, EBL is a more expensive and time consuming approach compared to the NSL method. On the other hand, since the template used in NSL method are fabricated by self assembly of microspheres in a monolayer structures, this method can produce much larger area of patterned surface in a remarkably shorter time. However, there are two major limitations in the NSL method in term of flexibility of the fabrication method. These limitations are in the shape of the holes and the thickness of the films. The only possible option for hole's shape in the fabricated structures using the NSL method is circular shape. The thickness of the metal film cannot exceed the height of the etched microspheres, otherwise, it would be impossible to remove the buried microspheres by chemical etching and open the holes.

In order to obtain reproducible and tunable fabrication methods, both techniques have been repeatedly tested and the fabricated structures characterized. The results and analyses of the potential defects are presented in the Chapter 3. In the following, some of the important steps for each procedure are presented that should be considered in order to improve the yield factor of the methods.

Etching of the PMGI polymer to form the nanopillars is one of the important steps

in the EBL method. The etching time is a critical parameter in this step because over etching of PMGI will result in the non-vertical hole walls. On the other hand, the liftoff of an under-etched PMGI layer will remove the structures and the whole process will fail. Therefore the exact thickness of the PMGI layers was characterized using a profilometer and the etching time was calculated precisely prior to the etching process. Another essential parameter in this method is metallization which needs to be done vertically (i.e. snow fall deposition). It turns out that the best method to do this is metallization by using an electron beam evaporation technique with a rate of 0.8 to 1 angstrom/s.

The other method that we introduced to fabricate the nanoholes array structures is based on nanosphere lithography (NSL) technique. In this method, a template of crystalline monolayer of microspheres is fabricated by self assembling microspheres on the glass substrate. Experiments showed that rendering of the glass substrate before deposition of the microspheres is a critical step. It has been shown that the best crystallization condition to maximize the area of coverage of the monolayer microspheres structure and hence the area of nanohole array is provided when the microspheres are spread on the surface while the thickness of the host solution is less than half of diameter of the microspheres. In hydrophilic surfaces, the contact angle between the glass surface and the droplet of the colloidal solution of the microspheres is reduced and the spheres could easily spread on the surface.

Since the template of the monolayer microspheres in NSL method are fabricated using a spin coating technique two essential parameters, the rotational speed and the acceleration rate of spinner, has to be adjusted. It turns out that these parameters are directly dependent on the size of microspheres. The results of the fine tuning of these parameters for spheres with three different diameters are presented in Table 3.1. The etching process of the microspheres is done using reactive ion etching technique. We found that due to the hexagonal close packed configuration of the nanospheres, the etching

process is anisotropic, the tops and the sides of the spheres did not etch with the same rate. The detail discussion about this process is presented in 3.3.1.

Following the fabrications, the devices were characterized using UV-VIS spectrometry. The sensitivity of measurements is very dependent on the area of structures. The larger the area, the easier to characterize the devices and the lower is the sensitivity of the measurements. As the total energy transmission through an array of long range ordered nanoholes increases, compared to a short range ordered nanohole array, the effect of the noise in the collector of the spectrometer is reduced, which made the far-field, non-focused and near normal UV-VIS spectrometry measurements possible.

In this work, we have also investigated the EOT phenomena theoretically. The theoretical investigation is motivated by ever increasing promising applications of this optical phenomenon. In absence of a universally accepted model for EOT, the features of the transmission spectrum with respect of the change of different structural parameters are studied using an extensive numerical calculation for electromagnetic field distributions. To be more specific, 5 sets of numerical analyses is presented in the Chapter 4, in each set, a comparative diagram is illustrated for the transmission spectra of the structures while one of the parameters including diameter of the holes , period of the arrays , thickness of the films , material of the films and the surrounding medium changes.

Among the different numerical algorithms for electromagnetic wave propagation, a time domain solver based on FDTD is used because; unlike the frequency domain algorithms the electromagnetic field distribution for the whole spectrum of the modes could be calculated in one time run of the algorithm. The optimized grid size for the circular holes is determined to be 5 nm in all three dimensions. To increase the accuracy of the numerical results, the dispersion properties of the metals is modeled according to Lorentz-Drude formulation. The good agreement between the transmission spectra from the numerical solver and the experimental measurements presented in Chapter 3 suggests

that the implemented framework could be used as a designing tool for structures that support EOT.

Moreover, the systematic analysis of the transmission spectra of the long range ordered nanohole arrays provides an opportunity to investigate the transmission process. In this study, I incorporate the effect of three major optical modes involved in the transmission process, namely, surface plasmon polariton *(SPP)*, Localized Surface Plasmon Resonance *(LSPR)* and Wood Anomalies *(WA)* and evaluate the results by the suggested model for each of these modes. The following are the highlights of the investigations when the results of the calculations compared by the predictions of the existing models for the features of the transmission spectrum:

1- Contrary to the prediction of the *SPP* model (i.e. the position of the peaks in the transmission spectrum are linearly and directly proportional to the period of the arrays), the result of numerical analysis showed otherwise. Confirmed by the numerical calculation, the shift is still monolithically related to the period of the arrays but not linearly.

2- The diffractive modes of *WA* are associated to the position of the minima in the transmission spectrum. The numerical results in a wide range of the changes of period confirm that the *WA* modes are shifting proportionally with spatial periods of structures, independent of the material of the films. These results are in agreement with the suggestion of the models for diffractive mode of *WA*.

3- The cut-off frequencies of the transmission are mostly defined by the *LSPR* at the rim of the holes rather than periodicity of the structures. The thickness analysis also showed that the increase in the thickness is decreasing the cut-off frequency.

4- The sensitivity of the long range order nanohole structure as it is shown in the

simulation results could be potentially as much as 800 nm of shift for change of 1 unit of index of refraction.

5.2 Contributions

Pursuing the objective of this thesis, several original contributions have been made by the author. Following is a list of them, all of them are already published as peer-reviewed articles except for the number 6 which is under preparation for a journal publication.

1- Long range order array of subwavelength holes on thick metallic films of noble metal have been investigated both experimentally and theoretically. The fabrication method based on nanospheres lithography is evaluated as a high throughput and cost efficient method which unlike the electron beam lithography method is a non-sequential technique.

2- Transmission spectra measurement on the long range order nanoholes arrays showed that the peak of the transmission spectrum can be observed by a far-field, non-focused and near normal UV-VIS spectrometry. As the total energy transmission through an array of long range order nanoholes is larger as compared to a short range order nanohole array, the effect of the noise in the collector of the spectrometer is drastically reduced making the above measurements possible.

3- A new method for crystallization of the microspheres known as flow control deposition method is introduced. The main advantage of this method over the existing techniques is that most of the unused colloidal solution during deposition can be saved for future depositions. Although, the technique did not lead to fabrication of a monolayer template which is used in the NSL method, the method has successfully

been applied to the deposition of composite films containing gold nanoparticle and microspheres.

4- Observation and analyses of the structural evolution of phase transition in the crystalline structure of self assembled microspheres in a single layer. In this research, the importance of the monodispersity of the colloidal solution of microspheres is demonstrated. If the size polydispersity of colloidal solution is increased the transition between FCC and HCP on a monolayer structures will be more frequent.

5- Fabrication of structures of patterned gold nanoparticle using convective vertical self assembly of gold nanoparticle and microspheres. In this technique, first a multilayer crystalline structure is fabricated by deposition of the composite solution formed by polystyrene microspheres and gold nanoparticles using convective self assembly in the vertical configuration. The final gold nanoparticles structure obtained after the removal of the polystyrene microsphers has been used as biosensors.

6- With the accurate solving of the full vectorial Maxwell's equations, we have investigated the coupling mechanisms between the surface plasmon polariton *(SPP)* and incident light in a nanohole array pierced into an optically thick metallic film. Our analyses demonstrate that the transmitted spectra through these structures are due to various contributions of the *SPP* and *LSPR* and *WA* diffractive modes. It has been discussed that the LSPR and SPP signatures could be observed in the peaks of the maxima of the spectrum whereas the minimum observed is only defined by the *WA* diffractive modes. Linearity and proportionality of the WA with the dips of the transmitted spectra is demonstrated in this work. The systematic analyses of the optical transmission spectrum indicate that the intensities and positions of the transmission peaks are very dependent on the diameter of the holes and thickness of the films. It is shown that for the structure with the same periodicity (i.e. the

center to center distance of the hole remains constant) the peaks are shifted toward the shorter wavelength as the thickness of the metallic films is increased or when the hole diameter is decreased.

5.3 Publication

- Fabrication of Ordered Films of Polystyrene Gold Composites by a New Flow-Controlled Method. Simona Badilescu, Nader Seirafianpour, Ahmad-Reza Hajiaboli, Yahia Djaoued,Mojtaba Kahrizi, P.V. Ashrit and Vo-Van Truong, Journal of Materials Science: Materials in Electronics, March 2007.

- Study of the Structural Evolution within Polystyrene and Polystyrene-Gold Composite Colloidal Crystals by AFM and SEM. Simona Badilescu, Ahmad-Reza Hajiaboli, Nader Seirafianpour, Ramin Banan Sadeghian, Mojtaba Kahrizi and Vo-Van Truong, Applied Physics Letters, 90, 023113 (2007).

- A Micro-Raman Spectroscopy Study of Colloidal Crystal Films of Polystyrene-Gold Composites. Yahia Djaoued, Simona Badilescu, Nader Seirafianpour, Ahmad-Reza Hajiaboli, Ramin Banan Sadeghian, Katherine Bradley, Ralf Brning, Mojtaba Kahrizi and Vo-Van Truong, Applied Spectroscopy (2007).

- Optical Properties of Thick Metal Nanohole Arrays Fabricated by Electron Beam - and Nanosphere Lithography. A. Hajiaboli, Bo Cui, M. Kahrizi, Vo-Van Truong, Physica Status Solidi (A) Applications and Materials, v 206, n 5, p 976-979, May 2009

- Spectral behaviour of thick metal films perforated with nanoholes. Ahmad Reza Hajiaboli, Mojtaba Kahrizi, Vo-Van Truong, in preparation (2009).

Conferences

- Biosensing Based on Surface Plasmon Resonance of Gold Nanohole and Nanoring Arrays Fabricated by a Novel Nanosphere Lithography Technique. Farah Fida, Ramin Banan-Sadeghian, Ahmad Reza Hajiaboli, Yahia Djaoued, Simona Badilescu, Subramanian Balaji, M. Kahrizi and Vo-Van Truong, International Conference on Biocomputation, Bioinformatics, and Biomedical Technologies, (2008).

- Optical Properties of Thick Metal Nanohole Arrays Fabricated by Electron Beam and nanospheres Lithography. A. Hajiaboli, Bo Cui, M. Kahrizi and Vo-Van Truong, International Conference on Optical and Optoelectronic Properties of Materials and Applications. (ICOOPMA) 2008, Edmonton.

- Fabrication of Ordered Gold nanostructures for Surface Plasmon Resonance Based Sensor Aplications. Farah Fida, Ahmad Reza Hajiaboli, R. B. Sadeghian, Y. Djaoued, S. Badilescu, S. Balaji, M. Kahrizi and Vo-Van Truong proceeding of 13th Canadian Semiconductor Technology Conference (CSTC), Montreal, August 2007. pp.89-90.

5.4 Further Directions

Results obtained and demonstrated in this thesis provide an opportunity to expand the research in several new directions. The following are two of the suggested areas:

1- Long range ordered nanoholes structures as biosensors:

It has been shown that the peak positions of transmission spectrum are sensitive to the change of index of refraction of ambient medium. This device can be used as high throughput biosensors for mimicking the bimolecular interaction.

2- Fabrication of the alternative plasmonic structures:

The monolayer templates of self assembled microspheres that are fabricated in this thesis are versatile building block used in the fabrication of diverse nanostructures such as arrays of nanorings and nanodisks. Long range order nanodisk or nanoring structures can be fabricated using the template proposed by present method.

Bibliography

[1] Bethe, H.A., *Theory of Diffraction by Small Holes.* Physical Review, 1944. 66(7-8): p. 163.

[2] Ebbesen, T.W., et al., *Extraordinary optical transmission through sub-wavelength hole arrays.* Nature, 1998. 391(6668): p. 667-9.

[3] Skinner, J.L., A.A. Talin, and D.A. Horsley, *A MEMS light modulator based on diffractive nanohole gratings.* Opt. Express, 2008. 16(6): p. 3701-3711.

[4] Sedoglavich, N., et al., *Polarisation and wavelength selective transmission through nanohole structures with multiple grating geometry.* Opt. Express, 2008. 16(8): p. 5832-5837.

[5] Luo, X. and T. Ishihara, *Subwavelength photolithography based on surface-plasmon polariton resonance.* Opt. Express, 2004. 12(14): p. 3055-3065.

[6] Luo, X. and T. Ishihara, *Sub-100-nm photolithography based on plasmon resonance.* Japanese Journal of Applied Physics, Part 1 , 2004. 43(6B): p. 4017-21.

[7] Brolo, A.G., et al. *Development of plasmonic substrates for biosensing.* 2008. USA: SPIE - The International Society for Optical Engineering.

[8] Stark, P.R.H., A.E. Halleck, and D.N. Larson, *Short order nanohole arrays in metals for highly sensitive probing of local indices of refraction as the basis for a highly multiplexed biosensor technology.* Methods, 2005. 37(1): p. 37-47.

[9] Stewart, M.E., et al., *Nanostructured plasmonic sensors.* Chemical Reviews, 2008. 108(2): p. 494-521.

[10] Rindzevicius, T., et al., *Long-range refractive index sensing using plasmonic nanostructures.* Journal of Physical Chemistry C, 2007. 111(32): p. 11806-10.

[11] Fida, F., et al. *Biosensing based on surface plasmon resonance of gold nanohole and nanoring arrays fabricated by a novel nanosphere lithography technique.* 2008. Bucharest, Romania: Inst. of Elec. and Elec. Eng. Computer Society.

[12] Otto, A., *Excitation of nonradiative surface plasma waves in silver by the method of frustrated total reflection.* Zeitschrift fr Physik A Hadrons and Nuclei, 1968. 216(4): p. 398-410.

[13] Knoll, W., *Interfaces and thin films as seen by bound electromagnetic waves.* Annual Review of Physical Chemistry, 1998. 49: p. 569-638.

[14] Herminghaus, S., et al., *Hydrogen and helium films as model systems of wetting.* Annalen der Physik, 1997. 6(6): p. 425-47.

[15] Chien, F.C. and S.J. Chen, *A sensitivity comparison of optical biosensors based on four different surface plasmon resonance modes.* Biosensors and Bioelectronics, 2004. 20(3): p. 633-642.

[16] Malmqvist, M., *Biospecific interaction analysis using biosensor technology.* Nature, 1993. 361(6408): p. 186-186.

[17] Braguglia, C.M., Biosensors: *An Outline of General Principles and Application.* Chemical and Biochemical Engineering Quarterly, 1998. 12(4): p. 183-190.

[18] Berndt, R., J.K. Gimzewski, and P. Johansson, *Inelastic tunneling excitation of tip-induced plasmon modes on noble-metal surfaces.* Physical Review Letters, 1991. 67(27): p. 3796-9.

[19] Shea, M.J. and R.N. Compton, *Surface-plasmon ejection of Ag+ ions from laser irradiation of a roughened silver surface.* Physical Review B, 1993. 47(15): p. 9967.

[20] Przybilla, F., et al., *Efficiency and finite size effects in enhanced transmission through subwavelength apertures.* Opt. Express, 2008. 16(13): p. 9571-9579.

[21] Yang, J.-C., et al., *Multiplexed plasmonic sensing based on small-dimension nanohole arrays and intensity interrogation.* Biosensors and Bioelectronics, 2009. 24(8): p. 2334-2338.

[22] Eftekhari, F., et al., *Polarization-dependent sensing of a self-assembled monolayer using biaxial nanohole arrays.* Applied Physics Letters, 2008. 92(25): p. 253103-3.

[23] Brolo, A.G., et al. *The development of surface-plasmon-based sensors using arrays of sub-wavelength holes.* 2005. Bellingham WA, WA 98227-0010, United States: International Society for Optical Engineering.

[24] Brolo, A.G., et al., *Enhanced fluorescence from arrays of nanoholes in a gold film.* Journal of the American Chemical Society, 2005. 127(42): p. 14936-14941.

[25] De Leebeeck, A., et al., *On-Chip Surface-Based Detection with Nanohole Arrays.* Analytical Chemistry, 2007. 79(11): p. 4094-4100.

[26] Henzie, J., L. Min Hyung, and T.W. Odom, *Multiscale patterning of plasmonic metamaterials.* Nature Nanotechnology, 2007. 2(9): p. 549-54.

[27] Jaksic, Z., et al. *Scanning probe-shaped nanohole arrays with extraordinary optical transmission as platform for enhanced surface plasmon-based biosensing.* 2006. Piscataway, NJ, USA: IEEE.

[28] Yang, T. and H.P. Ho, *Computational investigation of nanohole array based SPR sensing using phase shift.* Opt. Express, 2009. 17(13): p. 11205-11216.

[29] Genet, C. and T.W. Ebbesen, Light in tiny holes. Nature, 2007. 445(7123): p. 39-46.

[30] Shalaev, V.M. and S. Kawata, *Nanophotonics with surface plasmons.* 1st ed. Advances in nano-optics and nano-photonics,. 2007, Amsterdam ; Boston: Elsevier. xiv, 325 p.

[31] Wood, R.W., *On a Remarkable Case of Uneven Distribution of Light in a Diffraction Grating Spectrum.* Proceedings of the Physical Society of London, Vol. 18(1). 1902. 269-275.

[32] Pines, D., *Collective Energy Losses in Solids.* Reviews of Modern Physics, 1956. 28(3): p. 184.

[33] Fano, U., *Atomic Theory of Electromagnetic Interactions in Dense Materials.* Physical Review, 1956. 103(5): p. 1202.

[34] Ritchie, R.H., *Plasma Losses by Fast Electrons in Thin Films.* Physical Review, 1957. 106(5): p. 874.

[35] Ritchie, R.H., et al., *Surface-Plasmon Resonance Effect in Grating Diffraction.* Physical Review Letters, 1968. 21(22): p. 1530.

[36] Kreibig, U. and P. Zacharias, *Surface plasma resonances in small spherical silver and gold particles.* Zeitschrift fr Physik A Hadrons and Nuclei, 1970. 231(2): p. 128-143.

[37] Maier, S.A., P.G. Kik, and H.A. Atwater, *Optical pulse propagation in metal nanoparticle chain waveguides.* Physical Review B, 2003. 67(20): p. 205402.

[38] Takahara, J., et al., *Guiding of a one-dimensional optical beam with nanometer diameter.* Opt. Lett., 1997. 22(7): p. 475-477.

[39] Kyung-Young, J., F.L. Teixeira, and R.M. Reano, *Au/SiO_2 nanoring plasmon waveguides at optical communication band.* Journal of Lightwave Technology, 2007. 25(9): p. 2757-65.

[40] Rakic, A.D., et al., *Optical properties of metallic films for vertical-cavity optoelectronic devices.* Applied Optics, 1998. 37(22): p. 5271-83.

[41] Bora, U. and S. Yunlong, *Interference of surface waves in a metallic nanoslit.* Optics Express, 2007. 15(3): p. 1182-1190.

[42] OptiFDTD simulation tool *website address: http://www.optiwave.com/products/fdtd_overview.html* updated as 19/01/20010.

[43] Hajiaboli, Ahmad Reza, et al., *Optical properties of thick metal nanohole arrays fabricated by electron-beam and nanosphere lithography.* Physica Status Solidi (A) Applications and Materials, 2009. 206(6668): p. 976-979.

[44] de Abajo, F.J.G., *Colloquium: Light scattering by particle and hole arrays.* Reviews of Modern Physics, 2007. 79(4): p. 1267-24.

[45] Martin-Moreno, L., et al., *Theory of extraordinary optical transmission through subwavelength hole arrays.* Physical Review Letters, 2001. 86(6): p. 1114-17.

[46] Salomon, L., et al., *Near-Field Distribution of Optical Transmission of Periodic Subwavelength Holes in a Metal Film.* Physical Review Letters, 2001. 86(6): p. 1110.

[47] Ghaemi, H.F., et al., *Surface plasmons enhance optical transmission through subwavelength holes.* Physical Review B (Condensed Matter), 1998. 58(11): p. 6779-82.

[48] Hessel, A. and A.A. Oliner, *A New Theory of Wood?s Anomalies on Optical Gratings.* Appl. Opt., 1965. 4(10): p. 1275-1297.

[49] Chang, S.-H., S.K. Gray, and G.C. Schatz, *Surface plasmon generation and light transmission by isolated nanoholes and arrays of nanoholes in thin metal films.* Optics Express, 2005. 13(8): p. 3150-3165.

[50] Sarrazin, M., J.P. Vigneron, and J.M. Vigoureux, *Role of wood anomalies in optical properties of thin metallic films with a bidimensional array of subwavelength holes.* Physical Review B (Condensed Matter and Materials Physics), 2003. 67(8): p. 85415-1.

[51] Lezec, H. and T. Thio, *Diffracted evanescent wave model for enhanced and suppressed optical transmission through subwavelength hole arrays.* Opt. Express, 2004. 12(16): p. 3629-3651.

[52] Sarrazin, M. and J.-P. Vigneron, *Optical properties of tungsten thin films perforated with a bidimensional array of subwavelength holes.* Physical Review E, 2003. 68(1): p. 016603.

[53] Ulrich, R., *Far-infrared properties of metallic mesh and its complementary structure.* Infrared Physics, 1967. 7(1): p. 37-55.

[54] Chen, Chao-Chun, *Diffraction of electromagnetic waves by a conducting screen perforated periodically with circular holes.* IEEE Transactions on Microwave Theory and Techniques, 1971. MTT-19(5): p. 475-81.

[55] Gordon, R., *Bethe's aperture theory for arrays.* Physical Review A (Atomic, Molecular, and Optical Physics), 2007. 76(5): p. 053806-5.

[56] Chen, D.Z.A., et al., *Extraordinary optical transmission through subwavelength holes in a polaritonic silicon dioxide film.* Applied Physics Letters, 2007. 90(18): p. 181921-1.

[57] Genet, C., M.P. *van Exter, and J.P. Woerdman, Fano-type interpretation of red shifts and red tails in hole array transmission spectra.* Optics Communications, 2003. 225(4-6): p. 331-336.

[58] Pacifici, D., et al., *Universal optical transmission features in periodic and quasiperiodic hole arrays.* Optics Express, 2008. 16(12): p. 9222-9238.

[59] Fan Z., et al., *Critical process of extraordinary optical transmission through periodic subwavelength hole array: hole-assisted evanescent-field coupling.* Optics Communications, 2008. 281(21): p. 5467-71.

[60] Popov, E., et al., *Theory of light transmission through subwavelength periodic hole arrays.* Physical Review B, 2000. 62(23): p. 16100.

[61] Gao H. , J. Henzie, and T.W. Odom, *Direct evidence for surface plasmon-mediated enhanced light transmission through metallic nanohole arrays.* Nano Letters, 2006. 6(9): p. 2104-8.

[62] Degiron, A. and T.W. Ebbesen, *The role of localized surface plasmon modes in the enhanced transmission of periodic subwavelength apertures.* Journal of Optics A: Pure and Applied Optics, 2005. 7(2): p. S90-S96.

[63] Koerkamp, K.J.K., et al., *Strong Influence of Hole Shape on Extraordinary Transmission through Periodic Arrays of Subwavelength Holes.* Physical Review Letters, 2004. 92(18): p. 183901.

[64] van der Molen, K.L., et al., *Role of shape and localized resonances in extraordinary transmission through periodic arrays of subwavelength holes: experiment and theory.* Physical Review B (Condensed Matter and Materials Physics), 2005. 72(4): p. 45421-1.

[65] Li, T., et al., *Manipulating optical rotation in extraordinary transmission by hybrid plasmonic excitations.* Applied Physics Letters, 2008. 93(2): p. 021110.

[66] Van der Molen, K.L., et al., *Influence of hole size on the extraordinary transmission through subwavelength hole arrays.* Applied Physics Letters, 2004. 85(19): p. 4316-4318.

[67] Gordon, R., et al., *Strong Polarization in the Optical Transmission through Elliptical Nanohole Arrays.* Physical Review Letters, 2004. 92(3): p. 37401-1.

[68] Mei, S., et al., *The influence of hole shape on enhancing transmission through subwavelength hole arrays.* Chinese Physics, 2006. 15(7): p. 1591-1594.

[69] Kim, J.H. and P.J. Moyer, *Transmission characteristics of metallic equilateral triangular nanohole arrays.* Applied Physics Letters, 2006. 89(12): p. 121106-3.

[70] Fida, F., et al., *Fabrication of Ordered Gold Nanostructures for Surface Plasmon Resonance-Based Sensor Applications.* Proceeding of 13th Canadian Semiconductor Technology Conference (CSTC), Montreal, August 2007. pp.89-90.

[71] Lee, F.Y., et al., *Fabrication of gold nano-particle arrays using two-dimensional templates from holographic lithography.* Current Applied Physics, 2009. 9(4): p. 820-825.

[72] Wu, W., et al., *Large areas of periodic nanoholes perforated in multistacked films produced by lift-off.* Journal of Vacuum Science and Technology B: Microelectronics and Nanometer Structures, 2008. 26(5): p. 1745-1747.

[73] ZEP-520 *High Resolution Positive Electron Beam Resist.* Technical report 2001.

[74] Alexandre, M., D. Alain, and L.F. Thomas, *Localized surface plasmons on a torus in the nonretarded approximation.* Physical Review B (Condensed Matter and Materials Physics), 2005. 72(15): p. 155426.

[75] Cui, B. and T. Veres, *Fabrication of metal nanoring array by nanoimprint lithography (NIL) and reactive ion etching.* Microelectronic Engineering, 2007. 84(5-8): p. 1544-1547.

[76] Kim, S., et al., *Patterned arrays of au rings for localized surface plasmon resonance.* Langmuir, 2006. 22(17): p. 7109-7112.

[77] Zhou, X., et al., *Fabrication of gold nanocrescents by angle deposition with nanosphere lithography for localized surface plasmon resonance applications.* Journal of Nanoscience and Nanotechnology, 2008. 8(7): p. 3369-3378.

[78] Gordon, R., et al. *Comparing the transmission through ellipse and double-hole nanophotonic arrays in gold films.* 2004. New York, NY 10016-5997, United States: Institute of Electrical and Electronics Engineers Inc.

[79] Zheng, Y.B., et al., *Fabrication of large area ordered metal nanoring arrays for nanoscale optical sensors.* Journal of Non-Crystalline Solids, 2006. 352(23-25): p. 2532-2535.

[80] Zhang, J., et al., *Nearly Monodisperse Cu2O and CuO Nanospheres: Preparation and Applications for Sensitive Gas Sensors.* Chemistry of Materials, 2006. 18(4): p. 867-871.

[81] Wang, Y., et al., *Spherical antireflection coatings by large-area convective assembly of monolayer silica microspheres.* Solar Energy Materials and Solar Cells, 2009. 93(1): p. 85-91.

[82] Sun, Z. and B. Yang, *Fabricating colloidal crystals and construction of ordered nanostructures.* Nanoscale Research Letters, 2006. 1(1): p. 46-56.

[83] Badilescu, S., et al., *Study of the structural evolution within polystyrene and polystyrene-gold composite colloidal crystals by atomic force microscopy and scanning electron microscopy.* Applied Physics Letters, 2007. 90(2): p. 023113-3.

[84] Barnes, W.L., et al., *Surface plasmon polaritons and their role in the enhanced transmission of light through periodic arrays of subwavelength holes in a metal film.* Physical Review Letters, 2004. 92(10): p. 107401-1.

[85] Martn-Moreno, L., et al., *Theory of Extraordinary Optical Transmission through Subwavelength Hole Arrays.* Physical Review Letters, 2001. 86(6): p. 1114.

[86] Krishnan, A., et al., *Evanescently coupled resonance in surface plasmon enhanced transmission.* Optics Communications, 2001. 200(1-6): p. 1-7.

[87] Vigoureux, J.M., *Analysis of the Ebbesen experiment in the light of evanescent short range diffraction.* Optics Communications, 2001. 198(4-6): p. 257-263.

[88] Treacy, M.M.J., *Dynamical diffraction explanation of the anomalous transmission of light through metallic gratings.* Physical Review B, 2002. 66(19): p. 195105.

[89] Gordon, R., L.K.S. Kumar, and A.G. Brolo, *Resonant light transmission through a nanohole in a metal film. IEEE Transactions on Nanotechnology,* 2006. 5(3): p. 291-4.

[90] Wu, B. and Q. Wang. *Discussion of the mechanism of extraordinary optical transmission in metallic gratings.* 2006. Hangzhou, China: Institute of Electrical and Electronics Engineers Computer Society, Piscataway, NJ 08855-1331, United States.

[91] Ma, J., et al., *Study of the surface plasma transmission properties of a Fabry-Perot resonator by numerical simulation.* Journal of Optics A: Pure and Applied Optics, 2008. 10(3): p. 035002.

[92] Lesuffleur, A., et al., *Periodic nanohole arrays with shape-enhanced plasmon resonance as real-time biosensors. Applied Physics Letters,* 2007. 90(24): p. 243110-1.

[93] Genet, C., M.P. van Exter, and J.P. Woerdman, *Fano-type interpretation of red shifts and red tails in hole array transmission spectra.* Optics Communications, 2003. 225(4-6): p. 331-6.

[94] Jia, W. and Xiaohan Liu , *Origin of superenhanced light transmission through two-dimensional subwavelength rectangular hole arrays.* European Physical Journal B, 2005. 46(3): p. 343-7.

[95] Jia, W. and Xiaohan Liu, *Mechanism of the superenhanced light transmission through 2D subwavelength coaxial hole arrays.* Physics Letters A, 2005. 344(6): p. 451-6.

[96] Qiang, R., et al., *Modelling of infrared bandpass filters using three-dimensional FDTD method.* Electronics Letters, 2005. 41(16): p. 914-15.

[97] Johnson, P.B. and R.W. Christy, *Optical Constants of the Noble Metals.* Physical Review B, 1972. 6(12): p. 4370.

[98] Kanso, M., S. Cuenot and G. Louarn, *Sensitivity of Optical Fiber Sensor Based on Surface Plasmon Resonance: Modeling and Experiments.* Plasmonics, 2008. 3: p. 49-57.